^{18}F-FDOPA Positron Emission Tomography and Diffusion Tensor Imaging for Radiation Therapy of High-Grade Gliomas with Dose Painting

by

Robert Kosztyla

B.Sc., The University of Waterloo, 2007
B.Ed., Queen's University, 2007
M.Sc., The University of British Columbia, 2009

A THESIS SUBMITTED IN PARTIAL FULFILLMENT OF
THE REQUIREMENTS FOR THE DEGREE OF

DOCTOR OF PHILOSOPHY

in

The Faculty of Graduate and Postdoctoral Studies

(Physics)

THE UNIVERSITY OF BRITISH COLUMBIA

(Vancouver)

March 2014

Abstract

In the radiation therapy of high-grade gliomas, T1-weighted magnetic resonance imaging (MRI) with contrast enhancement does not accurately represent the extent of the tumour. Functional imaging techniques, such as positron emission tomography (PET) and diffusion tensor imaging (DTI), can potentially be used to improve tumour localization and for biologically-based treatment planning. This project investigated tumour localization using 3,4-dihydroxy-6-[^{18}F]fluoro-L-phenylalanine (^{18}F-FDOPA) PET and interhemispheric difference images obtained from DTI, and determined whether radiation therapy of high-grade gliomas using dose painting was feasible with volumetric modulated arc therapy (VMAT). First, radiation therapy target volumes obtained from five observers using ^{18}F-FDOPA PET and MRI were compared with the location of recurrences following radiotherapy. It was demonstrated with simultaneous truth and performance level estimation that high-grade glioma radiation therapy target volumes obtained with PET had similar interobserver agreement to MRI-based volumes. Although PET target volumes were significantly larger than volumes obtained using MRI, treatment planning using the PET-based volumes may not have yielded better treatment outcomes since all but one central recurrence extended beyond the PET abnormality. The second study characterized the distribution of fractional anisotropy (FA) and mean diffusivity (MD) values obtained from DTI, as well as FA and MD interhemispheric differences. It was

demonstrated that FA, MD, and interhemispheric differences approached those of contralateral normal brain as the distance from the tumour increased, consistent with the expectation of a gradual and decreasing presence of tumour cells. Lastly, a treatment planning study compared VMAT for high-grade gliomas obtained from dose painting using ^{18}F-FDOPA PET images. Dose constraints for each contour were specified by a radiobiological model. VMAT planning using dose painting for high-grade gliomas was achieved using biologically-guided thresholds of ^{18}F-FDOPA uptake with no significant change in the dose delivered to critical structures.

Preface

A version of Chapter 2 has been published (Kosztyla R, Chan EK, Hsu F, Wilson D, Ma R, Cheung A, Zhang S, Moiseenko V, Benard F, Nichol A. High-grade glioma radiation therapy target volumes and patterns of failure obtained from magnetic resonance imaging and ^{18}F-FDOPA positron emission tomography delineations from multiple observers. Int J Radiat Oncol Biol Phys. 2013;87(5): 1100–6. doi:10.1016/j.ijrobp.2013.09.008.). The principal investigator for this study was A. Nichol. Radiation therapy target volumes were outlined by F. Hsu, D. Wilson, R. Ma, A. Cheung, and A. Nichol. Image fusion in treatment planning software was done by S. Zhang. Recurrence image sets were identified by E. K. Chan. I conducted all data analysis, including analysis with simultaneous truth and performance level estimation, and wrote the manuscript. All authors assisted in editing the manuscript.

A version of Chapter 3 has been submitted for publication (Kosztyla R, Reinsberg SA, Moiseenko V, Toyota B, Nichol A. Interhemispheric difference images from postoperative diffusion tensor imaging of gliomas.) The diffusion tensor fitting method was selected by S. Reinsberg and myself. I devised the method of obtaining interhemispheric difference images from DTI parameters and completed all image registration, diffusion tensor fitting, image analysis, and statistical interpretation. Clinical guidance was provided by A. Nichol.

In Chapter 4, the treatment planning technique for dose painting was devised by myself, V. Moiseenko, and S. Reinsberg, with clinical guidance from A. Nichol. S. Zhang imported images into treatment planning software. Volumes of interest for dose escalation were identified by A. Nichol. I completed fusion of treatment planning CT and PET/CT images, obtained contours from PET images for dose escalation, and completed all treatment planning and data analysis.

The work reported in this thesis was completed with approval from the University of British Columbia BC Cancer Agency research ethics board, certificate numbers H08-02314 for the work in Chapter 2 and H10-02888 for the work in Chapters 3 and 4.

Table of Contents

List of Tables

List of Figures

List of Abbreviations

^{11}C-MET	^{11}C-methionine
^{18}F-FDOPA	3,4-dihydroxy-6-[^{18}F]fluoro-L-phenylalanine
^{18}F-FDG	^{18}F-fluorodeoxyglucose
^{18}F-FET	^{18}F-fluoroethyltyrosine
3D-CRT	three-dimensional conformal radiation therapy
ADC	apparent diffusion coefficient
BED	biologically equivalent dose
BTV	biological target volume
CI	conformity index
CSF	cerebrospinal spinal fluid
CT	computed tomography
CTV	clinical target volume
DTI	diffusion tensor imaging
DVH	dose volume histogram
EUD	equivalent uniform dose
FA	fractional anisotropy
FLAIR	fluid attenuated inversion recovery
FSL	Oxford Centre for Functional MRI of the Brain Software Library
GTV	gross tumour volume

Gy	gray
HI	homogeneity index
HU	Hounsfield unit
ICRU	International Commission on Radiation Units and Measurements
IMRT	intensity modulated radiation therapy
L-DOPA	3,4-dihydroxy-L-phenylalanine
linac	linear accelerator
MD	mean diffusivity
MLC	multileaf collimator
MNI	Montreal Neurological Institute
MRI	magnetic resonance imaging
MRSI	magnetic resonance spectroscopic imaging
MU	monitor unit
MV	megavoltage
NTCP	normal tissue complication probability
NTD	normalized total dose
OAR	organ at risk
PET	positron emission tomography
PRV	planning organ at risk volume
PTV	planning target volume
RF	radiofrequency
ROI	region of interest
RTOG	Radiation Therapy Oncology Group
SF	surviving fraction
SPECT	single photon emission computed tomography

STAPLE	simultaneous truth and performance level estimation
SUV	standardized uptake value
TCP	tumour control probability
TE	echo time
TI	inversion time
TR	repetition time
TSE	turbo spin echo
VMAT	volumetric modulated arc therapy
WHO	World Health Organization

Acknowledgements

First of all, I would like to thank my research supervisor Dr. Vitali Moiseenko (University of California, San Diego) and my academic supervisor Dr. Stefan Reinsberg (University of British Columbia) for their support and assistance as I have completed my studies and research. I would also like to thank Dr. Alan Nichol at the British Columbia Cancer Agency for his helpfulness and clinical insights. I also am grateful for the guidance and advice of my other supervisory committee members, Drs. Anna Celler and Alex Mackay at the University of British Columbia.

I would also like to extend my appreciation to other members of the research team for these projects: Drs. Fred Hsu, Don Wilson, Roy Ma, Arthur Cheung, Michael McKenzie, Susan Zhang, and Francois Benard at the British Columbia Cancer Agency, Drs. Brian Toyota and Talia Vertinsky at Vancouver General Hospital, and Dr. Elisa Chan at Saint John Regional Hospital. I gratefully acknowledge that this research has been completed with generous funding from the Natural Sciences and Engineering Research Council of Canada Alexander Graham Bell Canada Graduate Scholarship and the University of British Columbia Four Year Doctoral Fellowship. The work described in Chapter 2 was also supported by the Hershey and Yvette Porte Neuro-Oncology Endowment Fund of the BC Cancer Foundation. The work described in Chapters 3 and 4 was also

supported by the Brain Tumour Foundation of Canada and the Hershey and Yvette Porte Neuro-Oncology Endowment Fund

I would like to express my thanks to my parents, sister, and my entire extended family for their continued support of my education and research. It is greatly appreciated.

Chapter 1

Introduction

1.1 High-Grade Gliomas

Gliomas are cancers that arise from neuroglia. These cells, such as astrocytes, oligodendroglia, microglia, and ependymal cells, provide support and protection in the central nervous system (1). Astrocytes form a supporting network in the brain and spinal cord, attach neurons to blood vessels, and help regulate nutrients and ions that are needed by nerve cells. Oligodendroglia support the semirigid tissue rows between neurons in the central nervous system and produce the fatty myelin sheath of neurons. Microglia are small cells that protect the central nervous system by engulfing and destroying cellular debris and microbes, such as bacteria. Ependymal cells line the cavities of the brain and spinal cord, produce cerebrospinal spinal fluid (CSF), and with cilia move the fluid throughout the central nervous system.

Gliomas account for 28% of all primary brain and central nervous system tumours and 80% of malignant tumours (2). High-grade gliomas are those classified as either World Health Organization (WHO) grade III (e.g., anaplastic astrocytoma and oligodendroglioma) or grade IV tumours (e.g., glioblastoma) (3, 4). Despite recent technological advances, the prognosis for patients diagnosed with high-grade glioma is poor (4–7). From 1995–2010, the two-year relative survival rate for patients with anaplastic astrocytomas, anaplastic oligo-

Table 1.1. One-year, two-year, five-year, and ten-year relative survival rates for selected high-grade glioma histologies in the United States, from 1995–2010. Data from ref. 2.

Histology	Grade	Relative Survival (%)			
		1-year	2-year	5-year	10-year
Anaplastic astrocytoma	III	60.1	42.1	26.5	18.1
Anaplastic oligodendroglioma	III	80.6	67.7	50.7	37.3
Glioblastoma	IV	35.0	13.7	4.7	2.4

dendroglioma, and glioblastoma in the United States were 42.1%, 67.7%, and 13.7% (Table 1.1) (2).

The first treatment for high-grade gliomas is surgery—to make a pathological diagnosis and remove as much of the tumour as is deemed feasible and safe—followed by radiation therapy to the residual tumour (8, 9). The addition of concomitant chemotherapy to radiation therapy improves patient survival (10). Imaging plays an important role in the planning of radiation therapy. The radiation target volume is identified using postoperative computed tomography (CT) and magnetic resonance imaging (MRI) (11).

1.2 External Beam Radiation Therapy

1.2.1 Introduction

In the radiation therapy of cancer, the goal is to eradicate tumour cells using ionizing radiation while minimizing the radiation dose delivered to surrounding normal tissue. At the British Columbia Cancer Agency, radiation therapy of high-grade gliomas is delivered by external beam radiation therapy, a technique where a target in a patient is irradiated using a radiation beam located outside of the patient (12). Today, these beams are most commonly megavoltage (MV) x-ray photons or electrons from a medical linear accelerator (linac), although

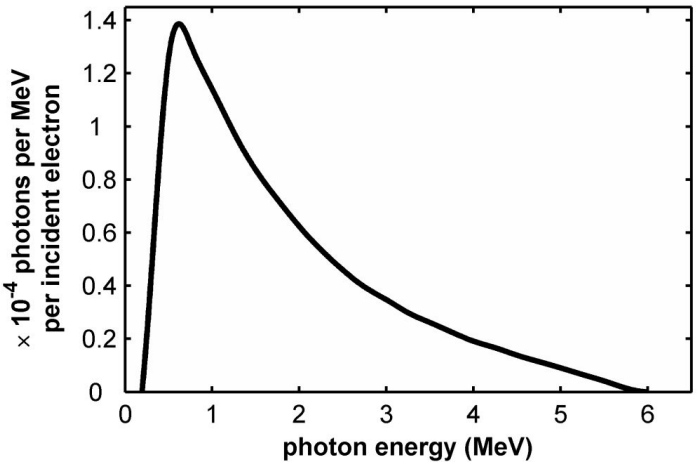

Figure 1.1. The bremsstrahlung spectrum obtained from Monte Carlo simulation of a Varian 6 MV linear accelerator. Data from ref. 14.

gammas rays from teletherapy units (e.g., using the isotope cobalt-60), protons, neutrons, and heavy ions are also used (13).

1.2.2 X-ray Production and Photon Interactions with Matter

X-ray photons are obtained from bremsstrahlung, or breaking radiation, produced by the deceleration of a high-energy charged particle near the Coulomb field of the nucleus of a target atom with large atomic number (e.g., tungsten). The intensity I of bremsstrahlung resulting from a charged particle of mass m and charge ze incident on a target nuclei with charge Ze is proportional to

$$I \propto \frac{Z^2 z^4 e^6}{m^2}. \tag{1.1}$$

An example of the bremsstrahlung spectrum obtained from a linac is shown in Figure 1.1.

As photons travel through a medium, they are exponentially attenuated:

$$I = I_0 e^{-\mu x}, \tag{1.2}$$

where μ is the linear attenuation coefficient. The attenuation of photons in matter is caused by five interactions: Rayleigh (coherent) scattering, photoelectric absorption, Compton scattering, pair production, and photonuclear interactions. In Rayleigh scattering (Figure 1.2(a)), the photon is scattered by an atom such that the photon is redirected with its energy unchanged. Ionization does not occur and no energy is transferred from the photon to the medium.

In photoelectric absorption (Figure 1.2(b)), the photon is absorbed by a bound (e.g., K-shell) electron, which is subsequently ejected from an atom. The energy of the ejected electron E is

$$E = h\nu - E_b \tag{1.3}$$

where $h\nu$ is the energy of photon and E_b is the binding energy of electron. The atom returns to the ground state by a cascade of electron transitions, resulting in the production of characteristic x-rays and Auger electrons.

In Compton scattering (Figure 1.2(c)), the photon is scattered by an outer-shell or free electron—the binding energy of electron is much less than the energy of the photon. By applying the laws of conservation of energy and momentum, the energy $h\nu'$ of the scattered photon is:

$$h\nu' = h\nu \frac{1}{1 + \alpha(1 - \cos\phi)}, \tag{1.4}$$

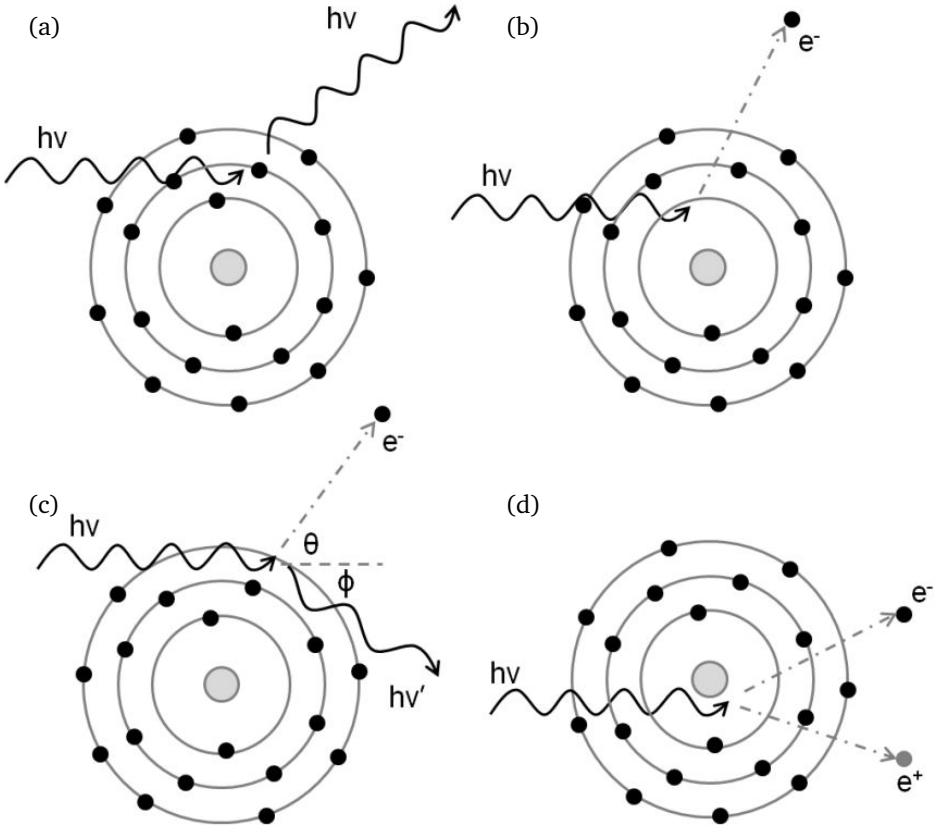

Figure 1.2. Schematic diagrams of (a) Raleigh scattering, (b) photoelectric absorption, (c) Compton scattering, and (d) pair production.

the energy E of the ejected electron is:

$$E = h\nu - h\nu' = h\nu \frac{\alpha(1-\cos\phi)}{1+\alpha(1-\cos\phi)}, \tag{1.5}$$

and the scattering angle θ of the electron is:

$$\cos\theta = (1+\alpha)\tan\frac{\phi}{2}. \tag{1.6}$$

$h\nu$ is the incident photon energy, ϕ is the scattering angle of the photon, $\alpha = h\nu/m_0c^2$, and $m_0c^2 = 0.511$ MeV is the rest energy of an electron.

The pair production of an electron and positron results from the absorption of photon near the Coulomb field of a nucleus (Figure 1.2(d)). It requires a minimum photon energy of $2m_0c^2 = 1.022$ MeV. For photon energies greater than $4m_0c^2 = 2.044$ MeV, pair production can occur in the Coulomb field of an electron. This is referred to as triplet production since the resulting energy is shared between three particles: the original electron and the electron-positron pair. In addition, the photonuclear interaction of a high-energy photon with the nucleus of an atom can lead to a nuclear reaction and the emission of a nucleon, such as a proton or neutron (15).

The quantity μ/ρ is known as the mass attenuation coefficient, where ρ is the density of the medium the photon is traveling through. The total mass attenuation coefficient μ/ρ is the sum of the mass attenuation coefficients from each photon interaction. Neglecting photonuclear interactions:

$$\frac{\mu}{\rho} = \frac{\sigma_{\text{coh}}}{\rho} + \frac{\tau}{\rho} + \frac{\sigma}{\rho} + \frac{\kappa}{\rho}, \tag{1.7}$$

where σ_{coh}/ρ, τ/ρ, σ/ρ, and κ/ρ are the mass attenuation coefficients for Raleigh scattering, the photoelectric effect, Compton (incoherent) scattering, and pair (and triplet) production, respectively. The mass attenuation coefficients for carbon and lead are shown in Figure 1.3.

1.2.3 Electron Interactions with Matter

Electrons that are set into motion by photons are scattered by the Coulomb electric force fields of atoms. These interactions can be characterized in terms of the relative size of the classical impact parameter b versus the classical atomic ra-

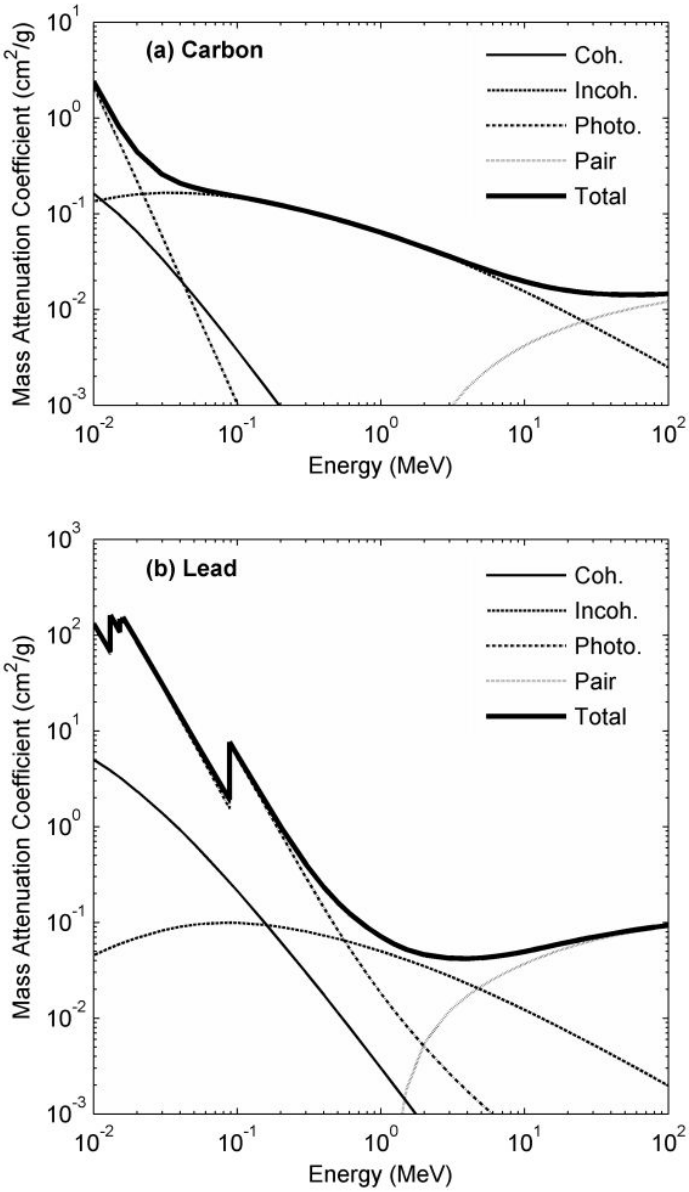

Figure 1.3. The mass attenuation coefficients for Raleigh (coh.) scattering, photoelectric absorption, Compton (incoh.) scattering, and pair production for (a) carbon and (b) lead. Data from ref. 16.

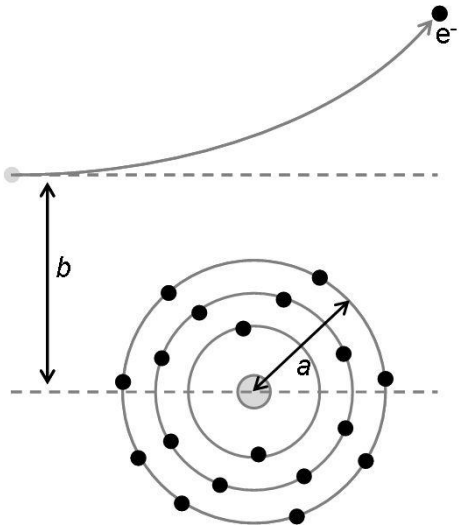

Figure 1.4. A schematic diagram of the scattering of an electron by an atom, where a is the classical atomic radius and b is the classical impact parameter.

dius a for electron collisions with atoms (Figure 1.4). Soft collisions ($b \gg a$) occur when the electron is a considerable distance from the atom and its Coulomb field interacts with the atom as a whole, causing an excitation or ionization. The energy transferred is on the order of a few eV. They are the most probable interaction and account for roughly half the energy transferred to the medium. Hard (or knock-on) collisions ($b \sim a$) occur when the electron interacts with a single atomic electron. These interactions are responsible for delta-ray production. These interactions are less probable, but account for approximately half of the energy transferred to the medium due to the larger energy transferred (a few keV to MeV) per interaction. Soft and hard collisions are inelastic as energy is transferred to the absorbing medium. If the Coulomb interaction takes place within the nucleus ($b \ll a$), the electron can be scattered elastically or an inelastic radiative interaction occurs that deflects the electron and results in the production of bremsstrahlung.

Inelastic energy losses of an electron moving through a medium of density ρ are described by the total mass-energy stopping power S/ρ:

$$\frac{S}{\rho} = \frac{1}{\rho}\frac{dE}{dx}, \tag{1.8}$$

where dE is the kinetic energy lost per unit path length dx (17). S/ρ consists of two components, the collisional stopping power S_{col}/ρ and the radiative stopping power S_{rad}/ρ:

$$\frac{S}{\rho} = \frac{S_{\text{col}}}{\rho} + \frac{S_{\text{rad}}}{\rho}. \tag{1.9}$$

The collisional stopping power characterizes the kinetic energy lost by soft and hard (knock-on) collisions. The total collision stopping power S_{col}/ρ for electrons is given by:

$$\begin{aligned}\frac{S_{\text{col}}}{\rho} = 2\pi r_0^2 N_{\text{e}} \frac{\mu_0}{\beta^2}\Bigg[\ln\frac{E^2(E+2\mu_0)}{2\mu_0 I^2} + \frac{E^2/8 - (2E+\mu_0)\mu_0 \ln 2}{(E+\mu_0)^2} \\ + 1 - \beta^2 - \delta - \frac{2C}{Z}\Bigg],\end{aligned} \tag{1.10}$$

where E is the energy of the electron, r_0 is the classic electron radius, N_{e} the electron density of the material, I is the average ionization energy, $\mu_0 = m_0 c^2$ is the rest energy of the electron, $\beta = v/c$ is the ratio of the electron's speed v to the speed of light in a vacuum c, δ is a density correction, and C/Z is a shell correction (17, 18).

The radiative stopping power characterizes bremsstrahlung production resulting from electron-nucleus interactions, and can be calculated by:

$$\frac{S_{\text{rad}}}{\rho} = 4r_0^2 \frac{N_{\text{e}} Z E}{137}\left[\ln\frac{2(E+\mu_0)}{\mu_0} - \frac{1}{3}\right]. \tag{1.11}$$

1.2.4 Absorbed Dose

Photons do not directly transfer energy to a medium. The electrons that are set in motion by interactions of photons in matter transfer energy to a medium through inelastic collisions. The kinetic energy transferred to the medium, or kerma K, is defined as:

$$K = \frac{dE_{\text{tr}}}{dm}, \tag{1.12}$$

where dE_{tr} is the net energy transferred to charged particles per unit mass dm. The kerma can be divided into two components: the collisional kerma K_{col}, which is the net energy transferred leading to the production of electrons that dissipate their energy as ionizations near the electron tracks in the medium, and the radiative kerma K_{rad}, which is the net energy transferred that leads to the production of bremsstrahlung x-rays.

The energy absorbed in the medium per unit mass is quantified by the absorbed dose D, which is defined by the International Commission on Radiation Units and Measurements (ICRU) as

$$D = \frac{d\bar{\epsilon}}{dm}, \tag{1.13}$$

where $d\bar{\epsilon}$ is the mean energy imparted by ionizing particles per unit mass dm (19). The unit for absorbed dose is the gray (Gy), defined as 1 Gy = 1 J/kg.

1.2.5 Linear Accelerators

A typical clinical linac (Figure 1.5) provides two photon beams (e.g., 6 MV and 18 MV) and several monoenergetic electron beams (e.g., 6, 9, 10, 12, 16, and 22 MeV) (13). A 6-MV photon beam will consist of a bremsstrahlung x-ray photon energy spectrum with a maximum photon energy of 6 MeV (Figure 1.1).

Figure 1.5. A linear accelerator with the electronic portal imaging device and kilovoltage cone-beam computed tomography system shown in their extended positions.

The average photon energy is approximately one third of the maximum photon energy (15).

The modern linac consists of a gantry, gantry stand, modulator cabinet, treatment couch, and control console. A schematic diagram of a linac is shown in Figure 1.6. The control console communicates with the modulator cabinet, stand, gantry, and treatment couch. High voltage pulses from the modulator are fed to a radiofrequency (RF) power generation system: a klystron (a microwave amplifier) or magnetron (a source of high power microwaves). The modulator cabinet triggers the electron gun to fire when the microwaves enter the accelerating structure. The accelerating structure is either a traveling wave or standing wave linear accelerator (13). Electrons fired by the electron gun enter the accelerating waveguide, in which a high vacuum is maintained. Cavities in the accelerating structure produce an electric field pattern that accelerates the electrons (13).

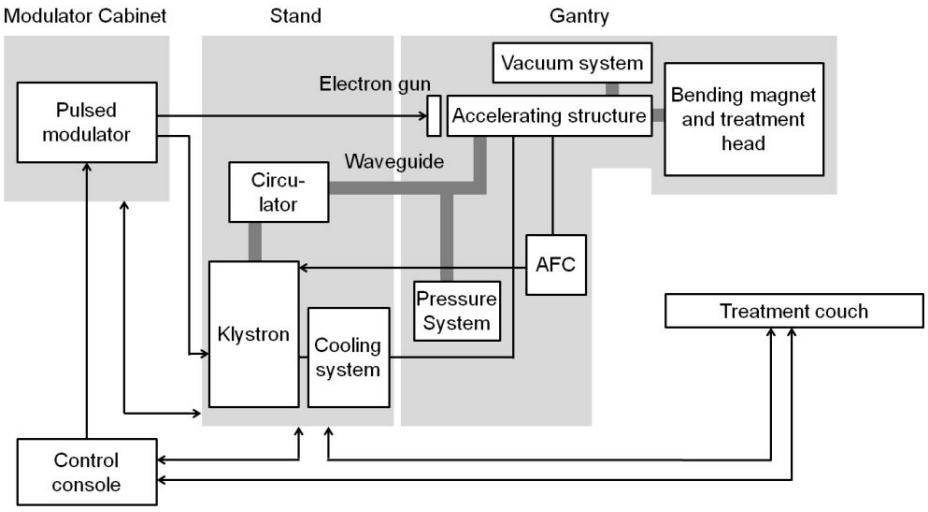

Figure 1.6. A schematic diagram of a linear accelerator. Abbreviation: AFC = automatic frequency controller.

High-energy electrons emerge from the accelerating structure in the form of a pencil beam. This electron beam is then transported to the treatment head of the linac in a straight-through design for low-energy machines (up to 6 MV) using a traveling wave linear accelerator, or via a bending magnet for higher-energy machines, which deflects the beam through 90° or 270° before it enters the treatment head (15).

In the treatment head (Figure 1.7), the electron beam enters a primary collimator which has a retractable x-ray target at its centre. Bremsstrahlung x-rays are produced when electrons hit the target. A flattening filter is inserted in the beam to produce a beam with a uniform-intensity field. When a linac is used to produce electron beams, the target and flattening field are removed from the beam line and an electron scattering foil is used to spread out the electron pencil beam and produce a beam with a uniform intensity across the field (Figure 1.8). The beam passes through a dose-monitoring system, which consists of

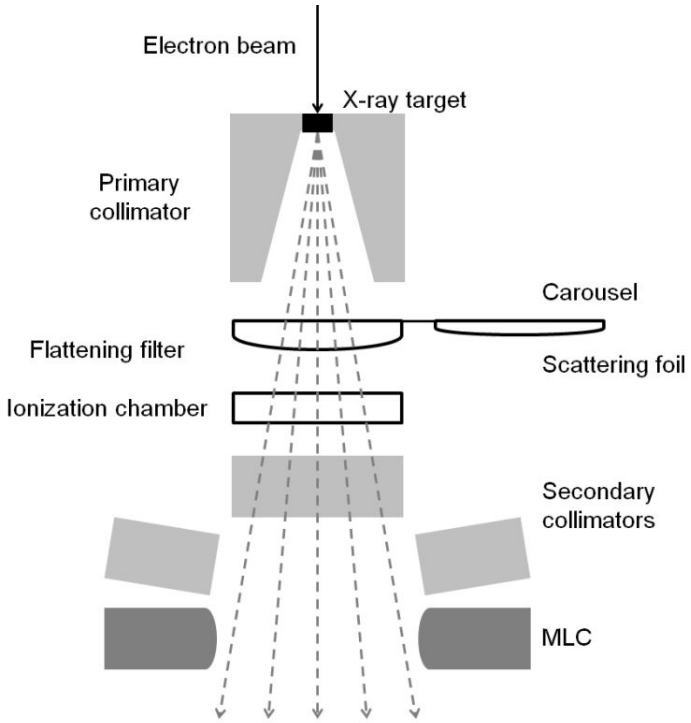

Figure 1.7. A schematic diagram of the treatment head of a linear accelerator when used to generate photon beams. Abbreviation: MLC = multileaf collimator. Adapted from ref. 15.

dual transmission ionization chambers. The ionization chambers monitor dose rate, integrated dose, and field symmetry (15). The beam then passes through a secondary collimator. Newer machines also include a multileaf collimator (MLC) (Figure 1.9) that consists of motorized leaves that provide customized field shaping. The photon or electron beam then exits the machine. A slot on the linac treatment head allows physical wedges, blocks, or compensators that modify the beam, or electron collimation systems (i.e., electron applicators) to be attached to the machine.

Modern linacs are constructed so that the gantry rotates about a horizontal axis, and the secondary collimator and treatment couch rotate about a vertical

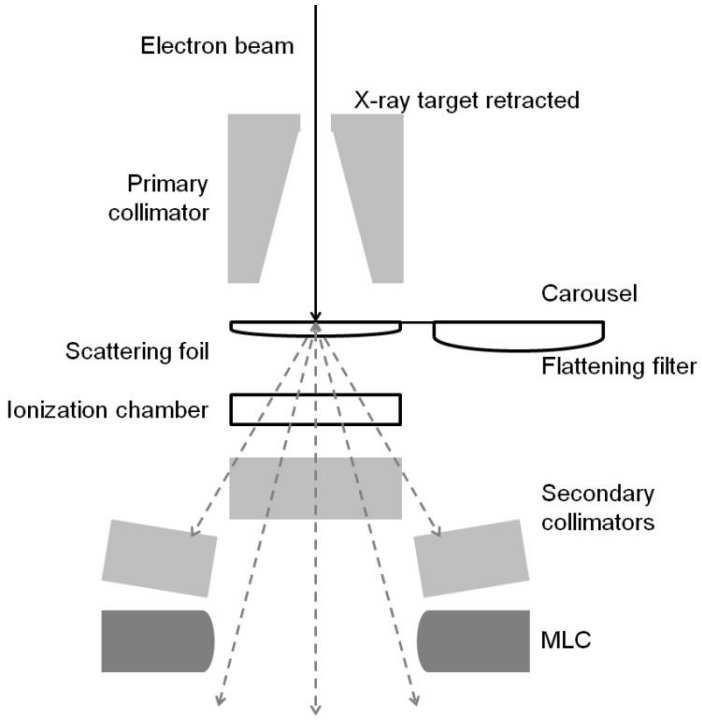

Figure 1.8. A schematic diagram of the treatment head of a linear accelerator when used to generate electron beams. Abbreviation: MLC = multileaf collimator. Adapted from ref. 15.

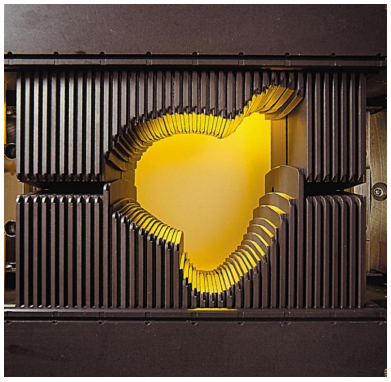

Figure 1.9. A Varian 120-leaf multileaf collimator. Image courtesy of Varian Medical Systems, Inc. All rights reserved.

axis. The point of intersection of the rotation axes of the gantry and collimator is called the isocentre (15). The isocentre is typically located 100 cm from the radiation source (i.e., x-ray target). Patients are initially setup for treatment using a laser marking system which intersects at the isocentre. Patient position can then verified using electronic portal imagers and kilovoltage cone-beam CT (shown in Figure 1.5).

Monitor units (MUs) are the measure of the machine output of a linac that is obtained from the dose-monitoring system. The dose output of a linac is usually calibrated for 1 MU to be equivalent to a dose 1 cGy under standard conditions; for example, 10×10 cm^2 field size at a reference depth in water (or water-equivalent phantom), with the reference point at the isocentre (source-axis-distance set-up).

1.3 Imaging for Radiation Therapy Planning

1.3.1 Computed Tomography

CT imaging plays an important role in radiation therapy planning. It allows for the localization of internal structures, provides information on the location and size of target volumes and critical organs, as well as quantitative information of inhomogeneities within the body. The basic principle of CT is that a narrow fan beam of x-rays scans across the patient to obtain x-ray projection images which are then reconstructed into a three dimensional volume.

Image reconstruction algorithms generate images with CT numbers, which are related to linear attenuation coefficients by the equation:

$$\text{CT number} = \frac{\mu - \mu_{\text{water}}}{\mu_{\text{water}}} \times 1000 \text{ HU}. \tag{1.14}$$

The unit used for CT numbers is the Hounsfield unit (HU). A change in CT number of 1 HU is equivalent to the change of 0.1% of the attenuation coefficient of water.

A CT simulator is a CT system that has been specially equipped for use in radiation therapy planning. A CT simulator has a flat-top surface for patient positioning which is identical to the linac treatment couch table top. In addition, a laser marking system is used to link the coordinate system of the CT simulator, and thus the location of the treatment isocentre, with the surface of a patient (e.g., by tattoo markings on the skin). In addition, virtual simulator software (at the CT simulator workstation or in treatment planning software) allows a user to identify the treatment isocentre and digitally reconstruct radiographs. This allows the design of treatment fields, the transfer of patient data to the treatment planning system, and the production of an image for treatment verification (13).

1.3.2 Magnetic Resonance Imaging

MRI has developed along with CT as an important modality for radiation therapy target localization (15). MRI is based on the principle of nuclear magnetic resonance (20, 21). The total angular momentum of a nucleus is often referred to as a nuclear spin. In the presence of a strong magnetic field $\mathbf{B}_0 = B_0\hat{\mathbf{z}}$, where B_0 is the magnetic field strength and $\hat{\mathbf{z}}$ is a unit vector in the z-direction, nuclear spins align parallel (a low-energy state) or antiparallel (a high-energy state) to the magnetic field. This results in a small net macroscopic magnetization $\mathbf{M}$, defined as the total magnetic moment in a unit volume, parallel to the magnetic field. The magnetization precesses around the field at a frequency of $\omega_0 = \gamma B_0$, called the Larmor frequency. The gyromagnetic ratio γ is ratio of the magnetic

dipole moment to its angular momentum for a given atom or system. MRI is most often performed for hydrogen nuclei (protons) since the high concentration of hydrogen in the body and its intrinsic high sensitivity lead to a strong detected signal.

Application of an RF pulse produces a magnetic field perpendicular to $\mathbf{B}_0$. The frequency of the RF pulse must match the Larmor frequency in order for nuclear spins in the low-energy state to transition to the high-energy state. This causes the magnetization to precess around the new magnetic field. The flip angle describes the angle which the magnetization rotates through while the RF pulse is applied. For example, a 90° pulse will rotate a magnetization that is initially aligned parallel to $\mathbf{B}_0$ into the xy-plane. The flip angle can be changed by varying the duration or strength of the RF pulse.

Spin dynamics are described by the Bloch equation:

$$\frac{d\mathbf{M}}{dt} = \gamma \mathbf{M} \times \mathbf{B}_0 - \frac{M_x \hat{\mathbf{x}} + M_y \hat{\mathbf{y}}}{\mathrm{T2}} - \frac{(M_z - M_0)\,\hat{\mathbf{z}}}{\mathrm{T1}}, \tag{1.15}$$

where $\mathbf{M} = M_x \hat{\mathbf{x}} + M_y \hat{\mathbf{y}} + M_z \hat{\mathbf{z}}$. Following the application of an RF pulse, the nuclear spins will return to their original alignment. This process is called relaxation, and is described by the following solution to the Bloch equation (with appropriate boundary conditions):

$$M_\perp = M_0 e^{-t/\mathrm{T2}}, \tag{1.16}$$

$$M_z = M_0 \left(1 - e^{-t/\mathrm{T1}}\right). \tag{1.17}$$

$M_\perp$ is the transverse and M_z is the longitudinal component of the magnetization. M_0 is the magnetization at time $t = 0$. The transverse component of the magnetization produces an induction signal which can be measured by a nearby

receiver coil. The time constant T1 characterizes spin-lattice interactions: the time required for spins in the high-energy state to transfer their energy to the environment or lattice. The time constant T2 characterizes spin-spin interactions: the time for dephasing of spins following the RF pulse. In practice, dephasing of spins is much faster due to magnetic field inhomogeneities, external fields, and local fields induced in the sample being measured. This relaxation is characterized by the time constant $T2^*$.

Imaging is achieved by applying gradient magnetic fields that vary linearly in spatial coordinates, produced by RF coils in three orthogonal directions (15). This varies the Larmor frequency spatially. Localization of a slice (e.g., in the z-direction) is achieved by a slice selection gradient which is applied at the same time as an RF pulse. Localization within a slice is achieved by frequency encoding, the application of transverse gradient in the x-direction during signal acquisition, and phase encoding, the application of a gradient in y-direction prior to signal acquisition. Images are obtained by inverse Fourier transforms.

By varying the timing and strength of RF pulses and gradients, different images can be produced. Using a single pulse (e.g., 90°), the signal measured is called a free induction decay curve. The spin echo sequence consists of a 90° pulse followed by a 180° pulse, which produces an echo of the free induction decay curve at a time that is twice the time between the pulses (22). This time is called the echo time (TE). The time between each 90° pulse is called the repetition time (TR). The signal S from a spin echo sequence can be written as:

$$S = S_0 \left(1 - e^{-\mathrm{TR}/\mathrm{T1}}\right) e^{-\mathrm{TE}/\mathrm{T2}}. \tag{1.18}$$

Different types of images can be achieved using different TE and TR times. T1-weighted images are obtained with $\mathrm{TE} \ll \mathrm{T2}$ and $\mathrm{TR} \approx \mathrm{T1}$, T2-weighted images

are obtained with TR $\gg$ T1 and TE $\approx$ T2, and spin-density (or proton-density) images are obtained with TR $\gg$ T1 and TE $\ll$ T2.

The inversion recovery sequence adds a 180° pulse before the 90° pulse of a spin echo sequence. The time between these pulses is called the inversion time (TI). Assuming a long TR, the longitudinal magnetization M_z at TI is:

$$M_z = M_0\left(1 - 2e^{-\mathrm{TI}/\mathrm{T1}}\right). \tag{1.19}$$

Using the inversion recovery sequence, signals for substances with known T1 values, such as fat, blood, and CSF, can be suppressed by setting $\mathrm{TI} = \mathrm{T1}\ln 2$. The usefulness of T2-weighted imaging of the brain is limited by the fact that white and gray matter signals decays much more rapidly than the signal of CSF and motion of the high-intensity CSF signal can cause image artifacts (23). The fluid attenuated inversion recovery (FLAIR) pulse sequence selective suppresses signal from CSF using TI $\approx$ 2300 ms. This allows clinical interpretation of T2-weighted brain images with reduced image degradation from partial volume effects and motion artifacts (24).

Contrast agents, such as metal chelates of gadolinium, are introduced to enhance relaxation for clinical applications. In the radiation therapy of high-grade gliomas, the target volume is identified using CT and MRI with gadolinium contrast enhancement (11). Enhancement of high-grade gliomas on T1-weighted images arises from blood-brain barrier disruptions which give abnormal vessel permeability to gadolinium (11, 25). Surrounding edema is also apparent on T2-weighted FLAIR images. However, pathological studies have shown that glioma cells can be identified infiltrating the brain beyond the area of contrast enhancement (26). Contrast enhancement is also a nonspecific sign of blood-brain barrier disruptions and cannot accurately differentiate nonspecific post-

surgical changes from residual tumour (27). There is a need for other imaging techniques that can improve glioma target localization.

1.3.3 Positron Emission Tomography

Positron emission tomography (PET) can potentially be used in conjunction with CT and MRI to improve localization of malignant tissue. The main principle of PET is β^+-decay, the decay of a proton into a neutron, positron (antielectron), and electron neutrino:

$$\mathrm{p} \rightarrow \mathrm{n} + \mathrm{e}^+ + \nu_\mathrm{e}\,. \tag{1.20}$$

In a typical PET study, a tracer labeled with a β^+-emitter is introduced to a patient by injection or inhalation (28). The radiotracer enters the bloodstream and is accumulated in the organ of interest. A positron that is emitted travels a short distance in tissue and then annihilates at its first encounter with an electron. The annihilation process results in the emission of two nearly colinear photons with an energy of 511 keV each. Detectors placed at 180° are used to record the arrival of these photons in coincidence (e.g., within a 5–20 ns timing window). The lines of response from coincidence detections form projections which are reconstructed into images.

Modern systems combine PET and CT scanners. The CT scanner allows anatomical localization of the metabolic PET data. Most isotopes used for PET are produced in cyclotrons. Some common isotopes used for PET are shown in Table 1.2. Radiotracers are obtained by attaching these isotopes to clinically-useful biomarkers. PET is therefore a functional imaging technique, since its images are representative of *in vivo* biological processes. For example, ^{18}F-fluorodeoxyglucose (^{18}F-FDG) provides a biomarker for glucose metabolism. ^{18}F-FDG was the first studied radiotracer for PET imaging of brain tumours.

Table 1.2. Physical properties of isotopes used in positron emission tomography.

Isotope	Symbol	Half-life (min)	Ave. Energy (MeV)	Max. Energy (MeV)	Range in water (mm)
Carbon-11	^{11}C	20.3	0.39	0.96	1.1
Nitrogen-13	^{13}N	9.97	0.49	1.19	1.4
Oxygen-15	^{15}O	2.0	0.73	1.7	1.5
Fluorine-18	^{18}F	109.8	0.24	0.63	1.0

Abbreviations: Ave. = average; Max. = maximum.

However, tumour visualization with ^{18}F-FDG is difficult since high glucose uptake in the normal cortex gives low tumour-to-background contrast (29, 30).

Since facilitated transport of amino acids is upregulated in gliomas, PET with radiolabeled amino acids, such as ^{11}C-methionine (^{11}C-MET) and ^{18}F-fluoroethyltyrosine (^{18}F-FET), has been investigated for glioma imaging (31). These radiotracers have been shown to have a more sensitive signal than ^{18}F-FDG, and have uptake outside the diseased volume identified with conventional MRI (29, 30, 32–34).

The radiotracer 3,4-dihydroxy-6-[^{18}F]fluoro-L-phenylalanine (^{18}F-FDOPA) has also been investigated for PET imaging (35). ^{18}F-FDOPA is an analog to 3,4-dihydroxy-L-phenylalanine (L-DOPA), which is the immediate precursor of dopamine, a neurotransmitter that is predominantly found in the nigrostriatal region of the central nervous system (36). Since defects in this region correspond to neurodegenerative and movement disorders, ^{18}F-FDOPA has been used for studies of Parkinson's disease (36–39). In addition, some studies have suggested the use of ^{18}F-FDOPA for the functional evaluation of brain tumours, since the amino acid transport system is highly expressed in brain tumours pathologically, causing an increased uptake of amino acids (29, 36). ^{18}F-FDOPA PET has been shown to have better sensitivity and specificity than ^{18}F-FDG PET

when evaluating both low-grade and high-grade gliomas (29, 38, 40, 41). There is an increase of uptake in high-grade gliomas and the uptake identifies disease not visible on conventional MRI (40, 41). However, unlike ^{11}C-MET and ^{18}F-FET PET, there is intense uptake of ^{18}F-FDOPA in the normal basal ganglia (37).

1.3.4 Diffusion Imaging

MRI can also characterize diffusion of water in the brain. Diffusion is the random motion of molecules due to their thermal energy. The diffusion coefficient D is characterized by Einstein's equation (42, 43):

$$D = \frac{\langle \Delta r^2 \rangle}{2n\Delta t}, \tag{1.21}$$

where $\langle \Delta r^2 \rangle$ is the mean-square distance traveled by a particle in time Δt; n is the number of dimensions. For pure water at 20°C, $D = 2.0 \times 10^{-3}$ mm^2/s. In the absence of boundaries, diffusion in three dimensions follows a Gaussian probability distribution:

$$p(\Delta r, \Delta t) = \frac{1}{\sqrt{(2\pi D\Delta t)^3}} \exp\left(-\frac{\Delta r^2}{4D\Delta t}\right). \tag{1.22}$$

To measure diffusion with MRI, a spin-echo pulse sequence can be used with two gradient pulses added before and after the 180° pulse. This is known as the Stejskal-Tanner experiment (44). The first gradient dephases the spins and the second gradient recombines them. The gradients have no effect in the absence of motion. A spin that is moving will accumulate additional phase. For simple isotropic Gaussian motion, the signal measured from a diffusion weighted image is:

$$S = S_0 e^{-bD}, \tag{1.23}$$

where,

$$b = \gamma^2 \delta^2 G^2 \left(\Delta - \frac{\delta}{3} \right), \tag{1.24}$$

and G is the strength of the gradient pulse, δ is the duration of the gradient pulse, and Δ is the timing between the pulses.

Anisotropic diffusion can be characterized with diffusion tensor imaging (DTI) (45). The probability distribution for anisotropic diffusion is:

$$p(\Delta \mathbf{r}, \Delta t) = \frac{1}{\sqrt{(2\pi \Delta t)^3 \left| \mathbf{D} \right|}} \exp\left(-\frac{\Delta \mathbf{r}^\intercal \mathbf{D}^{-1} \Delta \mathbf{r}}{4 \Delta t} \right), \tag{1.25}$$

where $\mathbf{D}$ the diffusion tensor, a symmetric second-order tensor. To measure the full diffusion tensor, Stejskal-Tanner measurements must be made in at least six noncolinear directions. For a given direction $\hat{\mathbf{g}}_i$, the signal strength S_i is:

$$S_i = S_0 \exp\left(-b_i \hat{\mathbf{g}}_i^\intercal \mathbf{D} \hat{\mathbf{g}}_i \right). \tag{1.26}$$

The six independent elements of the diffusion tensor are estimated using multiple linear least squares methods or nonlinear modeling using apparent diffusivity maps $D_{\text{app},i}$:

$$D_{\text{app},i} = \frac{\ln S_i - \ln S_0}{b_i}, \tag{1.27}$$

where S_i is an image with diffusion weighting b_i and S_0 is an image with no diffusion weighting (42).

The diffusion tensor is diagonalized to find its principle axes and their respective eigenvalues: λ_1, λ_2, and λ_3. Several measures are used to characterize diffusion. The mean diffusivity (MD) is:

$$\text{MD} = \frac{\lambda_1 + \lambda_2 + \lambda_3}{3}. \tag{1.28}$$

The MD is often referred to as the apparent diffusion coefficient (ADC). It reflects the magnitude of diffusion (i.e., how far a water molecule diffuses during measurement). The fractional anisotropy (FA) is:

$$\mathrm{FA} = \sqrt{\frac{3}{2} \cdot \frac{(\lambda_1 - \mathrm{MD})^2 + (\lambda_2 - \mathrm{MD})^2 + (\lambda_3 - \mathrm{MD})^2}{\lambda_1^2 + \lambda_2^2 + \lambda_3^2}}. \tag{1.29}$$

It is a rotationally-invariant measure of the degree to which the diffusivities are a function of the diffusion-weighting encoding direction (42, 46). Some studies alternatively will define the axial diffusivity $\lambda_{\|}$, which the largest eigenvalue of the diffusion tensor (e.g., $\lambda_{\|} = \lambda_1$), and radial diffusivity $\lambda_{\perp}$, which is the average of the two smaller eigenvalues ($\lambda_{\perp} = (\lambda_2 + \lambda_3)/2$).

1.4 Radiation Therapy Planning

1.4.1 Planning Volumes and Dose Prescription

Images obtained during CT simulation for radiation therapy planning are imported into treatment planning systems and the outlines of the patient surface, the tumour volume that will be treated, and tissues and organs that need to be avoided are contoured. Although the contouring process is CT-based, other images (MRI and PET) can also be imported, fused, and used for the treatment planning process. The following treatment planning volumes defined by the ICRU Reports 50 and 62 (47, 48) are used for radiation therapy planning:

- Gross tumour volume (GTV): The visible, palpable, or demonstrable extent or location of the tumour.
- Clinical target volume (CTV): The GTV plus a margin to account for the suspected microscopic spread of disease. The CTV is an anatomical and

clinical volume, which is independent of the treatment modality or technique selected.

- Planning target volume (PTV): The CTV plus margins to account for expected physiologic movements and variations in size, shape, and position of the CTV during therapy (the internal margin), and uncertainties in patient positioning and alignment of beams (the set-up margin). The PTV is a geometrical concept, which depends on the modality and technique used for treatment. The dose variation in the PTV is generally required to be between 95% to 107% of the prescribed dose for conventional fractionation schemes (e.g., 2 Gy/fraction).

- Organs at risk (OARs): Normal tissues whose radiation sensitivity may significantly influence treatment planning and/or prescribed dose. For critical organs, a margin to account for set-up errors may be also applied to create a planning organ at risk volume (PRV).

The target volumes for high-grade glioma radiation therapy are identified using CT and MRI: T1-weighted images with gadolinium contrast enhancement and T2-weighted images (11, 25). However, it is known that tumour cells infiltrate beyond the area of gadolinium contrast enhanced on T1-weighted images (26). It is believed that the edema volume overestimates the tumour volume. Thus, two protocols have emerged for target volume definition and dose prescription.

The European Organisation for Research and Treatment of Cancer protocol 26052-22053 (49) defines the GTV as the contrast-enhancing tumour visible on T1-weighted MRI. The CTV is defined as a 2-cm expansion of the GTV and postsurgical tumour bed. Edema visible on T2-weighted images is included in

the CTV. The PTV is a 0.5-cm expansion of the CTV, and a dose of 60 Gy in 30 daily fractions is prescribed.

The Radiation Therapy Oncology Group (RTOG) 0825 protocol (50) defines two GTVs: GTV1 and GTV2. GTV1 is defined as the abnormality seen on T2-weighted images. GTV2 is defined by the contrast-enhancement seen on T1-weighted images. The clinical target volumes CTV1 and CTV2 are defined by 2-cm expansions of GTV1 and GTV2, respectively. The planning target volumes PTV1 and PTV2 are additional expansions of 3 to 5 mm, depending on the localization method and set-up reproducibility of CTV1 and CTV2. The prescribed doses are 46 Gy in 23 fractions for PTV1 and 60 Gy in 30 fractions for PTV2. The appropriate contouring protocol for glioma radiation therapy remains unclear. Several authors have advocated using smaller margins than those in the RTOG guidelines since currently observed outcomes have failed to demonstrate a preferred method of prescription (51–53).

1.4.2 Treatment Planning Techniques

With three-dimensional anatomical information available from CT, modern radiation treatments of high-grade gliomas are delivered with three-dimensional conformal radiation therapy (3D-CRT), intensity modulated radiation therapy (IMRT), or volumetric modulated arc therapy (VMAT) (9, 49, 54). In general, 3D-CRT refers to treatments that use three-dimensional anatomical information to obtain dose distributions which conform as closely as possible to the target volume while minimizing dose in normal tissues (15).

Optimization of 3D-CRT plans is completed in a forward planning process. In treatment planning systems, after the target volume and normal tissues are delineated, a user selects the beam arrangement, shapes fields using beam's-

eye-view visualizations, and selects beam energies, beam weights, and any modifiers (e.g., wedges or compensators) that will be placed in the field. A three-dimensional dose calculation is then performed. If the treatment plan does not meet required constraints, the user manually changes the parameters and recalculates the dose. This process is iterated in a trial-by-error fashion until an acceptable plan is produced. For complex cases, this process can be labour intensive.

The flattening filter of a linac generates beam profiles that are uniform. In general, IMRT refers to the use of radiation beams with non-uniform fluences to deliver a conformal dose to the target. This can be achieved using dynamic MLCs and scanned elementary beams of variable intensity (15). Modern IMRT plans are optimized by inverse planning, where each beam is divided into a large number of beamlets and the beamlet weights or intensities are optimized by treatment planning systems to satisfy dose distribution criteria for the target volume and OARs (15, 55).

The computer-controlled MLC can produce intensity modulation in a number of ways. In step-and-shoot IMRT, the treatment fields are sub-divided into subfields, which are irradiated with uniform intensity (56). The subfields are delivered sequentially by the linac without operator intervention, with the beam off while the MLC moves between subfields. The sum of the dose delivered by these subfields results in intensity modulation. Dynamic delivery, also referred to as a sliding window, leaf-chasing, camera-shutter, or sweeping-variable gap, refers to a technique where corresponding (moving) leaves sweep across the field simultaneously and unidirectionally, each leaf traveling with a different time-dependent velocity (15). Tomotherapy is an IMRT technique in which a patient is treated slice-by-slice, analogous to a CT scanner, by intensity-modulated

beams (57). The slice size is variable and intensity modulation is achieved using a binary MLC.

Intensity modulation can also be achieved with arc therapies, where the beam is delivered while the gantry rotates around the patient. Intensity modulated arc therapy was the first technique in which the MLC was used dynamically to shape the treatment fields while the gantry rotated (58, 59). Developed by Otto (60), VMAT also obtains intensity modulation of a field in a single treatment arc with a dynamic MLC with the plan inversely optimized by direct-aperture optimization (61). VMAT is the precursor to the RapidArc system available commercially from Varian Medical Systems, Inc.

1.4.3 Treatment Plan Optimization

IMRT treatment plan optimization is achieved through dose-volume constraints obtained from dose volume histograms (DVHs), each assigned its own priority. A DVH is a plot of the differential or cumulative volume of a target or normal structure that receives a given dose. Dose and volume data in DVHs is represented in either absolute terms (e.g., Gy and cm^3) or as percentages of the prescribed dose or total structure volume. V_x (or $V_{x\%}$) is the volume of a structure that receives a dose of at least of x (x% of the prescribed dose). D_x (or $D_{x\%}$) is the minimum dose received by the hottest x (x%) volume of a structure. Care must be taken in interpreting DVH data since it does not give any information on the spatial distribution of dose. In addition, DVH data expressed as percentages must be examined carefully for cases where an entire structure may not have been contoured. Dose-volume parameters used for high-grade glioma treatment planning are shown in Table 1.3.

Table 1.3. DVH constraints used for intensity-modulated radiation therapy of high-grade gliomas.

Structure	Type	DVH Constraint
PTV	Target	$V_{95\%} \geq 98\%$
Optic Chiam and Nerve	OAR	$V_{54\ \mathrm{Gy}} \leq 1\%$
Brainstem	OAR	$D_{\mathrm{max}} = 60$ Gy
Retina	OAR	$D_{\mathrm{max}} = 45$ Gy
Anterior Chamber	OAR	$D_{\mathrm{max}} = 10$ Gy

Abbreviations: DVH = dose volume histogram; max = maximum; OAR = organ at risk.

Dose-volume constraints used for IMRT optimization are driven by treatment outcomes. The goal is to obtain an IMRT plan will all constraints fulfilled. This is done by minimization of an objective function. Minimization of the mean square deviations between the actual dose distribution and the dose-volume constraints is one the most common objective function used for IMRT planning, which penalizes voxels in the dose distribution that do not meet the dose-volume constraints placed on the OARs and target volumes (62).

1.4.4 Radiobiological Models

Dose-volume constraints used in IMRT plan optimization are surrogates for patient outcomes following radiation therapy. Radiobiological models can also be used to evaluate treatment plans. Radiobiological models for normal tissues account for organ architecture. Radiobiological tumour models account for the effects of proliferation; more advanced tumour models account for the tumour microenvironment (e.g., hypoxia). Biological response can ultimately be connected to cell kill.

Cell survival after irradiation can be described using the linear quadratic model (63). The general expression for the surviving fraction (SF) of cells after

receiving a dose D is

$$\mathrm{SF} = e^{-\alpha D - \beta G D^2 + \gamma T}\,, \tag{1.30}$$

where G is the Lea-Catcheside factor, T is the treatment time, $\gamma = \ln 2/T_d$, and T_d is time it takes for the number of tumour cells to double. The factors α and β are radiosensitivity parameters which characterize yields of lethal lesions produced through single-track or double-track pathways following radiation-induced damage in deoxyribonucleic acid. Clinical data for gliomas suggests that $\alpha = 0.06 \pm 0.05$ Gy^{-1} and $\alpha/\beta = 10.0 \pm 15.1$ Gy (64).

The Lea-Catcheside factor G accounts for changes in cell lethality due to fractionation or protracted irradiation (65). Assuming exponential repair,

$$G = \frac{2}{D}\int_{-\infty}^{\infty} \dot{D}(t)\,dt \int_{-\infty}^{t} e^{-\lambda(t-t')}\dot{D}(t')\,dt'\,, \tag{1.31}$$

where $1/\lambda$ is the typical lifetime for a sublethal lesion. For fractionated treatments, $G = 1/n_f$ where n_f is the number of fractions. This assumes that that time between fractions is $\gg 1/\lambda$ (each fraction acts independently) and the time to deliver the dose for one fraction is $\ll 1/\lambda$ (an acute exposure); i.e., no repair of sublethal lesions while the beam is delivered. Neglecting tumour cell proliferation, SF for fractionated treatments is:

$$\mathrm{SF} = e^{-\alpha D - \beta D^2/n_f} = e^{-\alpha D - \beta d D}\,, \tag{1.32}$$

where $d = D/n_f$ is the dose delivered per fraction. In terms of the surviving fraction SF_2 of cells after receiving a single dose of 2 Gy and α/β,

$$\mathrm{SF} = \mathrm{SF}_2^{\frac{D_i}{D_{\mathrm{ref}}}\cdot\frac{\alpha/\beta + D_i/n_f}{\alpha/\beta + D_{\mathrm{ref}}}}\,. \tag{1.33}$$

A limitation of the linear quadratic model is that it predicts that the survival curve continuously bends, which does not agree with experimental data (66, 67). For an acute irradiation, the linear quadratic model overpredicts cell kill above a certain cell-type dose threshold; for mammalian cells, a threshold of 12–15 Gy is reasonable (68, 69).

The biologically equivalent dose (BED), also referred to as the extrapolated response dose, is used to compare the biological effectiveness of radiation therapy schemes. The BED is the dose that if delivered in a protracted fashion will lead to same cell survival as the actual dose delivery scheme:

$$\mathrm{BED} = -\frac{\ln \mathrm{SF}}{\alpha}. \tag{1.34}$$

For fractionated treatments without accounting for proliferation:

$$\mathrm{BED} = D\left(1 + \frac{d}{\alpha/\beta}\right). \tag{1.35}$$

If two fractionation schemes lead to the same BED, it is assumed that they lead to the same biological response.

A related quantity is the normalized total dose (NTD), which is the total dose if given in 2-Gy fractions that is biologically equivalent to a total dose D delivered in fractions of size d:

$$\mathrm{NTD} = D\left(\frac{\alpha/\beta + d}{\alpha/\beta + 2\ \mathrm{Gy}}\right). \tag{1.36}$$

The NTD is often used since dose response is well established for fractionation schemes of 2 Gy per fraction.

Biological response to treatments can be estimated using the tumour control probability (TCP), the proportion of patients who show local control for a given

dose, and the normal tissue complication probability (NTCP), the proportion of patients who show complication of a certain grade. NTCP is popularly characterized with the Lyman-Kutcher-Burman model (70). TCP can be characterized by a Poisson-based model or logistic equation (71).

In addition, the equivalent uniform dose (EUD) can be used for assessment of radiation therapy plans. The EUD is the dose that if given uniformly to a structure will give the same biological effect as the actual heterogeneous dose distribution delivered, assuming that the same dose per fraction is maintained during treatment (72). Using a cell killing-based model with the linear quadratic formalism, the EUD can be calculated from:

$$\sum_{i=1}^{N} V_i \cdot \rho_i \cdot \mathrm{SF}_2^{\frac{\mathrm{EUD}}{D_{\mathrm{ref}}} \cdot \frac{\alpha/\beta + \mathrm{EUD}/n_f}{\alpha/\beta + D_{\mathrm{ref}}}} = \sum_{i=1}^{N} V_i \cdot \rho_i \cdot \mathrm{SF}_2^{\frac{D_i}{D_{\mathrm{ref}}} \cdot \frac{\alpha/\beta + D_i/n_f}{\alpha/\beta + D_{\mathrm{ref}}}} . \tag{1.37}$$

Solving for EUD gives

$$\mathrm{EUD} = \frac{n_f}{2} \left[-\frac{\alpha}{\beta} + \sqrt{\left(\frac{\alpha}{\beta}\right)^2 + 4 \cdot \frac{D_{\mathrm{ref}}}{n_f} \cdot \left(\frac{\alpha}{\beta} + D_{\mathrm{ref}}\right) \cdot \frac{\ln A}{\ln \mathrm{SF}_2}} \right] , \tag{1.38}$$

where

$$A = \sum_{i=1}^{N} V_i \cdot \rho_i \cdot \mathrm{SF}_2^{\frac{D_i}{D_{\mathrm{ref}}} \cdot \frac{\alpha/\beta + D_i/n_f}{\alpha/\beta + D_{\mathrm{ref}}}} \Bigg/ \sum_{i=1}^{N} V_i \cdot \rho_i \tag{1.39}$$

and D_i is the total dose delivered in n_f fractions to a given voxel with volume V_i and tumour cell density ρ_i. N is the total number of dose matrix voxels in the structure. The surviving fraction SF_2 of cells after receiving a single dose of $D_{\mathrm{ref}} = 2$ Gy and the radiosensitivity parameter α/β are assumed to be the same for all voxels.

The EUD in Eq. 1.38 is applicable to target volumes. A generalized EUD for target volumes and OARs is given by (73):

$$\mathrm{EUD} = \left(\sum_{i=1}^{N} v_i D_i^a \right)^{1/a}, \tag{1.40}$$

where v_i is the relative volume of a structure that receives a dose D_i, obtained from a differential DVH. The parameter a describes the volume-effect for organs. To minimize the effect of cold spots (regions of low dose), a is taken as negative ($a < -10$) for tumours. For serial organs, such as the spinal cord and optic nerve, whose complications depends highly on the maximum dose delivered, a is large ($a > 10$). For parallel organs, such as lung and kidney, the mean dose is predictive of normal tissue complication ($a \approx 1$) (74). Therefore, the EUD for parallel organs approaches the mean dose, whereas for serial organs it approaches maximum dose.

Advances in patient imaging may allow the incorporation of biological information into radiation therapy planning. Ling et al. (75) first proposed this approach as multidimensional radiotherapy, suggesting that biological information from functional images can be introduced to radiation therapy planning by introduction of a biological target volume (BTV). The BTV can be used to identify regions within the target volume, such as regions of greater tumour cell density, cell proliferation, or radioresistance, which may benefit from radiation dose boosts. IMRT allows the planned dose distribution to a BTV to be optimized by dose painting, where the dose distribution is optimized to conform to the biological information obtained from functional imaging techniques (75, 76). Biological models can also be incorporated into IMRT treatment planning by using an objective function based on EUD, TCP, or NTCP (73, 77).

1.5 Project Outline

Biological information from functional imaging techniques, such as PET and DTI, can potentially be used to improve localization of malignant tissue as well as for biologically-based treatment planning. This project investigated the utility of target localization using uptake of ^{18}F-FDOPA and interhemispheric difference images obtained by DTI, and explored the possibility for a unique biologically-guided, physically-based radiation therapy planning technique for high-grade gliomas.

First, a contouring study was completed to determine the utility of ^{18}F-FDOPA PET for radiation therapy planning of high-grade gliomas. PET with ^{18}F-FDOPA visualizes glioma that is not clearly identified on MRI. In a study of 19 patients, consensus target volumes obtained from five observers using ^{18}F-FDOPA PET and MRI were compared with the location of recurrences following radiotherapy. Simultaneous truth and performance level estimation (STAPLE) was used to calculate consensus target volumes from the observers' delineations and interobserver variations of MRI-based and PET-based delineations were quantified. Recurrence volumes following radiotherapy were contoured by each observer and consensus recurrence volumes calculated using STAPLE were compared with the consensus target volumes.

The second study aimed to determine if FA or MD images obtained from postoperative DTI can be used to improve radiation therapy target localization of gliomas. This was done first by characterizing the distribution of FA and MD in the tumour target volumes, obtained from T1-weighted and T2-weighted MRI images. In addition, the distribution of FA and MD was characterized in regions of interest (ROIs) that were peritumoural shells around the target volume, and were compared with the values of contralateral normal brain. In addition,

a method was implemented to automatically calculate FA and MD interhemispheric difference images for potential use for radiation therapy planning.

Lastly, a treatment planning study compared VMAT treatment plans for high-grade gliomas using a unique biologically-guided, physically-based treatment planning technique. This was accomplished by dose painting by contours using ^{18}F-FDOPA PET with dose constraints for each contour specified by a radiobiological model. This method was compared with VMAT plans obtained with conventional MRI-based target volume contours to determine the potential benefit, if any, can be realized with biological-based treatment planning of high-grade gliomas, while maintaining acceptable avoidance of critical structures in the brain.

Chapter 2

Contouring with ^{18}F-FDOPA Positron Emission Tomography

2.1 Introduction

As standard practice in the radiation therapy of high-grade gliomas, the target volume is identified using postoperative computed tomography (CT) and magnetic resonance imaging (MRI) with intravenous contrast. The area of gadolinium contrast enhancement on T1-weighted MRI is often used to define gross tumour extent radiologically. However, several pathological studies have shown that the contrast enhancement may not represent the outer tumor border since infiltrating glioma cells can be identified well beyond the area of enhancement (26). Gadolinium contrast enhancement is also a nonspecific sign of blood-brain barrier disruptions and cannot accurately differentiate nonspecific postsurgical changes from residual tumour (27).

Positron emission tomography (PET) can potentially be used in conjunction with CT and MRI to improve localization of malignant tissue. The amino acid tracer 3,4-dihydroxy-6-[^{18}F]fluoro-L-phenylalanine (^{18}F-FDOPA) is taken up by cells using a specific amino acid transport system, rather than breakdown of the blood-brain barrier (31). Increased protein synthesis and upregulation of amino acid transport in the supporting vasculature of brain tumour tissue is re-

sponsible for increased ^{18}F-FDOPA uptake in tumour cells. ^{18}F-FDOPA is also taken up by the dopaminergic system, resulting in increased activity seen in the basal ganglia. Amino acid tracers, such as ^{11}C-methionine (^{11}C-MET), ^{18}F-fluoroethyltyrosine (^{18}F-FET), and ^{18}F-FDOPA, are more useful for PET imaging of brain tumours than ^{18}F-fluorodeoxyglucose (^{18}F-FDG) because of high uptake in tumour tissue and low uptake in normal brain tissue, giving better tumour-to-normal-tissue contrast (30, 32, 33, 40, 78). ^{18}F-FDOPA PET/CT also provides accurate anatomic localization of newly diagnosed and recurrent, low-grade and high-grade gliomas when fused with MRI and treatment planning CT (41). It has also been shown to identify regions of high cellular density and higher-grade disease in newly diagnosed and recurrent astrocytomas (79). Thus, the addition of ^{18}F-FDOPA PET/CT to treatment planning may translate into clinically significant improvements in radiation therapy outcomes.

Interobserver variations in target volume contouring also have important implications for radiation therapy delivery and outcome. Recent brain segmentation studies (80, 81) have used simultaneous truth and performance level estimation (STAPLE) to estimate consensus volumes from delineations of multiple observers. STAPLE iteratively calculates a probabilistic estimate of the consensus volume by an expectation maximization algorithm that for each observer optimizes the sensitivity (the relative frequency that an observer includes a voxel in their contour when that voxel is inside the consensus volume) and specificity (the relative frequency that an observer does not include a voxel when it is outside the consensus volume) (82).

The objective of this study was to compare the post-radiation therapy delineation of recurrences with pre-radiation therapy delineation of newly diagnosed high-grade gliomas from the gadolinium contrast enhancement of T1-weighted

MRI and ^{18}F-FDOPA PET/CT using contours from five observers by calculating consensus target volumes using STAPLE.

2.2 Methods and Materials

2.2.1 Patient Characteristics and Treatment Planning Imaging

Nineteen patients with newly diagnosed high-grade gliomas underwent radiation therapy treatment planning with postoperative CT and T1-weighted MRI with gadolinium contrast enhancement. ^{18}F-FDOPA PET/CT images were also obtained at the time of treatment planning. Institutional research ethics board approval was obtained for all image protocols and all subjects provided written informed consent. Eligible patients had a new diagnosis of World Health Organization (WHO) grade III or IV glioma and Karnofsky Performance Status of 60 or better. Patients were ineligible if they were on medications for Parkinson's disease or had contraindications to contrast-enhanced MRI or radiation therapy. T2-weighted fluid attenuated inversion recovery (FLAIR) images were also obtained for 16 patients (84%). Patient, tumour, and therapy characteristics are shown in Table 2.1. The time between surgery, imaging, and radiation therapy start date is also shown in Table 2.1.

MRI was obtained with a 1.5-T Siemens Magnetom Symphony Tim system (Siemens Healthcare, Erlangen, Germany). For 16 patients (84%), T1-weighted images with gadolinium contrast enhancement were obtained with the turbo spin echo (TSE) sequence (echo time (TE) = 14 ms, pixel resolution = 1 mm, slice thickness = 3 mm) and T2-weighted FLAIR images were obtained (TE = 97 ms, pixel resolution = 0.5 mm, slice thickness = 3 mm). For the remaining three patients (16%), only T1-weighted images with gadolinium contrast en-

Table 2.1. Patient, tumour, and therapy characteristics.

No. of Patients	19
Sex	
Female	8 (42%)
Male	11 (58%)
Age, median (range)	52 (19–74) years
Histology	
Glioblastoma	12 (63%)
Anaplastic astrocytoma	4 (21%)
Anaplastic oligodendroglioma	3 (16%)
Extent of resection	
Gross total resection	9 (47%)
Partial resection	6 (32%)
Biopsy-only	4 (21%)
Chemotherapy	17 (89%)
Dose prescription and fractionation	
60 Gy in 30 fractions	10 (53%)
59.4 Gy in 33 fractions	8 (42%)
40 Gy in 15 fractions	1 (5%)
Time, median (range)	
Surgery to MRI	23 (9–48) days
Surgery to PET/CT	28 (10–48) days
Surgery to radiation therapy start date	34 (20–55) days

Abbreviations: CT = computed tomography; MRI = magnetic resonance imaging; PET = positron emission tomography.

hancement were obtained using the magnetization-prepared rapid acquisition with gradient echo sequence (TE = 3.5 ms, pixel spacing = 1 mm, slice thickness = 1 mm). Radiation therapy planning CT images were also obtained for all patients with a 3-mm slice thickness.

^{18}F-FDOPA was synthesized using a previously published procedure (83). The PET/CT images were obtained with a Siemens Biograph-16 Hi-Rez PET/CT system (Knoxville, TN). All patients fasted for a minimum of six hours prior to intravenous injection of 3.5 MBq/kg of ^{18}F-FDOPA. The patient's head was immobilized on the scanner table and dedicated noncontrast CT and 15 minute

three-dimensional emission PET images were obtained of the brain 40 minutes following injection. The attenuation corrected PET data was reconstructed using an iterative ordered-subset expectation maximization algorithm (matrix: 336 × 336, brain mode, zoom: 2.5, subsets: 8, iterations: 6, Gaussian filter: 2 mm). Reconstructed CT and PET image sets were exported to Siemens and Segami (Segami Corporation, Columbia, MD) workstations for clinical interpretation. All image sets (planning CT, MRI, and PET/CT) were imported into Eclipse treatment planning system (Varian Medical Systems, Palo Alto, CA) and fused using the Eclipse registration package. The planning CT images were fused both to the MRI and the CT image set of the PET/CT.

2.2.2 Radiation Therapy Planning

All study subjects received standard radiation therapy to MRI-defined target volumes contoured by their attending radiation oncologist. Twelve patients (63%) were treated with three-dimensional conformal radiation therapy (3D-CRT) with 6-MV or 10-MV photon beams. Coplanar intensity modulated radiation therapy (IMRT) plans were implemented for treatment for one patient (5%) with five fields and for three patients (16%) with seven fields of 6-MV photons. Three patients (16%) were planned and treated with volumetric modulated arc therapy (VMAT) using 6-MV photons. The IMRT and VMAT treatment planning techniques and objectives have been described earlier (49). The radiation therapy dose prescription was 60 Gy in 30 fractions for 10 patients (53%) and 59.4 Gy in 33 fractions for 8 patients (42%). One patient (5%) received an abbreviated course of 40 Gy in 15 fractions. Seventeen (89%) patients also received standard concurrent and adjuvant chemotherapy with temozolomide.

Five qualified radiation neuro-oncologists delineated the gross tumour volume (GTV) using T1-weighted MRI and ^{18}F-FDOPA PET while blinded to the original planning contours used for treatment. The PET imaging display window and level were determined by matching the ^{18}F-FDOPA uptake in the basal ganglia with anatomic MRI-based contours of the basal ganglia for each subject. Observers were not permitted to change the PET imaging display window and level. They each received training before the study and were advised about how to minimize uncertainty of contouring the PET GTVs in the vicinity of the basal ganglia and in the presence of postoperative inflammation. Each observer contoured an MRI-based GTV, defined as the volume of gadolinium contrast enhancement excluding the surgical cavity. A PET-based GTV was defined as the volume of ^{18}F-FDOPA PET uptake excluding the surgical cavity. A combined MRI-PET GTV was defined as the union of both MRI GTV and PET GTV. This definition was included since the study design anticipated that a clinician would not omit an enhancing abnormality on MRI from a PET-defined volume during radiation therapy treatment planning. Clinical target volumes (CTVs) were defined as a 2-cm isotropic expansion of the union of the GTV and the surgical cavity, cropped to exclude any portion lying outside the brain (10). Planning target volumes (PTVs) were defined as 0.5-cm isotropic expansions of the CTVs. Examples of these structures are shown in Figure 2.1.

2.2.3 Consensus Contours

Consensus contours were obtained by STAPLE (82) using in-house software created with MATLAB (version 7.0.0.19920; The MathWorks, Inc., Natick, MA). The contours made by each observer were described by a binary decision matrix $\mathbf{D}$, where $D_{ij} = 1$ if image voxel i was included inside observer j's contour

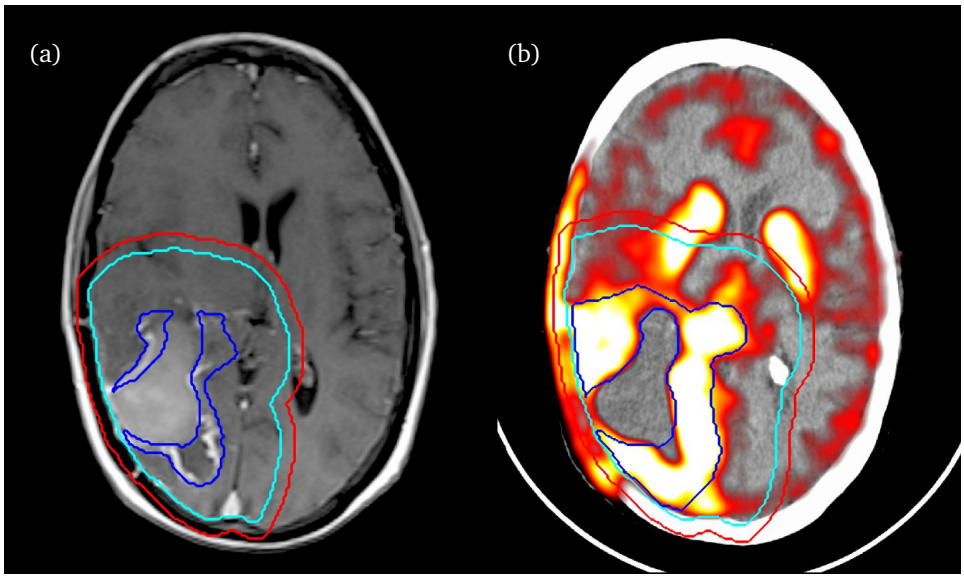

Figure 2.1. The gross tumour volume (blue), clinical target volume (cyan), and planning target volume (red) obtained from (a) extent of gadolinium contrast enhancement on T1-weighted magnetic resonance imaging and (b) ^{18}F-FDOPA positron emission tomography uptake contoured by one observer.

and $D_{ij} = 0$ if the voxel was not included inside observer j's contour. STAPLE estimated the performance level parameters p_j and q_j of each observer's segmentation by finding the parameters which maximized a log likelihood function

$$(\hat{\mathbf{p}}, \hat{\mathbf{q}}) = \arg \max_{\mathbf{p},\mathbf{q}} \ln f(\mathbf{D}, \mathbf{T}|\mathbf{p}, \mathbf{q}), \tag{2.1}$$

where T_i was the hidden binary true segmentation for each voxel, p_j was the sensitivity for an observer's segmentation (relative frequency that $D_{ij} = 1$ when $T_i = 1$), and q_j was the specificity for an observer's segmentation (relative frequency than $D_{ij} = 0$ when $T_i = 0$).

The complete log likelihood function $\ln f(\mathbf{D}, \mathbf{T}|\mathbf{p}, \mathbf{q})$ was not known since $\mathbf{T}$ was unknown. The performance level parameters were found using an expectation maximization algorithm. The details of these steps are discussed by

Warfield et al. (82). In brief, first a conditional expectation of the complete log likelihood function was computed and then the parameters that maximize this function were identified.

The conditional expectation of the complete log likelihood function was computed (E-step) using:

$$W_i^{(k-1)} = f(T_i = 1 | \mathbf{D_i}, \mathbf{p}^{(k-1)}, \mathbf{q}^{(k-1)}) \tag{2.2a}$$

$$= \frac{a_i^{(k-1)}}{a_i^{(k-1)} + b_i^{(k-1)}} \tag{2.2b}$$

where

$$a_i^{(k)} = f(T_i = 1) \prod_{j:D_{ij}=1} p_j^{(k)} \prod_{j:D_{ij}=0} (1 - p_j^{(k)}), \tag{2.3a}$$

$$b_i^{(k)} = f(T_i = 0) \prod_{j:D_{ij}=0} q_j^{(k)} \prod_{j:D_{ij}=1} (1 - q_j^{(k)}). \tag{2.3b}$$

W_i was the probability that the $T_i = 1$; it was the normalized product of a prior probability that the voxel was inside the true segmentation, the sensitivity of all observers that included that voxel inside their segmentation, and $1-$sensitivity of all observers that excluded the voxel from their segmentation. The prior estimates of the sensitivity and specificity were initialized with values very close but not equal to one:

$$p_j^{(0)} = q_j^{(0)} = 0.9999\,. \tag{2.4}$$

For simplicity, a uniform prior probability was used:

$$f(T_i = 1) = \frac{1}{RN} \sum_{j=1}^{R} \sum_{i=1}^{N} D_{ij}\,, \tag{2.5}$$

where $R = 5$ was the number of observers and N was the total number of voxels in a region of interest (ROI) around the contours. The ROI was chosen to be the smallest box that encompassed all contours to ensure that most voxels that all observers did not include in their contour were not included in the calculations.

The performance level parameters that maximized the conditional expectation of the complete log likelihood function were then calculated (M-step) using the equations:

$$p_j^{(k)} = \frac{\sum_{i:D_{ij}=1} W_i^{(k-1)}}{\sum_i W_i^{(k-1)}}, \tag{2.6a}$$

$$q_j^{(k)} = \frac{\sum_{i:D_{ij}=0} \left(1 - W_i^{(k-1)}\right)}{\sum_i \left(1 - W_i^{(k-1)}\right)}. \tag{2.6b}$$

The E-step (Eq. 2.2) and M-step (Eq. 2.6) were iterated until the sum

$$S_k = \sum_{i=1}^{N} W_i^{(k)}, \tag{2.7}$$

converged ($S_k - S_{k-1} < 10^{-12}$).

Consensus contours were then obtained using a voxel-wise maximum likelihood approach (84). An example of the consensus PET GTV contour obtained from the contours of five observers is shown in Figure 2.2.

2.2.4 Interobserver Variability

Interobserver contour variability was quantified by the percentage of volume overlap defined as the ratio of the volume common to all contours to the volume

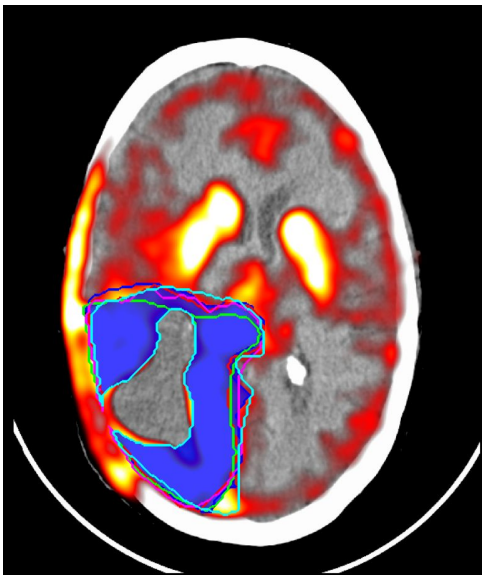

Figure 2.2. The consensus volume (blue wash) obtained from the positron emission tomography gross tumour volume contours of five observers (red, blue, green, cyan, and magenta) using simultaneous truth and performance level estimation.

encompassed by all contours:

$$\text{volume overlap} = \frac{\text{common volume}}{\text{encompassing volume}} \times 100\%. \tag{2.8}$$

The definition of the common and encompassing volumes is illustrated in Figure 2.3. In the case of two overlapping contours, the volume overlap is equivalent to the Jaccard index (85, 86). The STAPLE sensitivity and specificity (Eq. 2.6) values were also used to quantify interobserver contour variability. Differences between MRI and PET interobserver volume overlap were tested using a two-sided paired t-test ($\alpha = 0.05$).

Differences in the volume of the consensus MRI, PET, and MRI-PET contours were quantified using linear regression and statistically tested using two-sided paired t-tests ($\alpha = 0.05$). The overlap of consensus MRI CTVs and PET GTVs

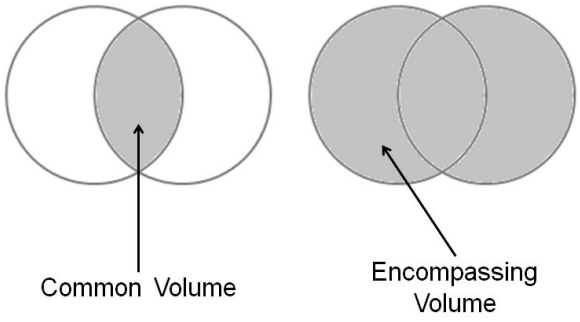

Figure 2.3. The definition of the common and encompassing volumes is illustrated using two contours.

were also compared to determine if the standard 2-cm margin from MRI GTV to MRI CTV encompassed ^{18}F-FDOPA uptake. This was done to determine if radiation therapy planning with only MRI would result in a geographic miss of the PET GTV.

2.2.5 Recurrence Imaging

Recurrence imaging was available for 12 patients (10 MRI and 2 CT), with a median follow-up time of 4.6 months (range, 2.3–20 months). Recurrence image sets were fused to the planning CT volume and recurrences following radiation therapy were contoured by each observer with each observer blinded to the previous contours. Consensus recurrence volumes were obtained using STAPLE. Patterns of failure were classified as central (>95% of consensus recurrence volume within 95% isodose), in-field (80–95% within 95% isodose), marginal (20–80% within 95% isodose), or outside (<20% within 95% isodose) (87). Consensus recurrence volumes were compared with margins of 0 cm, 1.5 cm, 2 cm, and 2.5 cm on the consensus MRI and PET GTV and the percentage of recurrence volume extending outside the consensus MRI and PET GTV was calculated.

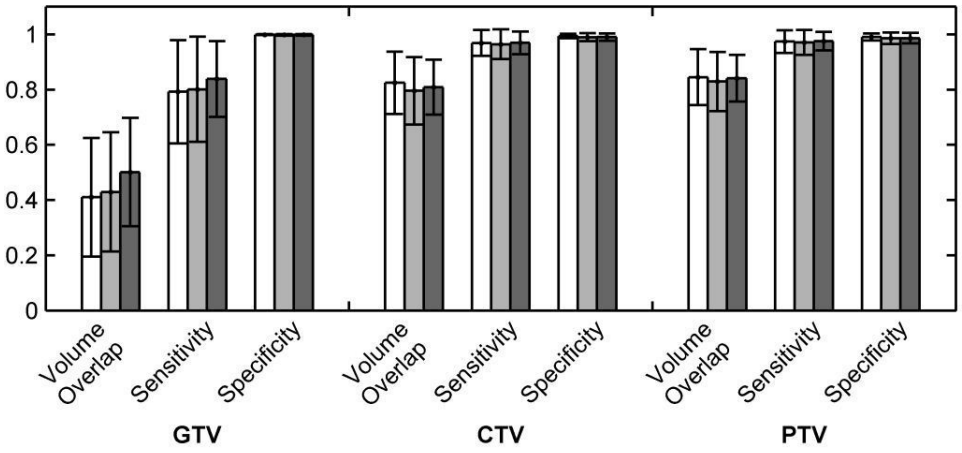

Figure 2.4. The mean interobserver volume overlap, and STAPLE sensitivity and specificity values are shown for the gross tumour volume (GTV), clinical target volume (CTV), and planning target volume (PTV) delineated on magnetic resonance imaging (MRI) (white), positron emission tomography (PET) (light gray), and both MRI-PET (dark gray). Standard deviations are shown by error bars.

2.3 Results

Interobserver volume overlap and STAPLE sensitivity and specificity values are shown for the MRI, PET, and MRI-PET target volumes in Figure 2.4. The mean interobserver volume overlap of PET GTV contours ($42\% \pm 22\%$) was not significantly different from the mean interobserver volume overlap of MRI GTV contours ($41\% \pm 22\%$, $p = 0.67$). The mean interobserver volume overlap of PET CTV ($80\% \pm 12\%$) and MRI CTV ($82\% \pm 11\%$) contours were not significantly different ($p = 0.25$). Similarly, the difference in mean interobserver volume overlap of PET PTV ($82\% \pm 11\%$) and MRI PTV ($85\% \pm 10\%$) contours was not statistically significant ($p = 0.50$).

Consensus target volumes obtained from MRI, PET, and MRI-PET, as well as paired statistics are shown in Table 2.2. The mean volume of the consensus PET GTV was 58.6 ± 52.4 cm^3 and consensus MRI GTV was 30.8 ± 26.0 cm^3

Table 2.2. Consensus target volumes obtained from MRI, PET, and MRI-PET, as well as p-values from paired t-tests.

Consensus Structure	Volume (cm^3)			p-value		
	MRI	PET	MRI-PET	MRI & PET	MRI & MRI-PET	PET & MRI-PET
Recurring cases ($n = 12$)						
GTV	23.1 ± 12.2	46.0 ± 32.1	51.2 ± 30.5	0.010	0.001	0.04
CTV	214 ± 73	265 ± 98	270 ± 98	0.003	0.001	0.04
PTV	325 ± 97	389 ± 123	395 ± 123	0.001	<0.001	0.02
Non-recurring cases ($n = 7$)						
GTV	44.0 ± 37.9	80.2 ± 74.2	84.6 ± 73.1	0.10	0.06	0.15
CTV	309 ± 169	375 ± 193	383 ± 195	0.04	0.015	0.08
PTV	444 ± 220	521 ± 245	532 ± 248	0.03	0.011	0.09
All cases ($n = 19$)						
GTV	30.8 ± 26.0	58.6 ± 52.4	63.5 ± 51.0	0.003	<0.001	0.009
CTV	249 ± 123	306 ± 146	312 ± 148	<0.001	<0.001	0.006
PTV	369 ± 159	437 ± 183	445 ± 185	<0.001	<0.001	0.004

Abbreviations: CTV = clinical target volume; GTV = gross tumour volume; MRI = magnetic resonance imaging; PET = positron emission tomography; PTV = planning target volume.

($p = 0.003$). The mean consensus PET CTV volume was 306 ± 146 cm^3 and the mean consensus MRI CTV volume was 249 ± 123 cm^3 ($p < 0.001$). The mean consensus PET PTV volume was 437 ± 183 cm^3 and the mean consensus MRI PTV volume was 369 ± 159 cm^3 ($p < 0.001$). This is consistent with linear regression of the consensus PET and MRI target volumes, as shown in Figure 2.5. In addition, the consensus MRI CTV margin did not encompass the consensus PET GTV in two cases (11%). In these cases, 1.6 and 2.9 cm^3 of the PET GTV extended outside the MRI CTV.

Uptake of ^{18}F-FDOPA was identified outside the edema volume apparent on T2 FLAIR images in 14/16 cases (88%). In addition, the apparent edema from T2 FLAIR images did not detect the ^{18}F-FDOPA uptake outside the MRI CTV for the case where the PET GTV extended outside the MRI CTV by 2.9 cm^3.

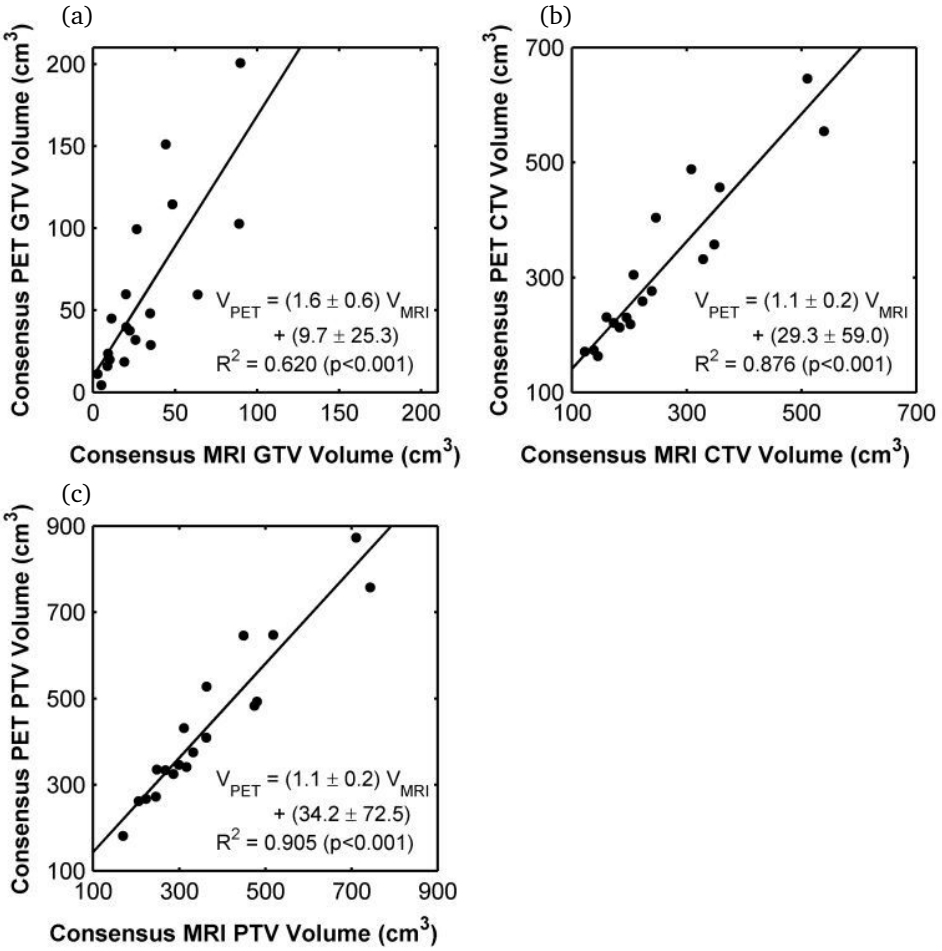

Figure 2.5. Linear regressions of the volumes of the consensus positron emission tomography (PET) and magnetic resonance imaging (MRI) (a) gross tumour volume (GTV), (b) clinical target volume (CTV), and (c) planning target volume (PTV). Uncertainties shown for the slope and intercept are 95% confidence intervals.

Consensus recurrence volumes were analyzed for 12 patients. Eleven (92%) recurrences were central. Glioblastomas accounted for seven (64%) central recurrences and anaplastic tumours accounted for four (36%) central recurrences. The mean volume of the central recurrences was 36.2 ± 37.1 cm^3. The interobserver volume overlap was $55\% \pm 19\%$. Examples of central recurrences are shown in Figures 2.6 and 2.7. Central recurrences extended outside the consensus MRI GTV in all cases and extended outside the consensus PET GTV in 10 cases (91%). Table 2.3 shows the number of central recurrences by tumour grade that extended outside margins of 0 cm, 1.5 cm, 2 cm, and 2.5 cm on the consensus MRI and PET GTV. The GTV plus 2-cm margin is equivalent to the CTV contour. Two (18%) central recurrences extended outside a 2-cm margin on the MRI GTV, one (9%) central recurrence extended outside a 2-cm margin on the PET GTV and the percentage of the recurrence volume that extended beyond the PET GTV ($52\% \pm 28\%$) was significantly less than the percentage that extended beyond the MRI GTV ($62\% \pm 20\%$, $p = 0.04$). One (8%) recurrence was outside (Figure 2.8), an anaplastic oligodendroglioma with a volume of 2.6 cm^3 and interobserver volume overlap of 47%.

2.4 Discussion

This study illustrates use of the STAPLE method to assess interobserver variability and calculate consensus contours. The interobserver contour variability of MRI-based contours in this study is similar to results previously reported in the literature. The mean STAPLE sensitivity reported previously for four high-grade astrocytoma cases was 0.914 (range, 0.753–0.981) and STAPLE specificity was 0.999 for all cases (80). In a retrospective study of seven patients with glioblastoma or anaplastic oligodendroglioma (88), the interobserver volume overlap

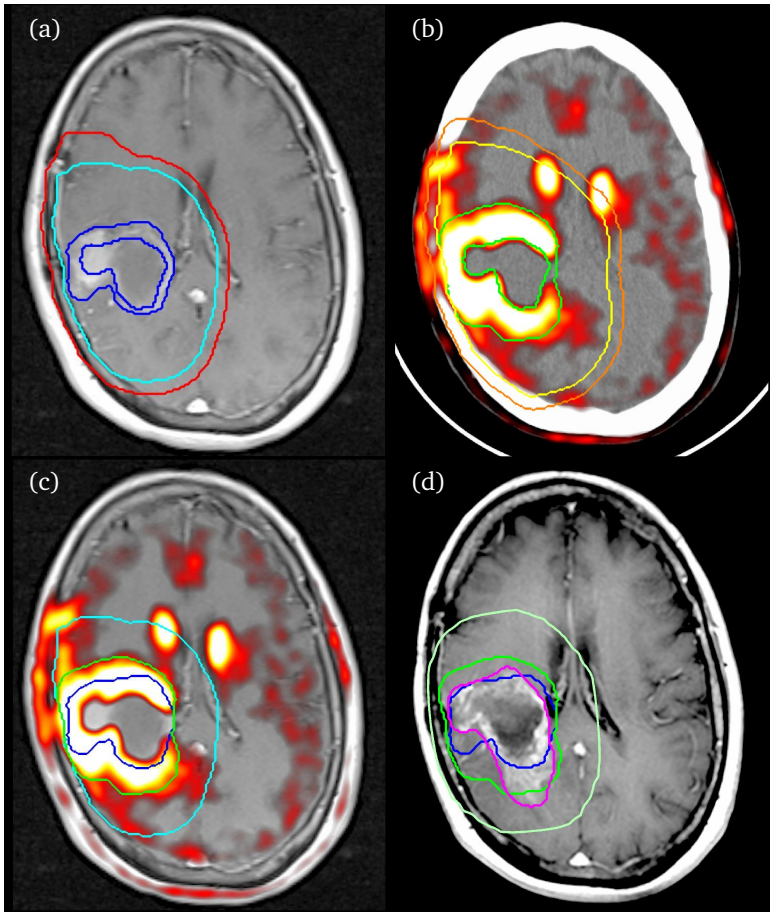

Figure 2.6. The (a) magnetic resonance imaging (MRI), (b) positron emission tomography (PET)/computed tomography, (c) fused MRI and PET, and (d) MRI at time of recurrence are shown to compare the MRI and MRI-PET target volumes for a case with a central recurrence. Contours shown: consensus MRI gross tumour volume (GTV) (blue), MRI clinical target volume (CTV) (cyan), MRI planning target volume (PTV) (red), MRI-PET GTV (green) MRI-PET CTV (yellow), MRI-PET PTV (orange), and recurrence (magenta), and the 95% isodose curve (light green).

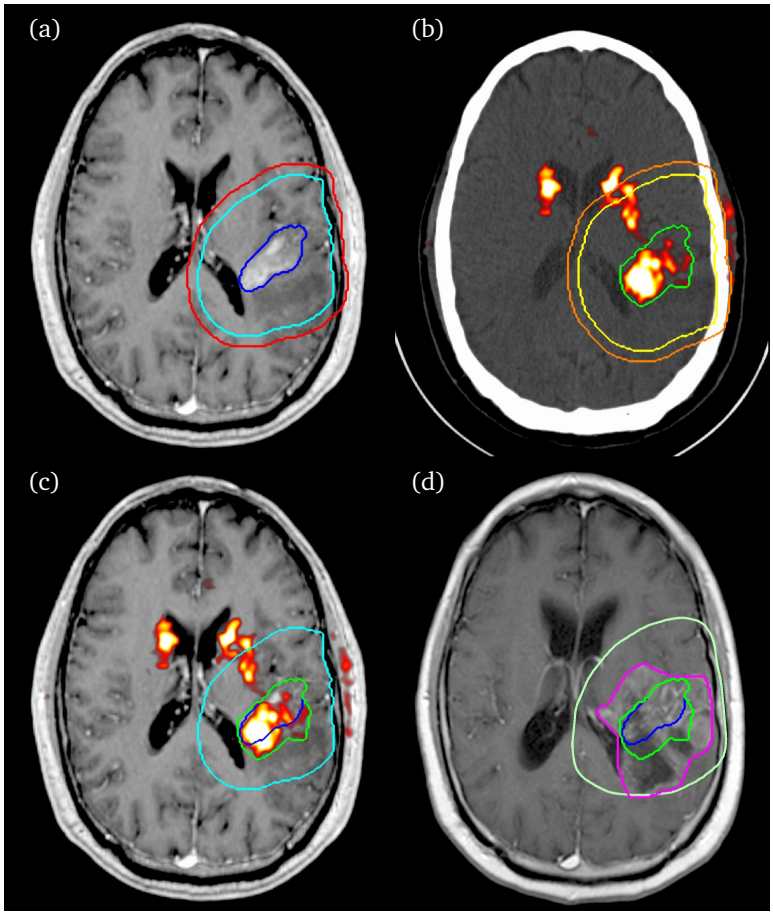

Figure 2.7. The (a) magnetic resonance imaging (MRI), (b) positron emission tomography (PET)/computed tomography, (c) fused MRI and PET, and (d) MRI at time of recurrence are shown to compare the MRI and MRI-PET target volumes for a second case with a central recurrence. Contours shown are the same as in Figure 2.6.

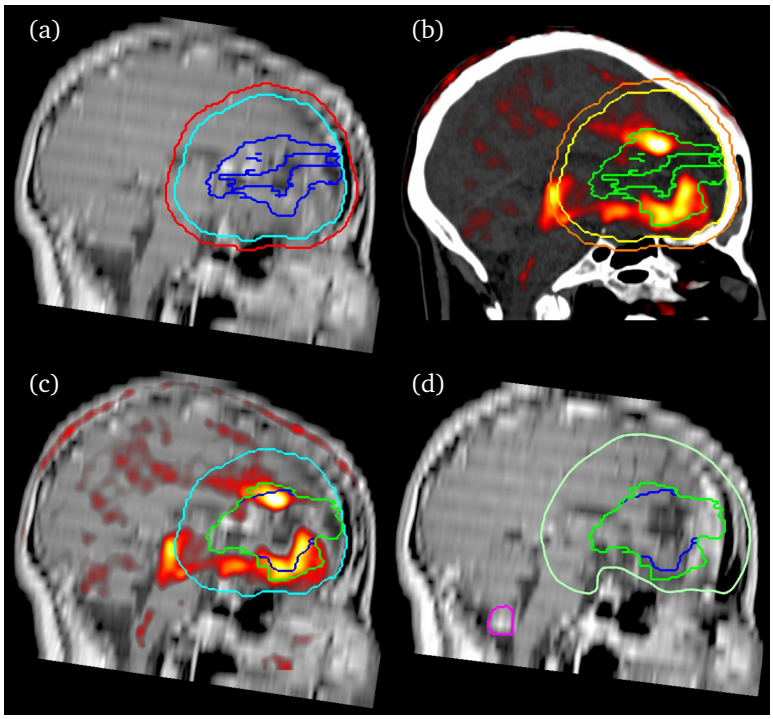

Figure 2.8. The (a) magnetic resonance imaging (MRI), (b) positron emission tomography (PET)/computed tomography, (c) fused MRI and PET, and (d) MRI at time of recurrence are shown to compare the MRI and MRI-PET target volumes for a case with an outside recurrence. Contours shown are the same as in Figure 2.6.

of delineations from five observers using CT and MRI registered with surface matching was on average 47% (range, 21%–72%).

In this study, interobserver variability of ^{18}F-FDOPA PET-based target volumes was not significantly different than variability of MRI-based target volumes. Interobserver volume overlap and STAPLE sensitivity values for CTVs and PTVs were larger than the values of GTVs. Since the CTV and PTV were isotropic expansions of the GTV, any interobserver variation appeared small relative to the large CTV and PTV volumes since volume overlap, sensitivity, and specificity are relatively insensitive to interobserver contour differences when these differences have a small impact on the total volume (81). Diffusion tensor

Table 2.3. Number of central recurrences, by tumour grade, that are outside consensus MRI, PET, and MRI-PET GTV structures.

Structure	MRI	PET	MRI-PET
Grade III tumours ($n = 4$)			
GTV	4 (100%)	3 (75%)	3 (75%)
GTV + 1.5 cm	1 (25%)	2 (50%)	1 (25%)
GTV + 2 cm (CTV)	1 (25%)	0 (0%)	0 (0%)
GTV + 2.5 cm	0 (0%)	0 (0%)	0 (0%)
Grade IV tumours ($n = 7$)			
GTV	7 (100%)	7 (100%)	7 (100%)
GTV + 1.5 cm	2 (29%)	3 (43%)	1 (14%)
GTV + 2 cm (CTV)	1 (14%)	1 (14%)	1 (14%)
GTV + 2.5 cm	1 (14%)	1 (14%)	1 (14%)
All recurrences ($n = 11$)			
GTV	11 (100%)	10 (91%)	10 (91%)
GTV + 1.5 cm	3 (27%)	5 (45%)	2 (18%)
GTV + 2 cm (CTV)	2 (18%)	1 (9%)	1 (9%)
GTV + 2.5 cm	1 (9%)	1 (9%)	1 (9%)

Abbreviations: CTV = clinical target volume; GTV = gross tumour volume; MRI = magnetic resonance imaging; PET = positron emission tomography.

imaging (DTI) may also be used to define anisotropic, patient-specific GTV-to-CTV margins (89, 90). In this case, there may be more interobserver variability of the CTV and PTV contours than that presented in Figure 2.4 and the relative difference between MRI and PET volumes for the CTV and PTV may be larger than that presented in 2.5(b) and (c).

Consensus PET target volumes were significantly larger than consensus MRI target volumes. The standard 2-cm margin from consensus MRI GTV-to-CTV definition led to geographic miss of the consensus PET GTV in 11% (2/19) of cases. Recurrence imaging was available for two of these cases and showed that recurrence volumes were within the 95% isodose surface and contained by a 2-cm margin on the MRI GTV in both cases. Even when reviewed retrospectively, the ^{18}F-FDOPA PET image set did not detect the one case of an outside

recurrence with a drop metastasis. Overall, it is unclear if treatment planning using the PET GTV would yield better treatment outcomes since all but one recurrence extended beyond the PET GTV and most were contained by a 2-cm margin on the MRI GTV. Despite the small number of cases, the proportion of recurrences of grade III and IV tumours that were contained by a 2-cm margin on the MRI GTV and PET GTV were similar (Table 2.3). It is important to note that any potential differences in treatment outcome could be a result of either target delineation or treatment technique. However, ^{18}F-FDOPA PET may detect glioma that is not detectable on MRI. Ledezma et al. (41) reported a case where ^{18}F-FDOPA PET uptake was in a region with a small amount of contrast enhancement on MRI, which could have been attributable to a residual tumour or postsurgical changes, was the site of recurrence three months afterward. There is a potential role of ^{18}F-FDOPA PET to include all areas of tumour while leading to a reduction of the GTV-to-CTV margin. This could reduce the potential for long-term neurocognitive toxicity of large irradiated brain volumes.

Amino acid radiotracers, such as ^{11}C-MET, ^{18}F-FET, and ^{18}F-FDOPA, have been comparatively studied and produce very similar quality images for brain tumours (91), except that there is normal, physiological uptake of ^{18}F-FDOPA in the basal ganglia. ^{11}C-MET and ^{18}F-FET do not accumulate in normal anatomic structures of the brain. Other studies have reported the use of ^{11}C-MET and ^{18}F-FET in similar settings to this study. In a prospective study of the treatment of primary glioblastomas, poor coverage of ^{11}C-MET uptake (which was not used for target volume delineation) was associated with an increased risk of noncentral recurrence (92). However, a prospective study of patients treated using ^{18}F-FET PET target volumes showed the observed pattern of failure to be predominantly central (93).

Biologically-based treatment planning with ^{18}F-FDOPA PET may also be possible since there is a correlation between ^{18}F-FDOPA uptake, cell density, and cell proliferation in newly diagnosed tumours (94). Uptake of ^{18}F-FET has been used to delineate radiation boost volumes. In a phase II trial of dose escalation for glioblastomas, a simultaneous integrated boost of 72 Gy in 30 fractions delivered to a ^{18}F-FET PET-defined PTV, concurrent with 60 Gy in 30 fractions delivered to a traditional MRI-defined PTV, did not lead to a survival benefit (95). ^{18}F-FDOPA uptake can potentially be used for dose painting by numbers. The feasibility of dose painting by numbers for proton treatments has been investigated using ^{18}F-FET PET (96). It is unknown if these techniques will lead to improved outcomes. Further research is warranted to determine if biologically-based treatment planning with ^{18}F-FDOPA PET/CT can improve outcomes for high-grade gliomas. However, it is important to note that twelve patients in this study had a recurrence in about five months, which stresses the need for better local control.

This study was limited in several respects, first of all, by the relatively small sample size ($n = 19$), with only 63% (12/19) having recurrence imaging available. For a larger sample of patients, the location of recurrent disease could be compared to consensus MRI and PET GTVs and this large dataset could be used to derive more accurate GTV-to-CTV margins and also compare resulting normal tissue involvement in the high dose region.

In addition, the intense uptake of ^{18}F-FDOPA in the normal basal ganglia may have made delineation of tumour using ^{18}F-FDOPA uptake more difficult for tumours located adjacent to these structures, possibly adding uncertainty to the study contours. Another difficulty with using ^{18}F-FDOPA PET is that post-surgical changes around the resection cavity can exhibit tracer uptake because of high levels of amino acid transport by activated macrophages or ^{18}F-FDOPA

leakage due to disruption of the blood-brain barrier (97). However, the study anticipated these challenges and the neuro-oncologists were advised on how to contour near the basal ganglia and how to omit regions of inflamed brain from the PET GTVs. It is not known how successful the observers were in following these instructions, because there was no gold standard available to define the glioma volumes. The true location of postoperative gliomas was unknown and the STAPLE consensus contours obtained from MRI and ^{18}F-FDOPA PET presented in this study were estimates of the true location of gliomas based on consensus contours by expert observers.

Chapter 3

Interhemispheric Differences from Diffusion Tensor Imaging

3.1 Introduction

T1-weighted magnetic resonance imaging (MRI) with contrast enhancement does not accurately represent the extent of the tumour for radiation therapy planning (26, 27). The addition of postoperative diffusion tensor imaging (DTI) to conventional MRI to treatment planning may potentially help improve localization of high-grade gliomas and therefore improve treatment outcome since anisotropic infiltration of glioma cells has been attributed in part to proliferation directed along structures in the brain, such as white matter tracks (98–103).

Diffusion, the random motion of molecules due to their thermal energy, can be accurately characterized by MRI. DTI is used to map and characterize the three-dimensional distribution of anisotropic diffusion of water in the brain. Its has been widely investigated for several pathologies, such as ischemia, myelination, axonal damage, inflammation, and edema (42). DTI measures often reported are the mean diffusivity (MD) and the fractional anisotropy (FA). MD, often referred to as the apparent diffusion coefficient (ADC), reflects the magnitude of diffusion (i.e., how far water molecules diffuse during measurement).

FA is a rotationally-invariant measure of the degree to which diffusivities are a function of the diffusion-weighting encoding direction (42, 46).

The role of DTI for the localization of radiation therapy target volumes for high-grade gliomas continues to be actively studied. Recent studies have shown that DTI may indicate glioma cell infiltration that is not visible on conventional MRI with gadolinium contrast enhancement (104, 105). In addition, DTI has been used to define anisotropic, patient-specific gross tumour volume (GTV)-to-clinical target volume (CTV) margins (89, 90). There is also potential that DTI may be used to identify regions within the target volume which may benefit from radiation dose boosts, such as regions of greater cell density and increased cell proliferation. FA has been suggested as a predictor of glioma cell density and proliferation activity (106–109).

FA and MD images can be difficult to interpret for the purpose of radiation therapy planning. Although edema is apparent on MD images (42), FA values around the tumour bed are smaller than in contralateral normal white matter (106). A potential method to improve interpretation of FA and MD images is by the calculation of interhemispheric difference images. In the method proposed by Aubert-Broche et al. (110), interhemispherical difference images were used to identify regions of functional interhemispheric asymmetries from brain ^{99m}Tc-exametazime and ^{99m}Tc-ethyl cysteinate dimer single photon emission computed tomography (SPECT) images of the brain using anatomical information from MRI. In their method, each MRI voxel was matched to its anatomically homologous voxel on the contralateral side. By mapping these voxels to the SPECT image, it was possible to compute SPECT interhemispheric difference images.

Therefore, the purpose of this study was to determine if FA or MD images obtained from postoperative DTI can be used to improve radiation therapy target

localization of gliomas. This was done by first characterizing the distribution of FA and MD in the GTV obtained from conventional T1-weighted and T2-weighted images. In addition, the distribution of FA and MD was characterized in regions of interest (ROIs) that were shells 0–5 mm, 5–10 mm, 10–15 mm, 15–20 mm, and 20–25 mm regions outside the GTV, and were then compared with values in contralateral normal brain. In addition, a method was implemented to automatically calculate FA and MD interhemispheric difference images for potential use in radiation therapy planning.

3.2 Methods and Materials

3.2.1 Patient Selection

Seven patients with histologically-confirmed, newly diagnosed glioma underwent radiation therapy planning with postoperative MRI and computed tomography (CT). Excision of the tumour was performed with MRI and 3,4-dihydroxy-6-[^{18}F]fluoro-L-phenylalanine (^{18}F-FDOPA) positron emission tomography (PET) neuronavigation. Institutional research ethics board approval was obtained for all image protocols and all subjects provided written informed consent. Eligible patients were at least 18 years of age, had a contrast-enhancing mass on diagnostic brain CT or MRI that strongly suggested a diagnosis of World Health Organization (WHO) grade III or IV glioma prior to surgery, had a Karnofsky Performance Status of 70 or greater, and had a glomerular filtration rate of 60 mL/min or greater. Exclusion criteria were indication for urgent craniotomy to relieve mass effect, T1 enhancement or T2 signal that involved the basal ganglia, previous intracranial malignancy or any invasive malignancy unless free of disease at least five years, prior cranial irradiation, were taking

Table 3.1. Patient characteristics.

No. of Patients	7
Sex	
Female	2 (29%)
Male	5 (71%)
Age, median (range)	51 (34–80) years
Histology	
Oligoastrocytoma (grade II)	1 (14%)
Anaplastic astrocytoma (grade III)	1 (14%)
Glioblastoma (grade IV)	5 (71%)
Time, median (range)	
Surgery to MRI	6 (2–27) days

Abbreviation: MRI = magnetic resonance imaging.

medication for the treatment of Parkinson's disease (e.g., levodopa), or allergies or contraindications to contrast MRI or radiation therapy. Patient and tumour characteristics, as well as the timing between surgery and postoperative MRI, are shown in Table 3.1.

3.2.2 Treatment Planning Imaging

MRI was obtained using a 1.5-T Siemens Magnetom Symphony Tim system (Siemens Healthcare, Erlangen, Germany). T1-weighted images with gadolinium contrast enhancement were obtained with the turbo spin echo (TSE) sequence (echo time (TE) = 14 ms, pixel resolution = 1 mm, slice thickness = 3 mm) and T2-weighted fluid attenuated inversion recovery (FLAIR) images were obtained (TE = 97 ms, pixel resolution = 0.5 mm, slice thickness = 3 mm).

3.2.3 Diffusion Tensor Imaging

DTI was obtained using single-shot echo planar imaging for 20 noncolinear directions with $b = 1000$ s/mm^2 and one additional image with $b = 0$ (TE = 98

ms, repetition time (TR) = 3800 ms, 128×128 acquisition matrix, pixel resolution = 1.95 mm, slice thickness = 5 mm, slice spacing = 1 mm). Diffusion imaging was repeated four times for signal averaging.

Images were processed using the Oxford Centre for Functional MRI of the Brain Software Library (FSL) (version 5.0; Oxford, UK) (111–113). The brain extraction tool was used to obtain a brain mask of the T1-weighted image (114). DTI data was corrected for eddy current distortions and then FA (Eq. 1.29) and MD (Eq. 1.28) images were obtained from diffusion tensor fitting (115–119).

The following ROIs were delineated: the GTV delineated by the patient's attending radiation oncologist on T1-weighted and T2-weighted images excluding the surgical cavity, and regions 0–5 mm, 5–10 mm, 10–15 mm, 15–20 mm, and 20–25 mm outside the GTV. ROIs were cropped to ensure that they were within the brain mask. All images were linearly registered using a 12-parameter affine model with mutual information cost function (120, 121). Figure 3.1 shows an example of the registered T1-weighted, T2-weighted, FA, and MD images for a sample patient. ROI contours for this case are shown in Figure 3.2.

In order to calculate a normal brain ROI and interhemispheric difference images (discussed below in Section 3.2.4), all images and ROIs were then aligned to the Montreal Neurological Institute (MNI) 152 standard-space T1-weighted average structure template image (122) using the FSL nonlinear registration tool (123, 124). It used a b-spline representation of the registration warp field (125). A normal brain ROI was defined as the mirror image of the GTV in the left-right direction in the standard space. An example of these images aligned to the standard space are shown in Figure 3.3. ROI contours in the standard space are shown in Figure 3.4.

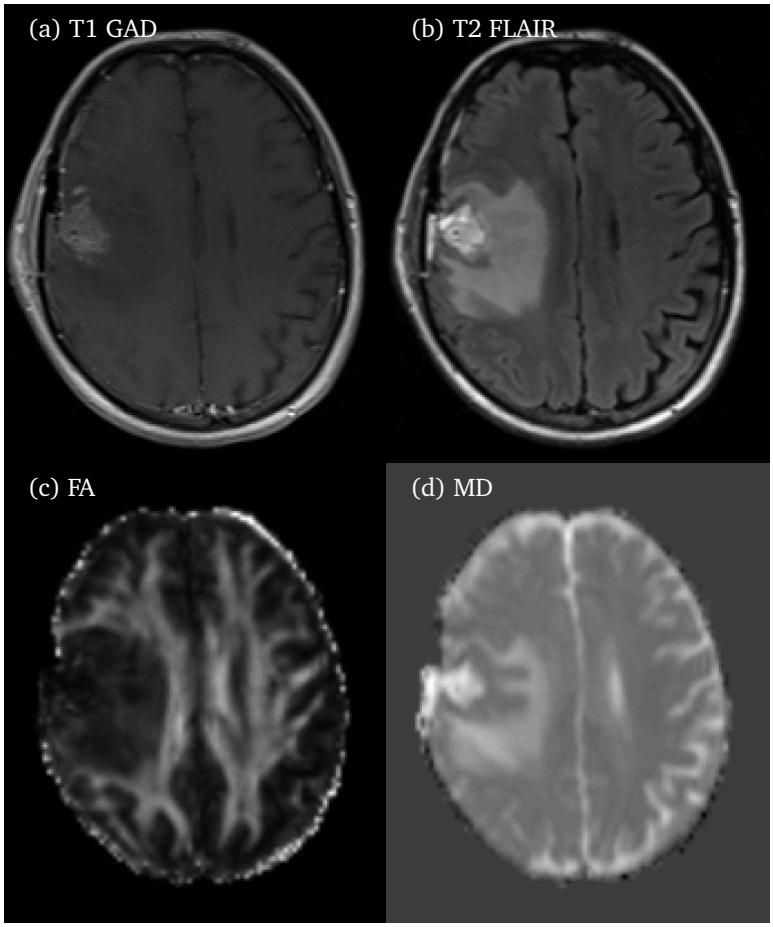

Figure 3.1. An example of (a) T1-weighted magnetic resonance imaging (MRI) with gadolinium contrast enhancement and (b) T2-weighted fluid attenuated inversion recovery MRI, and the (c) fractional anisotropy (FA) and (d) mean diffusivity (MD) images obtained from diffusion tensor imaging for a sample patient.

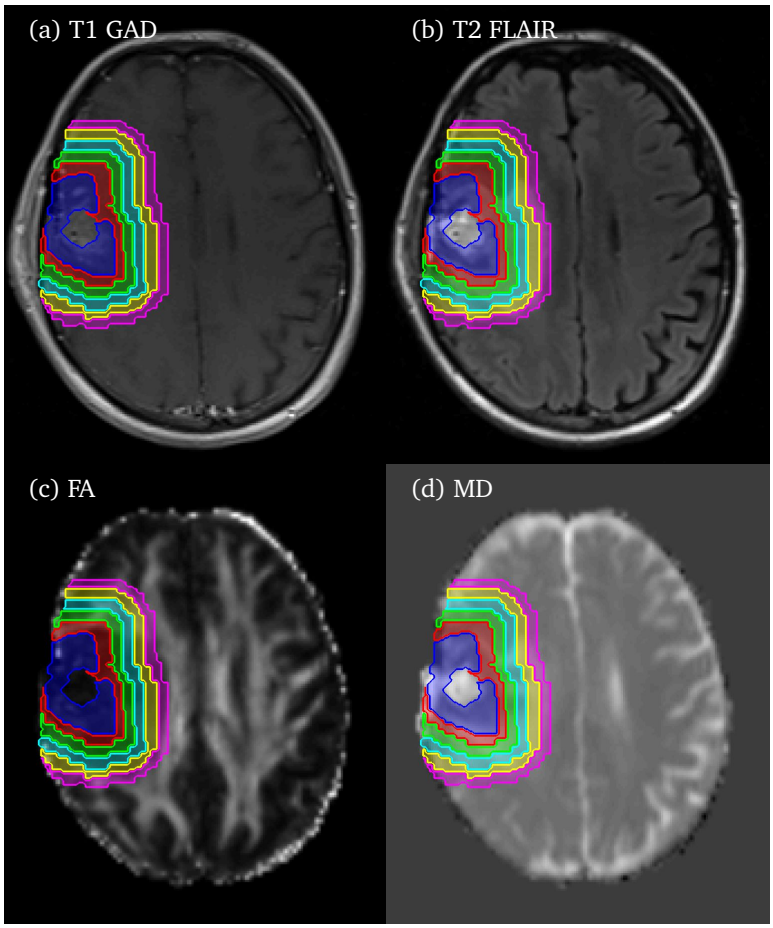

Figure 3.2. Region of interest contours are shown on (a) T1-weighted magnetic resonance imaging (MRI) with gadolinium contrast enhancement and (b) T2-weighted fluid attenuated inversion recovery MRI, and the (c) fractional anisotropy (FA) and (d) mean diffusivity (MD) images obtained from diffusion tensor imaging for a sample patient. Contours shown are the gross tumour volume (GTV) (blue), and regions regions 0–5 mm (red), 5–10 mm (green), 10–15 mm (cyan), 15–20 mm (yellow), and 20–25 mm (magenta) outside the GTV.

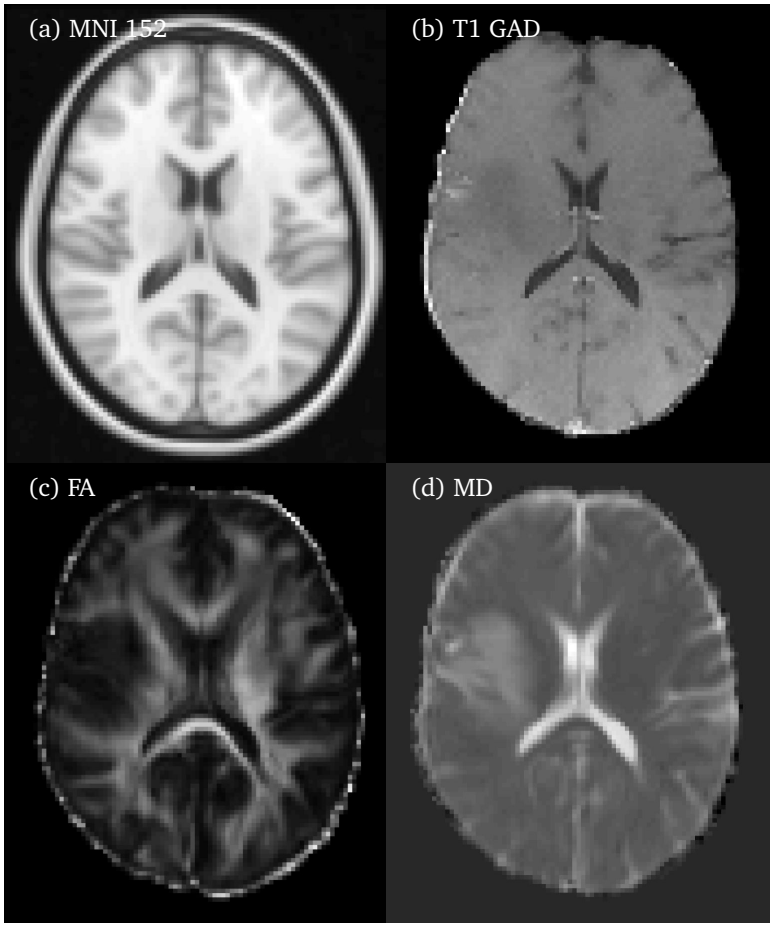

Figure 3.3. An example of the (a) Montreal Neurological Institute (MNI) 152 standard space T1-weighted average structure template image and the (b) T1-weighted with gadolinium contrast enhancement, (c) fractional anisotropy (FA), and (d) mean diffusivity (MD) images registered to this standard space for a sample patient.

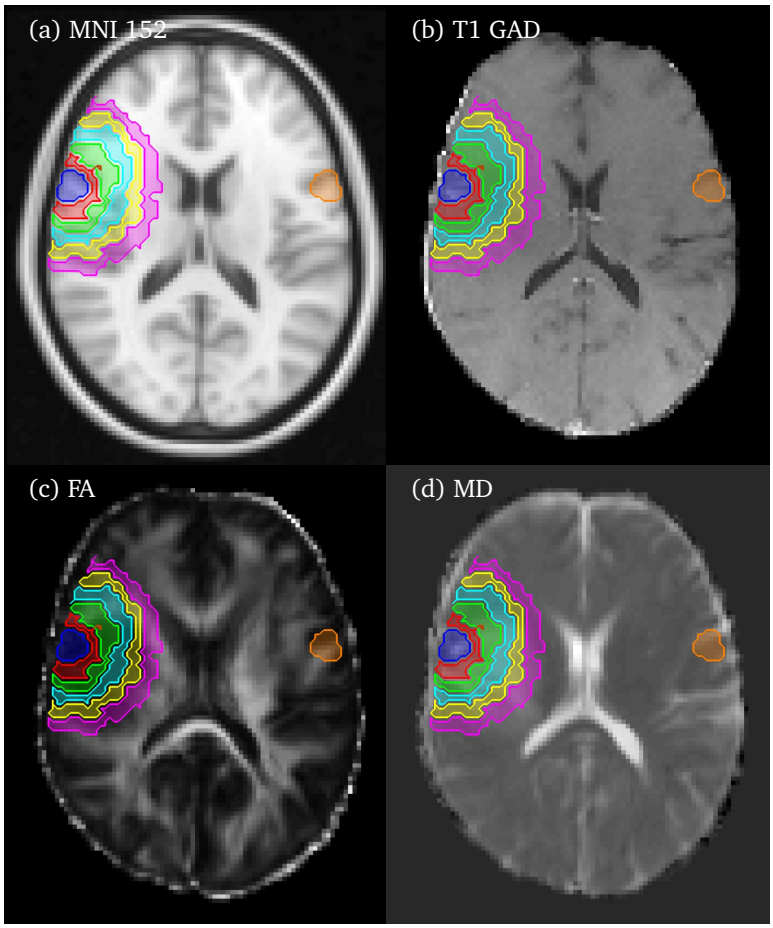

Figure 3.4. Region of interest contours on the (a) Montreal Neurological Institute (MNI) 152 standard space T1-weighted average structure template image, (b) T1-weighted with gadolinium contrast enhancement, (c) fractional anisotropy (FA), and (d) mean diffusivity (MD) images registered to this standard space for a sample patient. Contours shown are the gross tumour volume (GTV) (blue), and regions regions 0–5 mm (red), 5–10 mm (light green), 10–15 mm(cyan), 15–20 mm (yellow), and 20–25 mm (magenta) outside the GTV, and normal brain (orange).

The distribution of FA and MD values inside the ROIs (GTV, 0–5 mm, 5–10 mm, 10–15 mm, 15–20 mm, and 20–25 mm outside the GTV, and normal brain) were obtained using the images aligned in the standard space with MATLAB (version 7.0.0.19920; The MathWorks, Inc., Natick, MA). Differences between the mean FA and MD in normal brain and the mean FA and MD in the GTV, and 0–5 mm, 5–10 mm, 10–15 mm, 15–20 mm, and 20–25 mm regions outside the GTV were tested for statistical significance using two-sided paired t-tests ($\alpha = 0.05$).

In addition, the mean FA in the GTV, regions 0–5 mm, 5–10 mm, 10–15 mm, 15–20 mm, and 20–25 mm outside the GTV, and normal brain ROI were calculated using a standard FA atlas: the FMRIB58_FA standard space image available in FSL (126). This image is a high-resolution average of 58 well-aligned good quality FA images for healthy male and female subjects (aged, 20–60 years). The original DTI resolution for these images was $2 \times 2 \times 2$ mm. The mean FA obtained from the FMRIB58_FA image was then compared with the measured mean FA using two-sided paired t-tests ($\alpha = 0.05$).

3.2.4 Interhemispheric Difference Images

Using the FA and MD standard space images, interhemispheric difference images for FA (ΔFA) and MD (ΔMD) were calculated using the equations:

$$\Delta\mathrm{FA}(x,y,z) = \overline{\mathrm{FA}}(x,y,z) - \overline{\mathrm{FA}}(-x,y,z), \tag{3.1a}$$

$$\Delta\mathrm{MD}(x,y,z) = \overline{\mathrm{MD}}(x,y,z) - \overline{\mathrm{MD}}(-x,y,z). \tag{3.1b}$$

where $\overline{\mathrm{FA}}(x,y,z)$ and $\overline{\mathrm{MD}}(x,y,z)$ were the mean FA and MD images obtained using a mean filter with a sphere centered at voxel (x,y,z) in the standard

space. Interhemispheric difference images were calculated with spheres of diameter 0 mm, 10 mm, and 20 mm.

The distribution of FA and MD interhemispheric differences were characterized in the GTV and the regions 0–5 mm, 5–10 mm, 10–15 mm, 15–20 mm, and 20–25 mm outside the GTV. Mean interhemispheric differences were statistically compared using two-sided t-tests ($\alpha = 0.05$).

3.3 Results

Examples of the distribution of FA and MD in the GTV, regions 0–5 mm, 5–10 mm, 10–15 mm, 15–20 mm, and 20–25 mm outside the GTV, and normal brain ROIs are shown in Figure 3.5. The distribution of FA and MD suggested that FA values tended to increase and MD values tended to decrease as the distance outside the GTV increased. These values approached those of normal brain tissue. This is consistent with the expectation of a gradual and decreasing presence of tumour cells.

The mean FA and MD values in each ROI are shown in Figure 3.6. The mean FA in the GTV ($0.12 \pm 0.03; p = 0.004$) and in the regions 0–5 mm ($0.15 \pm 0.03; p = 0.02$), 5–10 mm ($0.17 \pm 0.03; p = 0.07$), 10–15 mm ($0.20 \pm 0.04; p = 0.8$), and 15–20 mm ($0.21 \pm 0.04; p = 0.2$) outside the GTV were smaller than the mean FA in normal brain tissue (0.20 ± 0.04). The mean FA in the region 20–25 mm ($0.24 \pm 0.05; p = 0.02$) outside the GTV was larger than the mean value in normal brain.

The mean FA obtained from the FMRIB58_FA standard space image in the GTV was 0.212 ± 0.006, which was significantly larger than mean measured FA in the GTV ($p = 0.001$). The FMRIB58_FA standard space image FA in the regions 0–5 mm, 5–10 mm, 10–15 mm, 15–20 mm, and 20–25 mm outside the

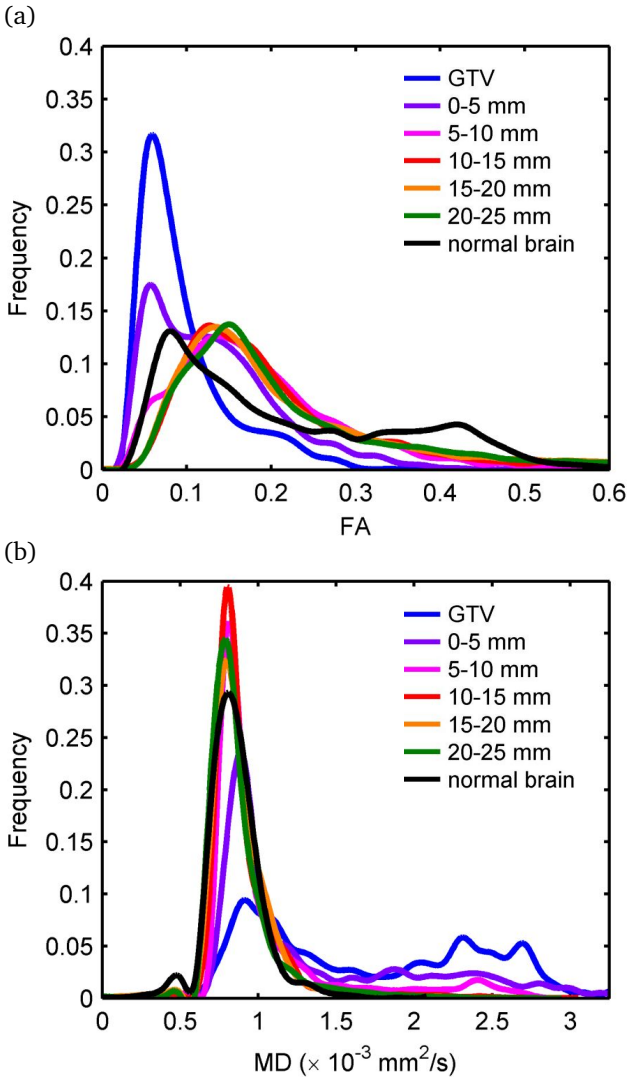

Figure 3.5. The distribution of fractional anisotropy (FA) and mean diffusivity (MD) values in the gross tumour volume (GTV), peritumoural regions of interest, and normal brain tissue for one patient.

GTV was 0.206 ± 0.006 ($p = 0.04$), 0.237 ± 0.006 ($p = 0.01$), 0.246 ± 0.006 ($p = 0.003$), 0.251 ± 0.006 ($p = 0.01$), and 0.261 ± 0.006 ($p = 0.033$). The normal brain mean FA in the FMRIB58_FA standard space image (0.205 ± 0.006) was not significantly different than the measured FA in that ROI ($p = 0.7$).

The mean MD ($\times 10^3$ mm^2/s) was significantly larger in the GTV (1.48 ± 0.19; $p = 0.01$) and regions 0–5 mm region (1.15 ± 0.26; $p = 0.10$) 5–10 mm (1.05 ± 0.11; $p = 0.10$), 0–15 mm (1.01 ± 0.10, $p = 0.01$), 15–20 mm (0.99 ± 0.10, $p = 0.009$), and 20–25 mm (0.96 ± 0.10; $p = 0.02$) outside the GTV than the mean MD in normal brain (0.93 ± 0.09).

Examples of FA and MD interhemispheric difference images that were obtained with a mean filter using a sphere of diameter 0 mm, 10 mm, and 20 mm are shown in Figures 3.7–3.9 for a sample patient. The distribution of FA and MD interhemispheric differences in Figures 3.10–3.12 a sample patient is shown for images that were obtained with a mean filter using a sphere of diameter 0 mm, 10 mm, and 20 mm. In general, the distribution of FA and MD interhemispheric differences followed the same trends as FA and MD values. This is consistent with the examples shown in Figures 3.7–3.9.

The mean and standard error of FA and MD interhemispheric differences are shown in Figure 3.13 for images that were spatially filtered with a mean filter using a sphere of diameter 0 mm, 10 mm, and 20 mm. The mean and standard error of FA and MD interhemispheric differences, along with p-values from two sided t-tests, for images that were spatially filtered with a mean filter using a sphere of diameter 0 mm, 10 mm, and 20 mm are shown in Table 3.2. The mean FA and MD interhemispheric differences values were significantly larger than zero in the GTV for all cases. However, most mean FA and MD interhemispheric difference values were not significantly larger than zero for the ROIs outside the GTV.

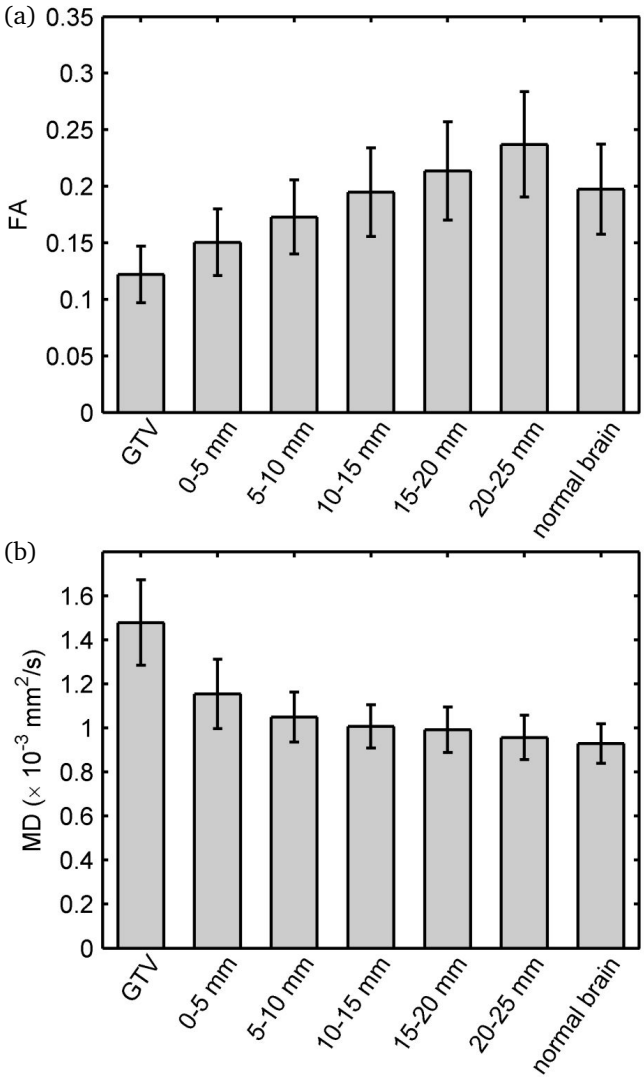

Figure 3.6. The patient-averaged (a) fractional anisotropy (FA) and (b) mean diffusivity (MD) values for tumour, peritumoural, and normal brain regions of interest. Error bars show the standard error.

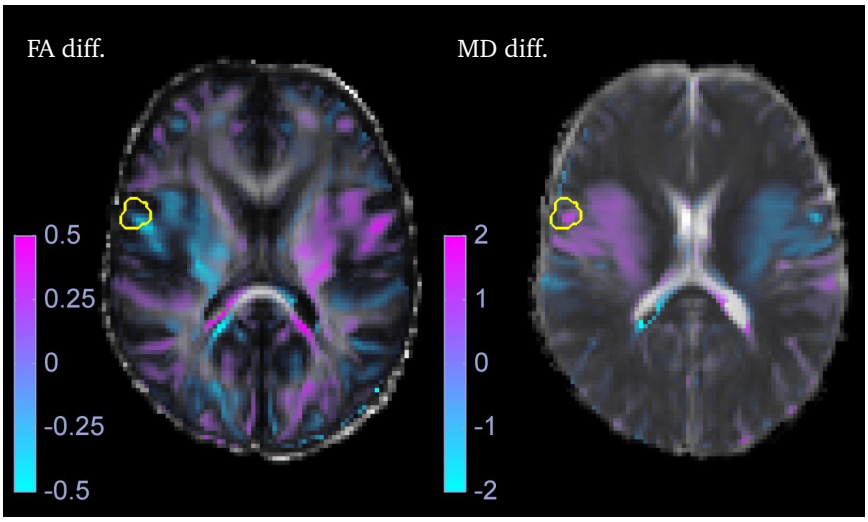

Figure 3.7. An example of the fractional anisotropy (FA) and mean diffusivity (MD) ($\times 10^{-3}$ mm^2/s) interhemispheric difference images for one patient obtained using unfiltered images. The gross tumour volume contour is shown in yellow.

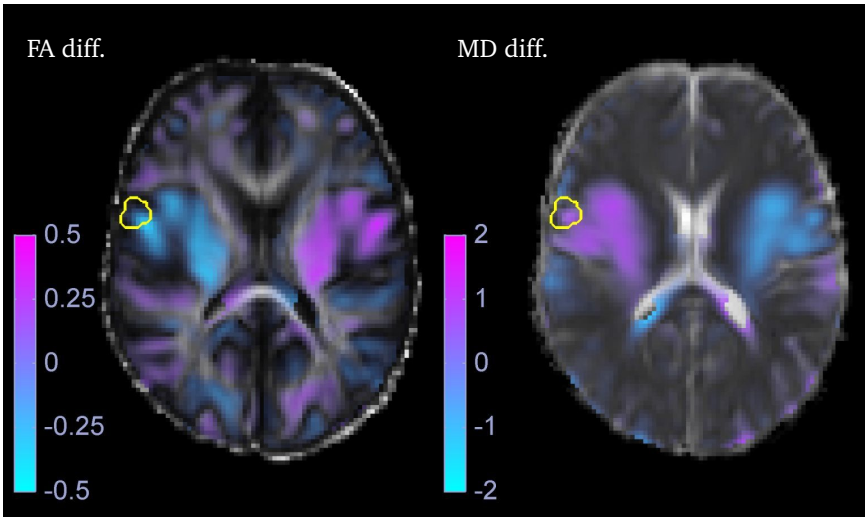

Figure 3.8. An example of the fractional anisotropy (FA) and mean diffusivity (MD) ($\times 10^{-3}$ mm^2/s) interhemispheric difference images for one patient obtained using images that were spatially filtered with a mean filter using a sphere of diameter 10 mm. The gross tumour volume contour is shown in yellow.

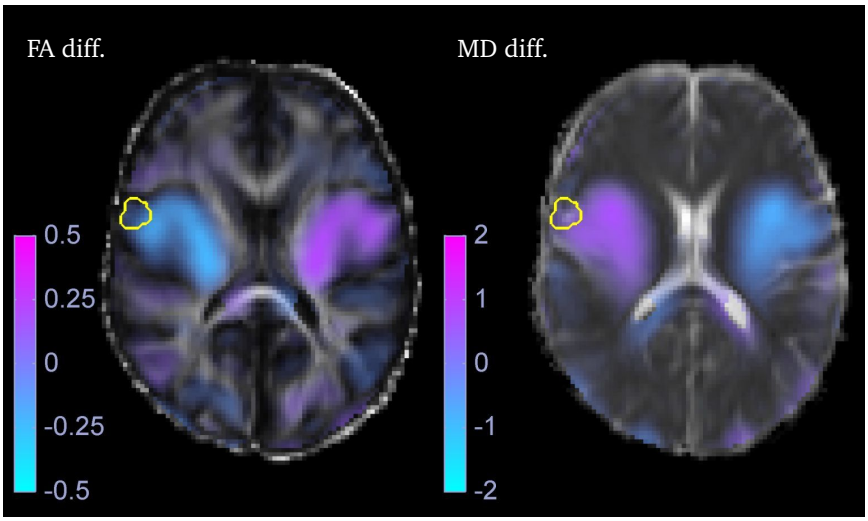

Figure 3.9. An example of the fractional anisotropy (FA) and mean diffusivity (MD) ($\times 10^{-3}$ mm^2/s) interhemispheric difference images for one patient obtained using images that were spatially filtered with a mean filter using a sphere of diameter 20 mm. The gross tumour volume contour is shown in yellow.

3.4 Discussion

This study is the first of its kind to characterize FA and MD values obtained from postoperative DTI of high-grade glioma following surgery guided by ^{18}F-FDOPA PET. The trend in DTI parameters is similar to those presented elsewhere. In a study of DTI of glioblastoma prior to CT-guided stereotactic biopsy, the mean values of the FA in the corpus collosum, subcortical white matter, and glioblastoma lesion were 0.70 ± 0.05, 0.32 ± 0.04, and 0.24 ± 0.05, with mean values significantly different among all three ROIs ($p < 0.05$) (106). In another study, fiber density mapping and magnetic resonance spectroscopy of 48 patients with grade II–IV glioma showed similar FA and MD values (127). For grade IV tumors, the FA values in the tumour, peritumoural region, and normal appearing white matter were 0.224 ± 0.043, 0.385 ± 0.043, and 0.469 ± 0.069, and MD values ($\times 10^{-3}$ mm^2/s) were 1.360 ± 0.164, 1.033 ± 0.107, and 0.822 ± 0.173.

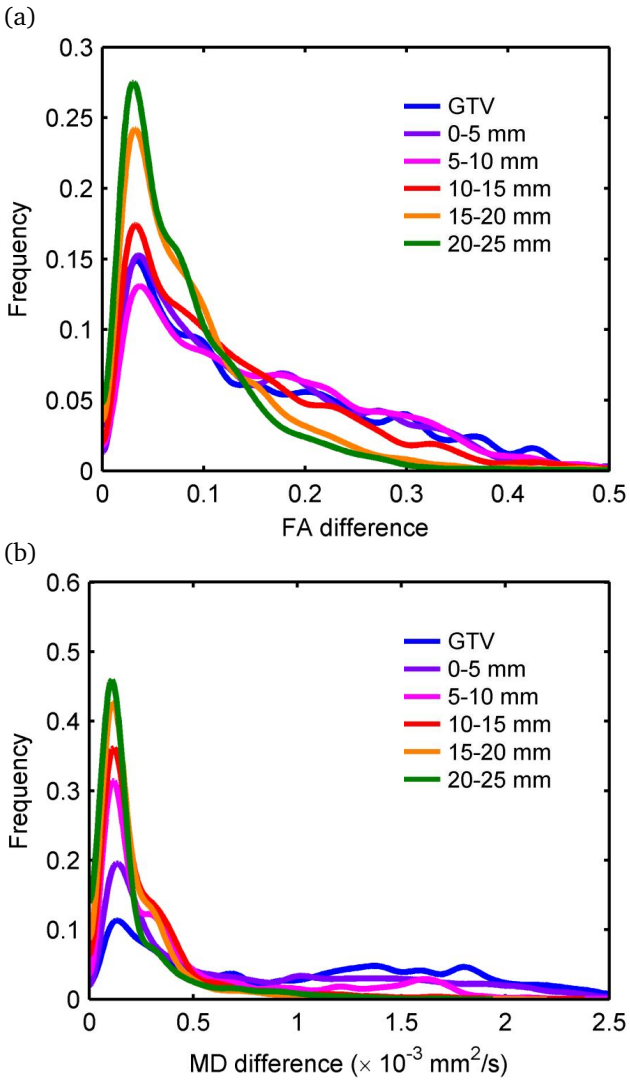

Figure 3.10. The distribution of (a) fractional anisotropy (FA) and (b) mean diffusivity (MD) interhemispheric differences in the gross tumour volume (GTV) and peritumoural regions of interest for one patient obtained using images spatially filtered using unfiltered images.

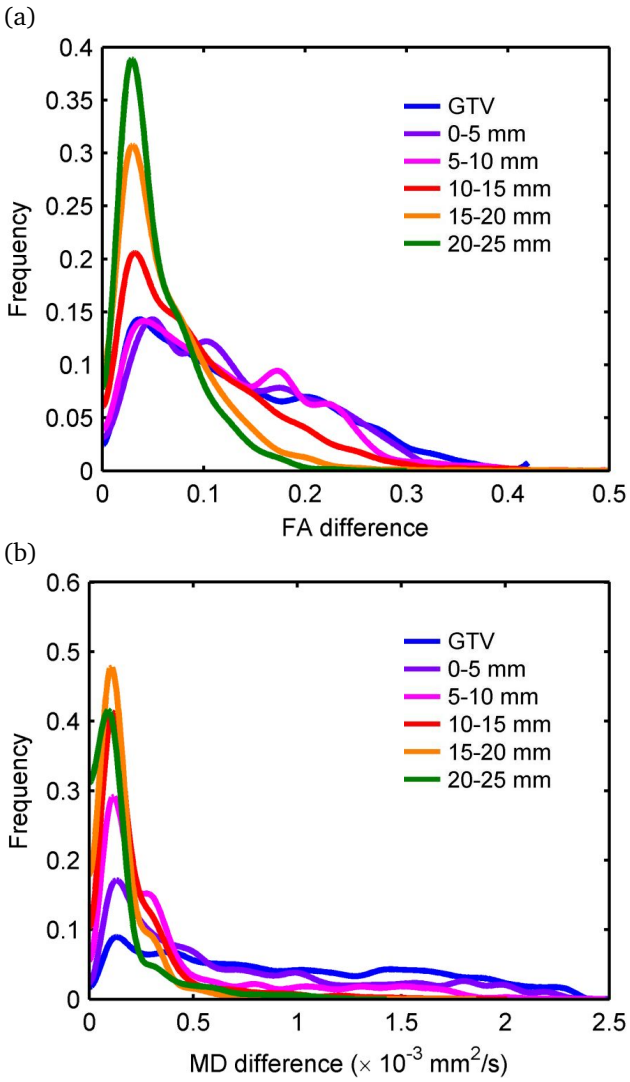

Figure 3.11. The distribution of fractional anisotropy (FA) and mean diffusivity (MD) interhemispheric differences in the gross tumour volume (GTV) and peritumoural regions of interest for one patient obtained using images spatially filtered using a mean filter with a sphere of diameter 10 mm.

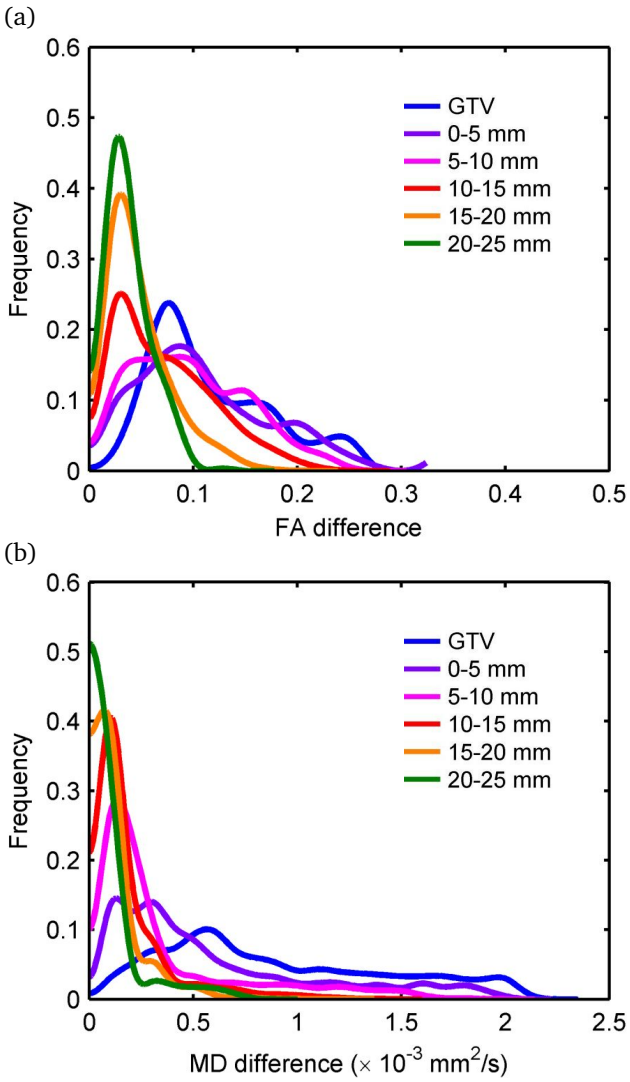

Figure 3.12. The distribution of fractional anisotropy (FA) and mean diffusivity (MD) interhemispheric differences in the gross tumour volume (GTV) and peritumoural regions of interest for one patient obtained using images spatially filtered using a mean filter with a sphere of diameter 20 mm.

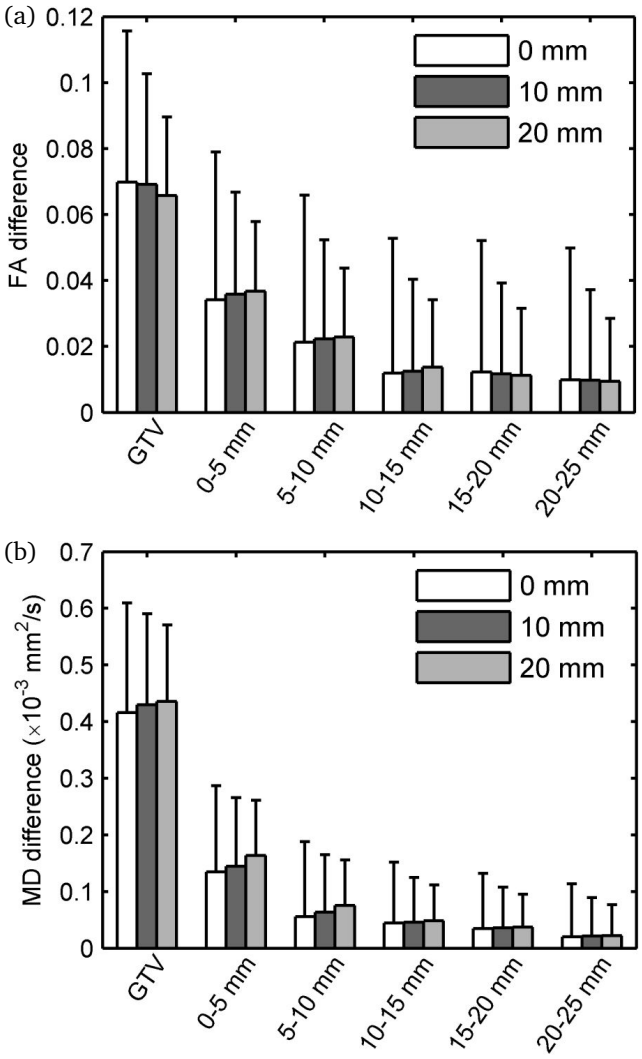

Figure 3.13. The patient-averaged (a) fractional anisotropy (FA) and (b) mean diffusivity (MD) interhemispheric difference for the gross tumour volume (GTV) and peritumoural regions of interest obtained using images that were spatially filtered with a mean filter using a sphere of diameter (a) 0 mm (white), 10 mm (dark gray) and 20 mm (light gray). Error bars show the standard error.

Table 3.2. Mean interhemispheric differences using images that were spatially filtered with a mean filter using spheres of diameter 0 mm, 10 mm, and 20 mm.

Structure	ΔFA		ΔMD ($\times 10^{-3}$ mm^2/s)	
	Mean ± SE	p	Mean ± SE	p
0-mm filter (unfiltered)				
GTV	0.073 ± 0.044	0.004	0.543 ± 0.219	0.011
0–5 mm	0.054 ± 0.044	0.04	0.203 ± 0.183	0.03
5–10 mm	0.050 ± 0.044	0.07	0.110 ± 0.142	0.11
10–15 mm	0.032 ± 0.042	0.05	0.089 ± 0.114	0.08
15–20 mm	0.026 ± 0.041	0.07	0.080 ± 0.104	0.12
20–25 mm	0.020 ± 0.042	0.07	0.050 ± 0.098	0.07
10-mm filter				
GTV	0.074 ± 0.031	0.004	0.550 ± 0.175	0.008
0–5 mm	0.055 ± 0.030	0.03	0.224 ± 0.147	0.02
5–10 mm	0.049 ± 0.030	0.06	0.116 ± 0.109	0.08
10–15 mm	0.033 ± 0.030	0.05	0.092 ± 0.085	0.08
15–20 mm	0.025 ± 0.030	0.06	0.079 ± 0.078	0.10
20–25 mm	0.019 ± 0.030	0.06	0.051 ± 0.073	0.06
20-mm filter				
GTV	0.073 ± 0.022	0.005	0.544 ± 0.141	0.006
0–5 mm	0.054 ± 0.021	0.02	0.256 ± 0.115	0.017
5–10 mm	0.047 ± 0.022	0.05	0.133 ± 0.088	0.04
10–15 mm	0.034 ± 0.023	0.05	0.096 ± 0.069	0.06
15–20 mm	0.025 ± 0.023	0.06	0.077 ± 0.065	0.09
20–25 mm	0.018 ± 0.021	0.05	0.051 ± 0.059	0.05

Abbreviations: FA = fractional anisotropy; GTV = gross tumour volumes; MD = mean diffusivity; SE = standard error.

However, in the present study the FA in the GTV and normal brain were lower: 0.12±0.03 and 0.20±0.04, respectively. This is due the fact that different ROI definitions were used in this study. In the aforementioned studies, the glioblastoma region of interest was placed at the enhancing central region of the tumour prior to surgery. The definition of the normal brain ROIs in this study included both white and gray matter. However, comparison of the FA values

with FA in the FMRIB58_FA standard space image showed that contralateral normal brain values were similar to those in healthy patients.

The interhemispheric difference images presented here provide guidance on how DTI images may be utilized for radiation therapy planning. Larger values of interhemispheric MD differences likely corresponded to edema. In addition, the area around the tumour with abnormal FA smaller than contralateral normal brain values were more easily visualized than with the original FA images. In Figure 3.6(a), the mean FA in the 20–25 mm region outside the GTV was significantly larger than the mean FA in the normal brain ROI. This is inconsistent with the trend of FA in the other peritumoural shells. This increase of FA in the 20–25 mm region occurred since this shell was more likely to include the corpus callosum. Interhemispheric differences in FA in this shell were not significantly different from zero (Figure 3.13(a)), consistent with the trend of interhemispheric FA differences in the other peritumoural shells.

However, for these images to be used to treatment planning, it is necessary to establish by some method, such as stereotactic biopsy or comparison with three-dimensional patterns of failure, that these difference values correlate with tumour cell density or proliferation. There is no clear physical mechanism that describes the expected FA and MD values for gliomas. In fact, there have been conflicting reports of the correlation of FA and MD values with tumour cell density and proliferation. Beppu et al. (106) and Kinoshita et al. (107) found that FA positively correlated and MD negatively correlated with the cell density in the tumour core, while Stadlbauer et al. (108) and Lee et al. (109) reported that FA negatively correlated and MD positively correlated. Moreover, a recent study of 15 patients with high-grade glioma found minimal anatomical overlap of the the minimum ADC value, a marker of tumour cellularity, obtained from diffusion weighted imaging (maximum b=3000 s/mm^2) and the maximum ^{18}F-FDOPA

PET standardized uptake value (SUV) ratio, a marker of tumour infiltration and proliferation (128).

In this study, isotropic margins were used to define the regions of interest 0–5 mm, 5–10 mm, 10–15 mm, 15–20 mm, and 20–25 mm. Since glioma infiltration is anisotropic (98–103), the use of anisotropic margins from the DTI (89, 90) could also be combined with the interhemispheric difference images presented here to improve radiation therapy target localization. In addition, fiber tractography may also be useful for glioma identification. For example, a study by Stadlbauer et al. (129) of the fiber density mapping of 20 patients with grade II and III glioma showed a strong negative correlation between fiber density and both the logarithm of tumour cell number and the percentage of tumour cell infiltration.

Despite the small sample size ($n = 7$), this study demonstrates that interhemispherical difference images obtained from DTI may potentially be useful for radiation therapy target volume localization of gliomas. As mentioned earlier, for these images to be used clinically it is necessary to establish if either FA and/or MD interhemispherical difference values correlate with tumour cell density or proliferation. In addition, any clinical interpretation of these images must take into account that this method is based on the nonlinear registration of the patient images with unhealthy tissue that is being mapped to a standardized image of a healthy patient.

Chapter 4

Biologically-Guided Volumetric Modulated Arc Therapy

4.1 Introduction

Intensity modulated radiation therapy (IMRT) and volumetric modulated arc therapy (VMAT) offer a dosimetric advantage to three-dimensional conformal radiation therapy (3D-CRT) in the radiation therapy planning of high-grade gliomas (9, 49, 54, 130–132), maintaining dose coverage to the planning target volume (PTV) while reducing dose to organs at risk (OARs). Clinical studies with IMRT have reported good patient outcomes (54, 133–138). Although radiation therapy of high-grade gliomas with concomitant chemotherapy improves patient survival (10), patterns of failure following radiation therapy are central (i.e., near the resection margin) (52, 92, 139–142).

Functional imaging can potentially be used in conjunction with computed tomography (CT) and conventional magnetic resonance imaging (MRI) to improve localization of malignant tissue. It can also be used to identify regions within the target volume, such as regions of greater tumour cell density, cell proliferation, or radioresistance, which may benefit from radiation dose escalation. The feasibility of such dose boosts has been reported. The Radiation Therapy Oncology Group (RTOG) 98-03 study reported that dose escalation to 84 Gy in

2-Gy fractions using 3D-CRT for newly diagnosed glioblastoma did not result in any dose-limiting central nervous system toxicities (143). Positron emission tomography (PET) images have been used to identify regions for dose escalation. In a study of the hypofractionated treatment of glioblastoma, a simultaneous integrated boost of a ^{11}C-methionine (^{11}C-MET)-defined gross tumour volume (GTV) to 68 Gy in eight fractions, delivered with helical tomotherapy, showed efficacy in controlling tumour cells without evidence of normal tissue toxicity (138).

In addition, the intensity modulation achievable with IMRT and VMAT can allow the planned dose distribution to the target to be optimized by dose painting, where the dose distribution is optimized to conform to the functional information obtained from imaging techniques (75, 76, 144). Dose escalation in this manner can be achieved by dose painting by contours or dose painting by numbers. Dose painting by contours refers to the use of functional images to identify subvolumes for radiation boosts, with the dose in each subvolume homogeneously prescribed (145). Dose painting by numbers refers to the voxel-by-voxel prescription of dose to biological information from images (145–148).

Dose painting by contours has been notably suggested for the treatment of prostate and lung cancer, among others (149–152). Piroth et al. (153) have used automatically contoured boost volumes of glioblastoma using a ^{18}F-fluoroethyltyrosine (^{18}F-FET) PET tumour-to-brain ratio threshold of ≥ 1.6. However, a simultaneous integrated boost of 72 Gy in 30 fractions delivered to those volumes with IMRT, concurrent with 60 Gy in 30 fractions delivered to a conventional MRI-defined PTV, did not lead to a survival benefit (95). A treatment planning study of glioblastoma patients for a simultaneous integrated boost of 72 Gy to three-dimensional magnetic resonance spectroscopic imaging (MRSI)-

defined volume delivered with IMRT did not increase dose to normal tissues (154).

Dose painting by numbers has been demonstrated in planning studies with ^{18}F-fluoromisonidazole PET, a biomarker of hypoxia (155), and clinical trials with ^{18}F-fluorodeoxyglucose (^{18}F-FDG) PET for head and neck cancers (148, 156). For brain tumours, the feasibility of dose painting by numbers using ^{18}F-FET PET for IMRT and intensity-modulated proton therapy has been demonstrated in treatment planning studies (96, 157).

3,4-dihydroxy-6-[^{18}F]fluoro-L-phenylalanine (^{18}F-FDOPA) PET may also be appropriate for dose painting in the management of high-grade glioma since ^{18}F-FDOPA PET identifies regions of high tumour cell density and higher-grade disease (79). While other dose escalation strategies have not shown a survival benefit for patients, dose painting may improve tumour control by directing escalated dose to regions of high tumour cell density or high proliferation. Thus, the purpose of this study was to determine the feasibility of dose painting obtained from ^{18}F-FDOPA uptake for the treatment of high-grade gliomas using VMAT. Dose painting is achieved by contouring biological target volumes (BTVs) using ^{18}F-FDOPA PET for five patients. The dose prescribed to each BTV was specified by a radiobiological model. This method was compared with VMAT plans obtained without dose escalation to conventional MRI-based contours to determine the potential benefit, if any, can be obtained with biological-based treatment planning of high-grade gliomas, while maintaining acceptable avoidance of critical structures in the brain.

4.2 Methods and Materials

4.2.1 Patients and Imaging

Five patients from the cohort of patients described in Chapter 3 were selected. Postoperative planning CT and MRI, T1-weighted images with gadolinium contrast enhancement obtained with the turbo spin echo (TSE) sequence and T2-weighted fluid attenuated inversion recovery (FLAIR) images, were obtained. Preoperative and postoperative ^{18}F-FDOPA PET were also obtained. Technical details for these imaging modalities are discussed Sections 2.2.1 and 3.2.2. All image sets (planning CT, MRI, and PET/CT) were imported into Eclipse treatment planning system (Varian Medical Systems, Palo Alto, CA) and fused using the Eclipse auto-matching registration algorithm. The planning CT images were fused to both the MRI and the CT image set of the ^{18}F-FDOPA PET/CT.

4.2.2 Volume Delineation

Target volume and OAR delineations were imported from each patient's treated radiation therapy plan. The GTV was contoured by each patient's attending radiation oncologist as the contrast-enhancing tumour on T1-weighted and T2-weighted MRI, excluding the surgical cavity. The clinical target volume (CTV) was defined as a 2-cm expansion of the GTV and surgical cavity. The PTV was defined as a 0.5-cm expansion of the CTV. The dose prescribed in the PTV was 60 Gy in 30 fractions (10, 49). OARs used for treatment planning were the brainstem, optic nerves and chiasm, anterior chambers, and retinas. Margins were not added to OAR contours. Normal brain was not used as an OAR planning constraint in this study.

A radiation oncologist experienced with ^{18}F-FDOPA PET images delineated a volume of interest for dose painting on either the preoperative or postoperative ^{18}F-FDOPA PET. Seven BTVs (BTV62.5, BTV65, BTV67.5, BTV70, BTV72.5, BTV75, and BTV75.5) inside the volume of interest were delineated by thresholding of the ^{18}F-FDOPA uptake. These volumes corresponded to dose boosts of 62.5 Gy to 77.5 Gy, in 2.5 Gy steps. The image intensity threshold I for each BTV was calculated using a linear quadratic model that assumes that the image intensity is linearly related to the tumour cell density ρ in each image voxel. For the number of surviving cells in each voxel to be the same:

$$\rho \cdot \mathrm{SF}_2^{\frac{D}{D_{\mathrm{ref}}} \cdot \frac{\alpha/\beta + D/n_f}{\alpha/\beta + D_{\mathrm{ref}}}} = \rho_0 \cdot \mathrm{SF}_2^{\frac{D_0}{D_{\mathrm{ref}}} \cdot \frac{\alpha/\beta + D_0/n_f}{\alpha/\beta + D_{\mathrm{ref}}}}, \tag{4.1}$$

where D is the prescribed dose for the BTV, $D_0 = 60$ Gy is the prescribed dose in the PTV, $n_f = 30$ is the number of fractions, $\alpha/\beta = 10$ Gy, and SF_2 is the surviving fraction of cells after a single dose of $D_{\mathrm{ref}} = 2$ Gy (64, 72, 158). Assuming that $I/I_0 = \rho/\rho_0$:

$$\ln \frac{I}{I_0} = -\ln \mathrm{SF}_2 \left[\frac{D\left(\alpha/\beta + D/n_f\right) - D_0\left(\alpha/\beta + D_0/n_f\right)}{D_{\mathrm{ref}}(\alpha/\beta + D_{\mathrm{ref}})} \right]. \tag{4.2}$$

SF_2 was chosen so that that a boost of $D = 80$ Gy would correspond with the maximum image intensity I_{max} in the ^{18}F-FDOPA volume of interest in each patient. I_0 was the minimum image intensity for dose boosting. For this study, it was chosen only to escalate dose in regions where the image intensity was larger than the image intensity at the anatomic border of the basal ganglia. An example of the dose painting model is shown in Figure 4.1(a). The dose escalation steps for this model are shown in Figure 4.1(b)–(d). An example of the target volumes is shown in Figure 4.2.

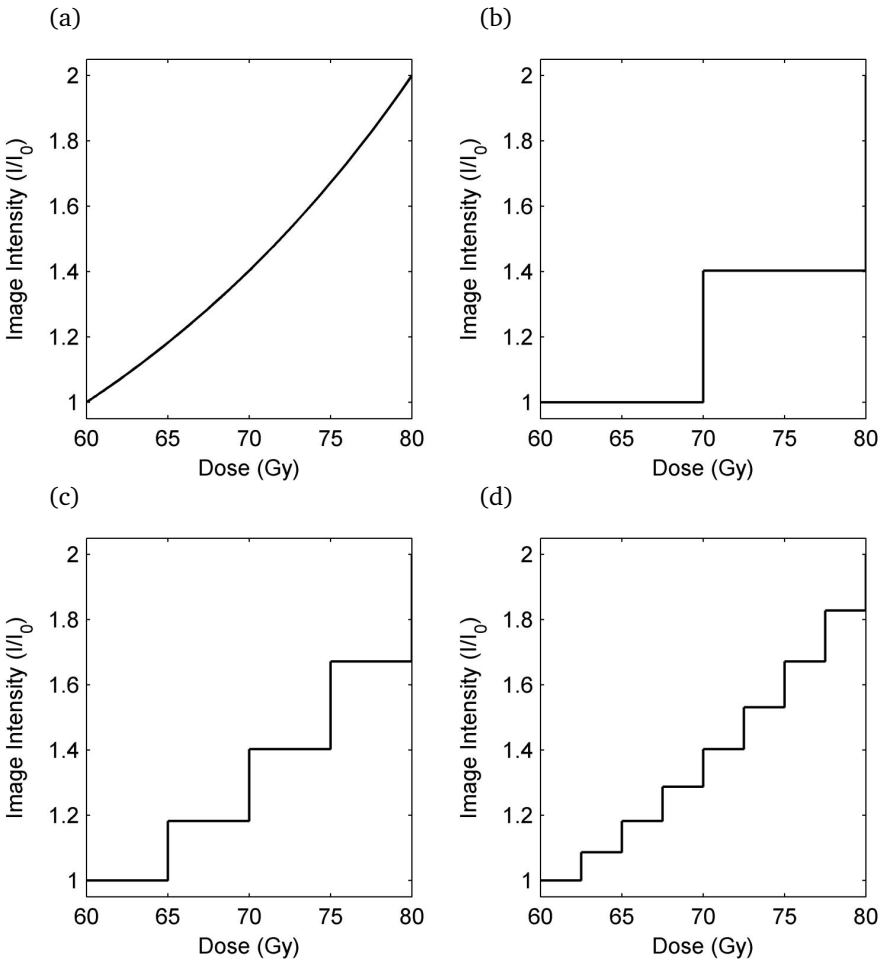

Figure 4.1. (a) The dose that was prescribed for dose painting as a function of image intensity (I/I_0). The maximum dose was fixed at 80 Gy. The dose painting levels that were used to derive biologically-based volumetric modulated arc therapy plans of high-grade gliomas are shown using (b) one dose escalation step (i.e., simultaneous integrated boost of 70 Gy), (c) three dose escalation steps (65 Gy, 70 Gy, and 75 Gy), and (d) seven dose escalation steps (62.5 Gy to 77.5 Gy, in steps of 2.5 Gy).

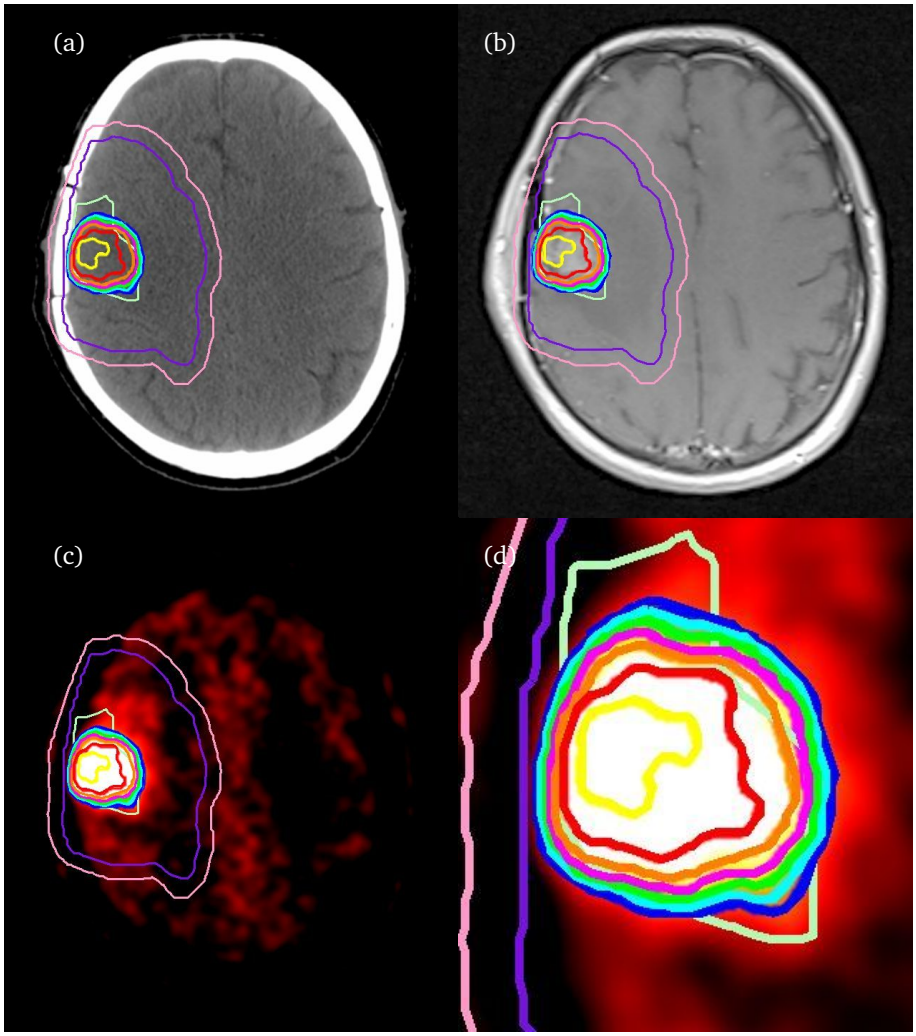

Figure 4.2. Biological target volumes shown on (a) computed tomography, (b) magnetic resonance imaging, and (c) ^{18}F-FDOPA positron emission tomography. Contours shown are the BTV62.5 (blue), BTV65 (cyan), BTV67.5 (green), BTV70 (magenta), BTV72.5 (orange), BTV75 (red), and BTV75.5 (yellow), GTV (light green), CTV (violet), and PTV (pink). Panel (d) shows a close up of panel (c).

4.2.3 Radiation Therapy Planning

For each patient, four VMAT plans were generated using Eclipse treatment planning software using the Anisotropic Analytical Algorithm (version 11.031) for dose calculations and Progressive Resolution Optimization (version 11.031) for VMAT optimization. Plans were obtained using a single 360° arc of a 6-MV photon beam from a Varian TrueBeam linear accelerator with High Definition 120-leaf multileaf collimator (MLC). The field arrangement is shown in Figure 4.3. First, a treatment plan was obtained without any dose escalation. The dose volume histogram (DVH) planning objectives that were used for treatment planning are shown in Table 4.1. In the case of overlapping target and OARs, plan optimization was done with non-overlapping PTVs (PTV60, the portion of the PTV that does not overlap with OARs; PTV54, the portion of the PTV that overlaps with the optic nerve or chiasm; and PTVb, the portion of the PTV that overlaps with the brainstem) and OARs (brainstem_opti and optic_opti, the portion of the brainstem and optic structures that do not overlap the PTV). In addition, it was attempted to reduce the mean dose in the OARs to as small as possible while maintaining dosimetric coverage of the PTV.

Dose painting was achieved by progressively adding dose constraints to the BTVs on the treatment plan without any dose escalation. Dose constraints were added with the expectation the mean dose in the BTVs would be similar to the prescribed dose escalation. The second treatment plan added a simultaneous integrated boost of 70 Gy to the BTV70 structure. Coverage inside BTV70 required that $V_{66.5\ \mathrm{Gy}} \geq 98\%$ (coverage of 95% of the prescribed dose boost) and a maximum dose of 72.5 Gy. For the third treatment plan, constraints for BTV65 ($V_{61.8\ \mathrm{Gy}} \geq 98\%$), BTV70 ($V_{66.5\ \mathrm{Gy}} \geq 98\%$), and BTV75 ($V_{71.3\ \mathrm{Gy}} \geq 98\%$ and a maximum dose of 77.5 Gy). For the final treatment plan, the dose in the BTVs

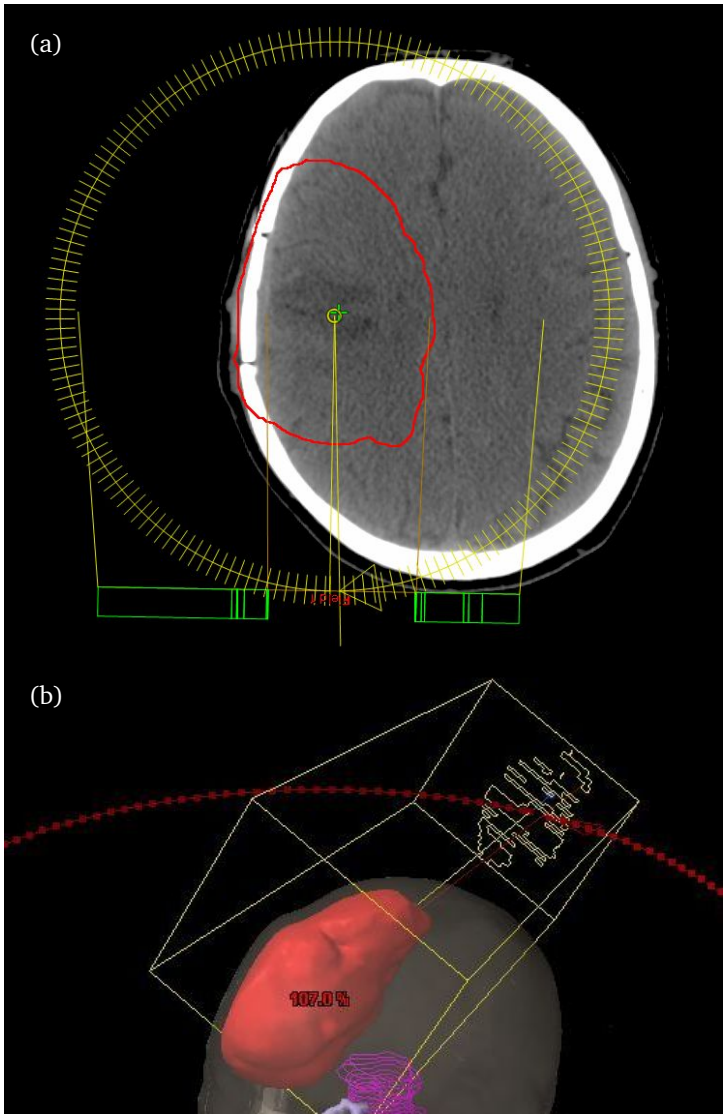

Figure 4.3. The field arrangement for volumetric modulated arc therapy is shown for (a) axial and (b) three-dimensional views. The planning target volume is shown in red.

Table 4.1. Dose volume histogram constraints used for volumetric modulated arc therapy.

Structure	Type	Constraint
No overlapping volumes		
PTV	Target	$V_{95\%} \geq 98\%$ and $D_{\max} = 107\%$
Optic Chiam and Nerve	OAR	$V_{54\ \mathrm{Gy}} \leq 1\%$
Brainstem	OAR	$D_{\max} = 60$ Gy
Retina	OAR	$D_{\max} = 45$ Gy
Anterior Chamber	OAR	$D_{\max} = 10$ Gy
Overlapping target and OARs		
PTV54	Target	$V_{54\ \mathrm{Gy}} \leq 1\%$ and $V_{51.3\ \mathrm{Gy}} \geq 98\%$
PTV60	Target	$V_{95\%} \geq 98\%$ and $D_{\max} = 107\%$
PTVb	Target	$V_{95\%} \geq 98\%$ and $D_{\max} = 60$ Gy
Optic_opti	OAR	$V_{54\ \mathrm{Gy}} \leq 1\%$
Brainstem_opti	OAR	$D_{\max} = 60$ Gy
Retina	OAR	$D_{\max} = 45$ Gy
Anterior Chamber	OAR	$D_{\max} = 10$ Gy
Dose escalation volumes for dose painting		
BTV62.5	BTV	$V_{59.4\ \mathrm{Gy}} \geq 98\%$
BTV65	BTV	$V_{61.8\ \mathrm{Gy}} \geq 98\%$
BTV67.5	BTV	$V_{64.1\ \mathrm{Gy}} \geq 98\%$
BTV70	BTV	$V_{66.5\ \mathrm{Gy}} \geq 98\%$
BTV72.5	BTV	$V_{68.9\ \mathrm{Gy}} \geq 98\%$
BTV75	BTV	$V_{71.3\ \mathrm{Gy}} \geq 98\%$
BTV77.5	BTV	$V_{73.6\ \mathrm{Gy}} \geq 98\%$ and $D_{\max} = 80$ Gy

Abbreviations: BTV = biological target volume; max = maximum; OAR = organ at risk; PTV = planning target volume.

was constrained so that at least 98% of each volume was covered by 95% of its prescribed dose boost and that the maximum dose in BTV77.5 was 80 Gy (Table 4.1). For all dose escalation schemes, it was also attempted to reduce the mean dose to the OARs. These progressive dose painting steps are illustrated in Figure 4.1(b)–(d).

4.2.4 Evaluation of Treatment Plans

The number of monitor units (MUs) required to deliver a 2-Gy fraction was recorded for each treatment plan. In addition, a dosimetric comparison of the VMAT plans without dose escalation and with all dose painting steps was performed using cumulative DVHs and dosimetric parameters for the PTV, BTVs, and OARs, including mean and maximum doses. In addition, conformity of the PTV was quantified using the conformity index (CI), which is defined as:

$$\mathrm{CI} = \frac{\text{95\% isodose surface volume}}{\text{PTV volume}}. \tag{4.3}$$

The ideal value for the CI in this study is 0.98. Homogeneity of the dose in the PTV was quantified using the homogeneity index (HI), which is defined as:

$$\mathrm{HI} = \frac{\text{Max. \% dose in PTV}}{\text{95\%}}. \tag{4.4}$$

For plans with dose escalation, dose homogeneity was calculated using the portion of the PTV excluding the BTVs.

In addition, the equivalent uniform dose (EUD) (Eq. 1.38) was calculated for each OAR. The EUD was calculated using the generalized EUD (74):

$$\mathrm{EUD} = \left(\sum_{i=1}^{N} v_i \, \mathrm{NTD}_i^a \right)^{1/a} \tag{4.5}$$

where $a = 1/n$. Values for the volume dependence parameter n for each OAR were obtained from the Quantitative Analysis of Normal Tissue Effects in the Clinic review papers (159–161) and those reported by Burman et al. (70). The normalized total dose (NTD) (Eq. 1.36) was calculated with $\alpha/\beta = 2$ Gy for all OARs (158, 162).

Table 4.2. Characteristics of patients planned for volumetric modulated arc therapy with dose painting.

No.	Age	Histology	PET Image	Volume (cm^3)	
				PTV	BTV62.5
1	61	Glioblastoma	Preop	343	20.2
2	80	Glioblastoma	Preop	152	6.8
3	51	Glioblastoma	Postop	329	5.7
4	60	Glioblastoma	Postop	439	1.4
5	31	Anaplastic astrocytoma	Postop	320	3.2

Abbreviations: BTV = biological target volume; PET = positron emission tomography; Postop: postoperative; Preop: preoperative; PTV = planning target volume.

Statistical comparisons of dose-volume metrics and EUDs were performed using MATLAB (version 7.0.0.19920; The MathWorks, Inc., Natick, MA) using two-sided paired t-tests ($\alpha = 0.05$).

4.3 Results

Patient characteristics are shown in Table 4.2. Patient 2 had a PTV that overlapped with the brainstem and optic nerve. The target volumes did not overlap with OARs for all other patients. The mean PTV volume was 317 cm^3 (range, 152–439 cm^3). The mean dose escalation volumes were 7.4 cm^3 (1.4–20.3 cm^3) for BTV62.5, 5.7 cm^3 (1.1–17.2 cm^3) for BTV65, 4.5 cm^3 (0.9–14.6 cm^3) for BTV67.5, 3.4 cm^3 (0.7–11.8 cm^3) for BTV70, 2.4 cm^3 (0.5–9.0 cm^3) for BTV72.5, 1.3 cm^3 (0.2–5.5 cm^3) for BTV75, and 0.2 cm^3 (0.0–0.8 cm^3) for BTV77.5.

It was possible to produce dose painting plans for all cases without sacrificing dose conformity within the PTV (Figure 4.4). Examples of the distribution of isodose lines for VMAT plans without dose escalation and with dose paint-

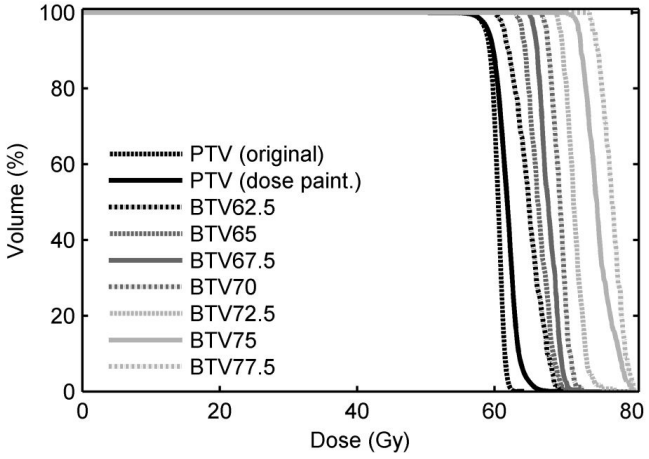

Figure 4.4. A dose volume histogram for the planning target volume (PTV) without dose escalation, and the PTV (excluding the dose escalation region) and biological target volumes (BTVs) with dose painting for a sample patient (Patient 1).

ing are shown in Figure 4.5. Dose distributions are illustrated in Figure 4.6. The mean number of MUs to treat a 2-Gy fraction was 380 (range, 353–405) for VMAT plans without dose escalation and 430 (401–472) for VMAT plans with dose painting. This difference was significant ($p = 0.01$). The conformity of the 95% isodose surface between plans was similar. The mean CI was 1.16 (1.05–1.48) without dose escalation and 1.20 (1.05–1.63) with dose painting ($p = 0.32$). The HI inside the PTV was 1.12 (1.12–1.14) without dose escalation and 1.30 (1.25–1.33) with dose painting ($p < 0.001$). This was expected since dose escalation by design will increase the HI.

The dosimetric comparison of OARs for plans with and without dose painting is shown in Table 4.3. For all cases, OAR mean and maximum doses were not significantly different between VMAT plans without dose escalation and with dose painting. In addition, dose painting VMAT plans produced EUDs that were similar to those for plans produced with no dose escalation in all cases

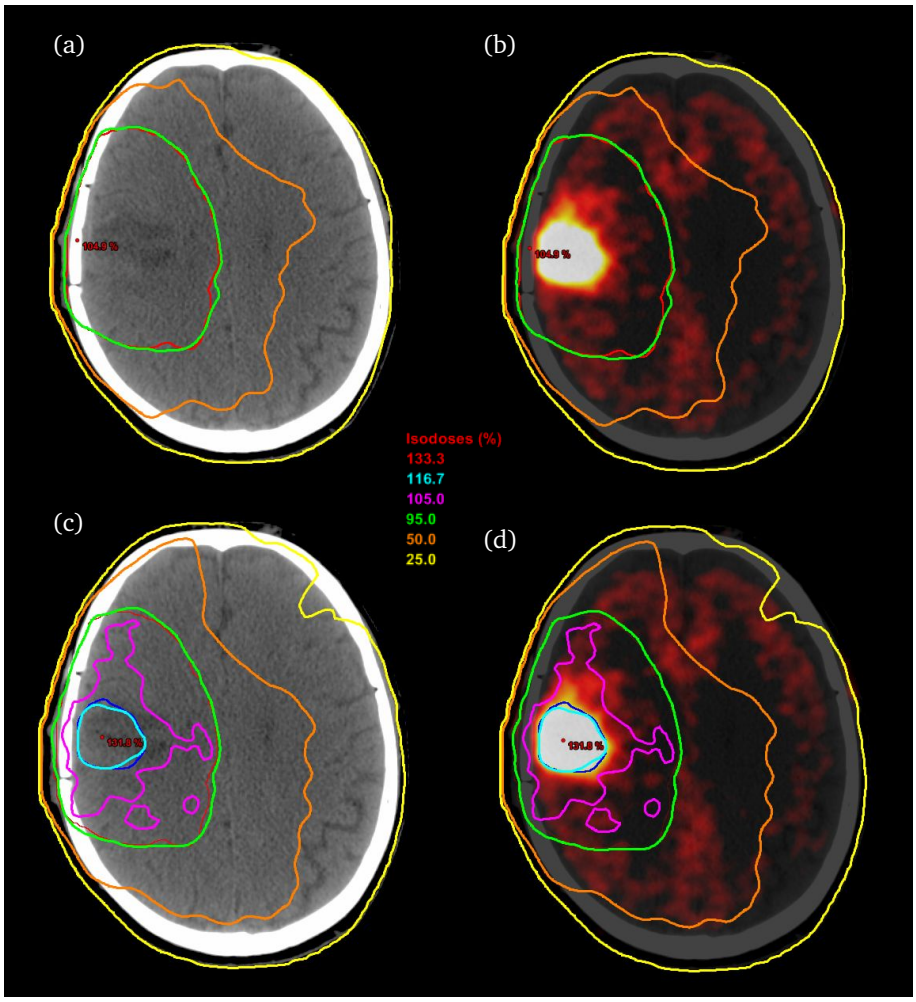

Figure 4.5. Isodose lines are shown for a volumetric modulated arc therapy (VMAT) plan without dose escalation on (a) computed tomography (CT) and (b) ^{18}F-FDOPA positron emission tomography (PET), and a VMAT plan with dose painting on (c) CT and (d) ^{18}F-FDOPA PET. The planning target volumes is shown in red and the BTV70 structure is shown in blue.

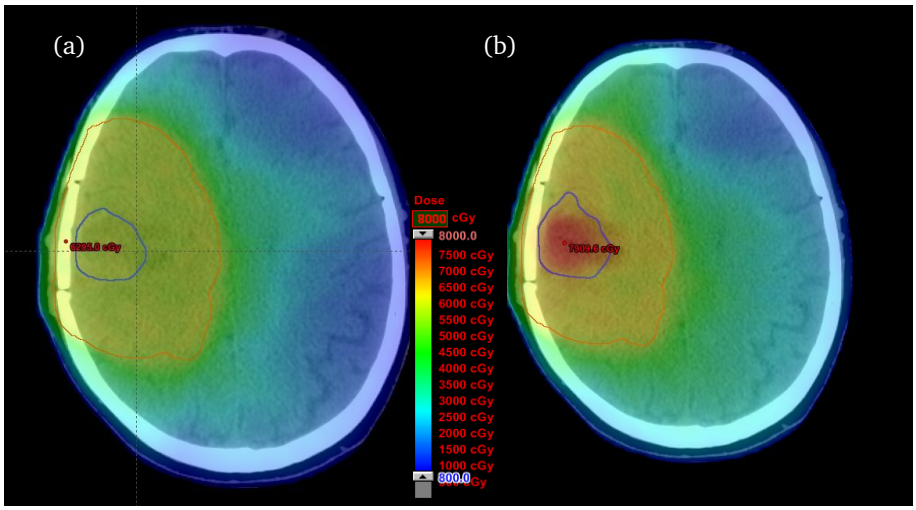

Figure 4.6. The dose distribution from the case in Figure 4.5 is shown for volumetric modulated arc therapy plans (a) without dose escalation and (b) with dose painting. The planning target volume is shown in red and the BTV70 structure is shown in blue.

(Table 4.4). The DVHs for the brainstem, optic nerve and chiasm, retinas, and anterior chambers are shown for most complex case (Patient 2) with overlapping PTV and OARs are shown in Figures 4.7–4.9. Even in this complex case, similar DVHs were obtained for all OARs for plans without dose escalation and with dose painting.

4.4 Discussion

This study has shown that dose painting with ^{18}F-FDOPA PET contours was possible with VMAT planning of high-grade gliomas without increasing the dose delivered to critical structures. This is the first study to show the feasibility of VMAT dose painting for gliomas. Dosimetric data of glioma VMAT in this study is similar to those reported by others (49, 163). However, this study did not use a clinically-implemented protocol and normal brain was not used as an

Table 4.3. Dosimetric comparison of organs at risk for volumetric modulated arc therapy plans with and without dose painting.

Structure	Original*	Dose Painting*	*p*-value
Mean Dose (Gy)			
Brainstem	25.0 (11.6–42.5)	24.3 (10.7–43.1)	0.30
Left retina	4.7 (2.1–7.2)	3.8 (1.9–6.2)	0.10
Right retina	4.1 (2.2–7.6)	3.9 (1.5–7.1)	0.52
Left anterior chamber	3.4 (1.8–4.5)	2.9 (1.7–4.1)	0.14
Right anterior chamber	3.2 (1.8–5.2)	3.0 (1.3–4.8)	0.33
Optic nerve & chiasm	19.3 (9.3–34.7)	18.6 (8.9–34.0)	0.10
Maximum Dose (Gy)			
Brainstem	54.6 (45.5–60.1)	52.1 (39.2–59.9)	0.11
Left retina	9.6 (5.6–15.1)	7.6 (4.8–11.8)	0.05
Right retina	8.5 (3.5–16.7)	8.2 (2.2–16.7)	0.48
Left anterior chamber	6.1 (3.8–8.1)	5.1 (3.3–6.9)	0.18
Right anterior chamber	5.5 (3.2–7.8)	5.3 (2.3–8.1)	0.58
Optic nerve & chiasm	35.1 (16.3–53.9)	34.4 (14.5–53.8)	0.33

*Mean values are shown, with the range in parentheses.

Table 4.4. Comparison of equivalent uniform doses, in Gy, of organs at risk for volumetric modulated arc therapy plans with and without dose painting.

Structure	*n**	Original**	Dose Painting**	*p*-value
Brainstem	0.16	33.8 (18.7–48.9)	32.2 (15.8–48.7)	0.08
Left retina	0.2	3.1 (1.3–4.9)	2.4 (1.2–4.0)	0.06
Right retina	0.2	2.8 (1.2–5.5)	2.7 (0.8–5.3)	0.46
Left anterior chamber	0.25	1.9 (1.0–2.7)	1.6 (0.9–2.3)	0.11
Right anterior chamber	0.25	1.8 (1.0–2.8)	1.7 (0.7–2.6)	0.23
Optic nerve & chiasm	0.3	19.7 (6.1–37.8)	19.3 (5.8–37.6)	0.07

*Volume parameter used for equivalent uniform dose calculation.
**Mean values are shown, with the range in parentheses.

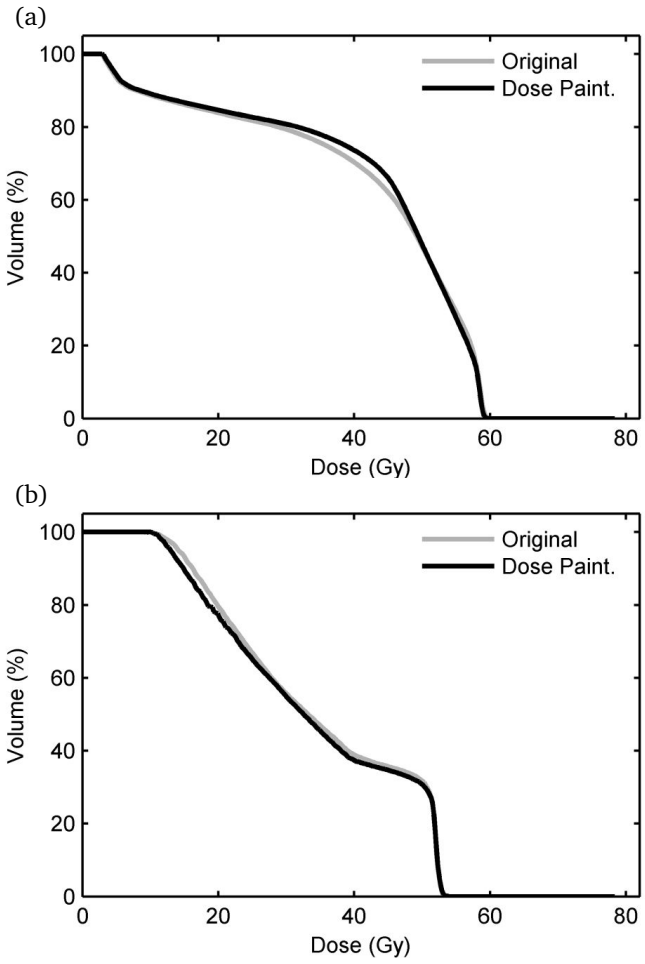

Figure 4.7. Dose volume histograms for the (a) brainstem and (b) optic chiasm and nerves for volumetric modulated arc therapy plans without dose escalation (gray line) and with dose painting (black line) for a sample patient (Patient 2).

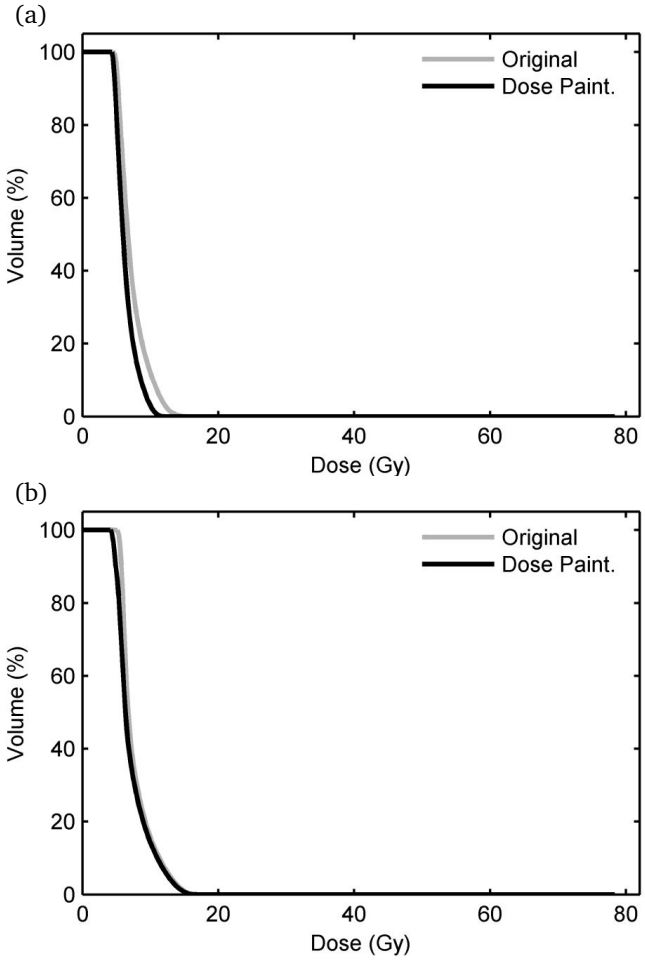

Figure 4.8. Dose volume histograms for the (a) left and (b) right retinas for volumetric modulated arc therapy plans without dose escalation (gray line) and with dose painting (black line) for a sample patient (Patient 2).

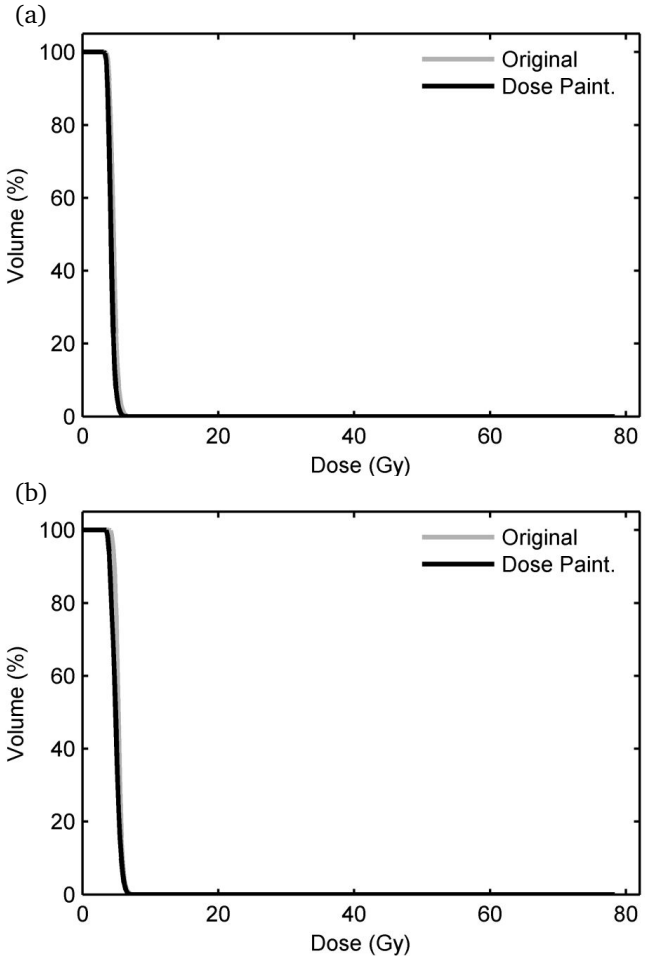

Figure 4.9. Dose volume histograms for the (a) left and (b) right anterior chambers for volumetric modulated arc therapy plans without dose escalation (gray line) and with dose painting (black line) for a sample patient (Patient 2).

OAR planning constraint in this study. This may result in larger normal brain doses as compared to plans obtained with IMRT (49). Further reduction in normal tissue doses may be possible if normal brain was included in the plan optimization process. This study also only used a single treatment arc. It has been reported that the use of noncoplanar VMAT reduced dose to the lower contralateral temporal lobe dose for patients with fronto-temporal high-grade glioma (163). The use of noncoplanar VMAT for dose painting may potentially reduce normal brain doses while allowing dose escalation to abnormalities on ^{18}F-FDOPA PET.

The unique biologically-guided choice of dose painting thresholds in this study allows for dose painting with multiple contours to be performed with clinically-available treatment planning software. However, this method relied on the choice of radiobiological parameters for the assignment of dose painting thresholds. Qi et al. (64) reported the radiosensitivity parameters for gliomas from clinical outcomes data to be $\alpha = 0.06 \pm 0.05$ Gy^{-1} and $\alpha/\beta = 10.0 \pm 15.1$ Gy. From these values, $SF_2 = 0.87$, suggesting strongly radioresistant cells. This value is similar to the SF_2 values used in this study. For example, $SF_2 = 0.94$ was used to obtain the curve in Figure 4.1(a) with the assumption $\alpha/\beta = 10$ Gy. The choice of radiosensitivity parameters may be crucial to potential improvement of patient outcomes. Furthermore, the functional relationship between ^{18}F-FDOPA uptake and tumour cell density is not known in relative or absolute terms. The impact of image acquisition parameters and reconstruction algorithms on dose painting also needs to be established. Research is needed to provide this data.

Tumour-to-background ratios are often used to define simultaneous integrated boost volumes. Piroth et al. (153) used the ^{18}F-FET PET tumour-to-brain ratio of ≥ 1.6 since it was assumed that this value would to give a 5-mm safety

margin to ratios of 2.0–2.6 which have been reported to identify malignant cells (164–166). But use of this threshold to define a simultaneous integrated boost of 72 Gy in 30 fractions did not lead to a survival benefit (95). Using three-dimensional MRSI, Ken et al. (154) defined a simultaneous integrated boost to a GTV defined by a choline-to-*N*-acetyl-aspartate ratio > 2. ^{11}C-MET-defined GTVs have also been defined using a tumour-to-brain ratio of 2 (138). Recently reported biopsy data suggested that an optimal ^{18}F-FDOPA PET tumour-to-brain ratio of > 2 as a threshold that identifies high-grade disease for newly diagnosed and recurrent glioma (79). This suggests a useful threshold for dose painting (i.e., I_0 in this study), although more clarity is needed before clinical implementation. In addition, an appropriate margin would need to be added to the BTVs for clinical implementation of the biologically-guided technique presented here. The treatment technique would need to be chosen (i.e., small set-up margin) to ensure that the dose distribution as closely as possible matches the biological information from PET.

Planning studies which report dose painting by numbers for gliomas have used linear models to map image intensity or standardized uptake value (SUV) to dose (96, 157). The model presented in this study can also be used to add radiobiological-guidance for dose painting by numbers. Other biological models can also be employed. For example, normal tissue complication probability (NTCP) and tumour control probability (TCP) have been investigated for dose painting subvolumes for prostate treatments (77). For head and neck cancer, TCP-based models have proposed (148, 167).

Multimodality approaches have shown that different imaging techniques can show different dose escalation volumes. In a recent study by Houweling et al (168), ^{18}F-FDG PET and apparent diffusion coefficient (ADC)-based target volumes for head and neck cancer patients showed minimal overlap. This

has important implications dose painting treatment techniques since there was poor dose coverage inside ADC-based target volumes for dose painting plans obtained using a PET PTV. For high-grade gliomas, a recent study found minimal overlaps of the ADC value and the maximum ^{18}F-FDOPA PET SUV ratio (128). Multimodality approaches for dose painting are needed to fully assess dose painting treatment plans and compare these imaging parameters with patterns of failure.

Despite the small number of patients ($n = 5$), this study has demonstrated a unique, biologically-guided and physically-based VMAT planning method for high-grade glioma treatments. However, the dose escalation volume for most patients was small since ^{18}F-FDOPA PET was used for neuronavigation during surgery. This study did not include patients with tumours near the basal ganglia since there is intense normal uptake of ^{18}F-FDOPA in these structures (37). Dose painting techniques for tumours near these structures may be more difficult. As noted in Chapter 2, another difficulty with using ^{18}F-FDOPA PET is that postsurgical changes around the resection cavity can exhibit tracer uptake because of high levels of amino acid transport by activated macrophages or ^{18}F-FDOPA leakage due to disruption of the blood-brain barrier (97). This study anticipated this challenge by having a radiation oncologist with experience with ^{18}F-FDOPA PET images delineate volumes of interest for dose escalation. In addition, care must be taken with any automatic segmentation methods that may include regions of normal ^{18}F-FDOPA uptake in basal ganglia or in dose escalation volumes.

Chapter 5

Conclusions and Future Work

5.1 Conclusions

This project has demonstrated that biological information from functional imaging techniques, such as positron emission tomography (PET) and diffusion tensor imaging (DTI), can potentially be used to improve localization of malignant tissue and for biologically-based treatment planning. First, it was demonstrated that high-grade glioma radiation therapy target volumes obtained with 3,4-dihydroxy-6-[^{18}F]fluoro-L-phenylalanine (^{18}F-FDOPA) PET had similar interobserver agreement than volumes obtained with magnetic resonance imaging (MRI) with gadolinium contrast enhancement. Although consensus target volumes obtained using ^{18}F-FDOPA PET were significantly larger than volumes obtained using MRI, treatment planning using the PET-based volumes may not have yielded better treatment outcomes since all but one central recurrence extended beyond the PET gross tumour volume (GTV) and most were contained by a 2-cm margin on the MRI GTV.

Radiation therapy target localization for high-grade gliomas was potentially possible using DTI. Fractional anisotropy (FA) were significantly smaller and mean diffusivity (MD) was significantly larger in the GTV as compared to contralateral normal brain tissue. FA and MD values, as well as FA and MD interhemispheric differences approached those of normal brain tissue as the distance

from the GTV increased, consistent with the expectation of a gradual and decreasing presence of tumour cells. Interhemispheric difference images obtained from DTI provide images that may allow easier interpretation of DTI data, as compared to images of FA and MD. Further research is warranted to determine if treatment planning using interhemispheric difference images images can be used to improve target delineation or be used for biologically-based treatment planning, potentially improving treatment outcomes.

Lastly, volumetric modulated arc therapy (VMAT) planning using dose painting for high-grade gliomas was achieved using biological target volumes (BTVs) obtained from biologically-guided thresholds of ^{18}F-FDOPA PET images. There was no significant difference in the dose delivered to critical normal structures between plans without dose escalation and plans with dose painting. While further research is needed to clarify radiosensitivity parameters and thresholds for dose escalation, dose painting using ^{18}F-FDOPA can be implemented using clinically-available VMAT optimization techniques.

5.2 Future Work and Other Applications

In this thesis, the radiation therapy applications of ^{18}F-FDOPA PET and DTI have been discussed. However, the addition of these imaging techniques to neurosurgical resection planning may improve patient survival since the extent of resection is associated with survival in patients with high-grade disease (169). Incorporation of ^{18}F-FDOPA PET images may allow neurosurgeons to identify higher-grade and higher-density disease than that which could be identified from T1-weighted contrast-enhancement MRI (79, 94).

^{18}F-FDOPA PET has other applications as well, such as the detection of recurrent glioma. While the diagnostic accuracies of the detection of recurrent

tumours with ^{18}F-FDOPA PET and T1-weighted MRI are similar, ^{18}F-FDOPA PET is more specific than MRI for recurrent glioma detection (170). Karunanithi et al. (171) have reported a multivariate analysis which shows that tumour size on MRI and the standardized uptake value (SUV) ratio of tumour to contralateral normal brain from ^{18}F-FDOPA PET were independent predictors of patient survival for recurrent glioma. ^{18}F-FDOPA PET parametric response maps (voxel-wise changes in ^{18}F-FDOPA uptake in time) may also be a useful biomarker of progression free survival and overall survival for patients with recurrent glioma treated with bevacizumab (172).

The use of DTI for neurosurgical resection of glioma is well established (173, 174). In a prospective, randomized controlled trial, Wu et al. (175) reported that there was a significant survival benefit for patients with cerebral high-grade glioma with pyramidal tract involvement who underwent surgery with DTI-based neuronavigation (21.2 months) compared to those operated on with routine neuronavigation (14.0 months) ($p = 0.048$). Mathematical modeling of glioma growth has also been investigated using DTI to predict anisotropic pathways for glioma cell invasion and identify potential locations for recurrence (90, 98, 101, 176, 177).

Many studies have also investigated the use of preoperative diffusion imaging to distinguish glioma from other pathologies, such as brain metastases, demyelinating diseases, and radiation-induced injury (178–184). Axial and radial diffusivities have been suggested as biomarkers to distinguish low-grade and high-grade gliomas (185). The decrease of FA in peritumoural white matter has been reported to be significantly different for patients with glioma and meningioma (186). In another study, FA and MD values were significantly smaller in cerebral lymphoma than the values for glioblastoma (187). Despite these efforts, the gold standard remains histological analysis (174).

Other imaging techniques may also be appropriate for radiation therapy planning. For example, arterial spin labeling has been shown to improve the diagnostic accuracy of preoperative glioma grading (188). The high fractional cerebral blood volume obtained from T2*-weighted dynamic susceptibility contrast MRI, may identify regions that are radioresistant and thus benefit from radiation dose escalation (189). Pharmacokinetic parameters from T1-weighted dynamic contrast enhanced MRI have been suggested to differentiate tumour from radiation-induced injury and surrounding brain tissue (190, 191). The choline-to-*N*-acetyl-aspartate ratio obtained from magnetic resonance spectroscopic imaging (MRSI) can identify abnormal metabolically active regions that can be used to define target volumes for primary and boost volumes (192, 193). Single photon emission computed tomography (SPECT)/computed tomography (CT) with ^{99m}Tc-glucoheptonate has been suggested as a low-cost alternative to ^{18}F-FDOPA PET for detection of recurrent glioma (194). Sodium concentrations obtained from ^{23}Na-MRI may potentially be used to differentiate between low-grade and high-grade glioma (195, 196).

The dose painting technique proposed in this thesis may ultimately allow for radiation treatment plans for high-grade gliomas to conform to the biological information obtained from ^{18}F-FDOPA PET or DTI, as originally envisioned by the concept of multidimensional radiotherapy introduced by Ling et al. (75). While the feasibility of dose painting by contours (95, 153, 154) and by numbers (96, 157) for glioma treatments has been investigated, there is a need for more research. Although dose escalation up to 84 Gy can be delivered without increased incidence radionecrosis or normal tissue effects (143, 154), there is not yet any evidence that dose escalation will improve patient outcomes (95). In this project, it has been demonstrated that ^{18}F-FDOPA PET and DTI can potentially be used for biological-guidance in radiation therapy and that dose painting

can be achieved using commercially-available VMAT optimization without increased dose to normal tissues. However, there is the need for more research before these techniques can be implemented clinically. The choice of image thresholds used for dose painting, or the function used to prescribed dose from image intensities for dose painting by numbers, are crucial to any biologically-guided technique. While there is limited evidence for appropriate thresholds for ^{18}F-FDOPA PET (79), more research is needed to determine appropriate threshold for biologically-based radiation therapy of gliomas. In addition it must be noted that the threshold values may also depend on target-to-background intensity ratios, reconstruction algorithms, and the type of scanner used (197, 198).

There is also a need for more clinical investigations to determine the role of biological guidance in the treatment of high-grade glioma. Currently, there is no consistent data to provide a rationale for the use of heterogeneous, biologically-based treatment planning (74). Preclinical studies with animal models are needed to provide this data. In addition, any biologically-guided treatment planning technique will require a robust acceptance and commissioning, quality assurance, and treatment plan evaluation procedures, such as those outlined in the report of Task Group 166 of the American Association of Physicists in Medicine (74). It is important that any biologically-based treatment plan be evaluated using established dose volume histogram (DVH) criteria. The review of three-dimensional dose distributions is also essential to ensure that quality radiation therapy plans are obtained. Moreover, the effect of cold spots in the GTV may be underestimated for plans optimized by dose painting and care must be taken to ensure that hot spots within the planning target volume (PTV) are located within the GTV (74). Any validation of such techniques must ultimately be based on the assessment of three-dimensional patterns of failure following treatment (197).

This project has demonstrated the feasibility of biologically-guided radiation therapy of high-grade gliomas through the use of ^{18}F-FDOPA PET or interhemispheric difference images of DTI-based parameters. While much work must still be done before these techniques can be introduced clinically, the use of ^{18}F-FDOPA PET and DTI during radiation therapy planning may improve tumour localization and be used for VMAT dose painting, thereby potentially improving survival for patients with high-grade glioma.

Bibliography

1. Rizzo DC. Fundamentals of anatomy and physiology. 1st ed. Clifton Park (NY): Delmar Cengage Learning; 2000.

2. Ostrom QT, Gittleman H, Farah P, Ondracek A, Chen Y, Wolinsky Y, et al. CBTRUS statistical report: primary brain and central nervous system tumors diagnosed in the United States in 2006-2010. Neuro Oncol. 2013;15 Suppl 2:ii1–ii56.

3. Louis DN, Ohgaki H, Wiestler OD, Cavenee WK, Burger PC, Jouvet A, et al. The 2007 WHO classification of tumours of the central nervous system. Acta Neuropathol. 2007;114(2):97–109.

4. Daumas-Duport C, Scheithauer B, O'Fallon J, Kelly P. Grading of astrocytomas. A simple and reproducible method. Cancer. 1988;62(10):2152–65.

5. Anderson E, Grant R, Lewis SC, Whittle IR. Randomized Phase III controlled trials of therapy in malignant glioma: where are we after 40 years? Br J Neurosurg. 2008;22(3):339–49.

6. Smith JS, Jenkins RB. Genetic alterations in adult diffuse glioma: occurrence, significance, and prognostic implications. Front Biosci. 2000;5:D213–D231.

7. Laws ER, Parney IF, Huang W, Anderson F, Morris AM, Asher A, et al. Survival following surgery and prognostic factors for recently diagnosed malignant glioma: data from the Glioma Outcomes Project. J Neurosurg. 2003;99(3):467–73.

8. Perrin RG, Bernstein M. Current treatment of malignant gliomas: an evidence-based review. Oncol Exch. 2004;3(3):28–32.

9. MacDonald SM, Ahmad S, Kachris S, Vogds BJ, DeRouen M, Gittleman AE, et al. Intensity modulated radiation therapy versus three-dimensional conformal radiation therapy for the treatment of high grade glioma: a dosimetric comparison. J Appl Clin Med Phys. 2007;8(2):47–60.

10. Stupp R, Mason WP, van den Bent MJ, Weller M, Fisher B, Taphoorn MJB, et al. Radiotherapy plus concomitant and adjuvant temozolomide for glioblastoma. N Engl J Med. 2005;352(10):987–96.

11. Thornton AF, Sandler HM, Ten Haken RK, McShan DL, Fraass BA, La Vigne ML, et al. The clinical utility of magnetic resonance imaging in 3-dimensional treatment planning of brain neoplasms. Int J Radiat Oncol Biol Phys. 1992;24(4):767–75.

12. Podgorsak EB. External photon beams: Physical aspects. In: Podgorsak EB, editor. Radiation oncology physics: A handbook for teachers and students. Vienna: International Atomic Energy Agency; 2005. p. 161–218.

13. Podgorsak EB. Treatment machines for external beam radiotherapy. In: Podgorsak EB, editor. Radiation oncology physics: A handbook for teachers and students. Vienna: International Atomic Energy Agency; 2005. p. 123–60.

14. Sheikh-Bagheri D, Rogers DWO. Monte Carlo calculation of nine megavoltage photon beam spectra using the BEAM code. Med Phys. 2002;29(3):391–402.

15. Khan FM. The physics of radiation therapy. 3rd ed. Philadelphia: Lippincott Williams & Wilkins; 2003.

16. Hubbell JH, Seltzer SM. Tables of X-ray mass attenuation coefficients and mass energy-absorption coefficients from 1 keV to 20 MeV for elements Z = 1 to 92 and 48 additional substances of dosimetric interest [Internet]; 1996 [cited 19 Jan 2013]. Available from: http://www.nist.gov/pml/data/xraycoef/.

17. Podgorsak EB. Basic radiation physics. In: Podgorsak EB, editor. Radiation oncology physics: A handbook for teachers and students. Vienna: International Atomic Energy Agency; 2005. p. 1–44.

18. Attix FH. Introduction to radiological physics and radiation dosimetry. New York: Wiley; 1986.

19. Report 85: Fundamental quantities and units for ionizing radiation. J ICRU. 2011;11(1):1–31.

20. Bloch F. Nuclear Induction. Phys Rev. 1946;70(7-8):460–74.

21. Bloch F, Hansen W, Packard M. Nuclear Induction. Phys Rev. 1946;69(3-4):127.

22. Hahn E. Spin Echoes. Phys Rev. 1950;80(4):580–94.

23. Hajnal JV, De Coene B, Lewis PD, Baudouin CJ, Cowan FM, Pennock JM, et al. High signal regions in normal white matter shown by heav-

ily T2-weighted CSF nulled IR sequences. J Comput Assist Tomogr. 1992;16(4):506–13.

24. Hajnal JV, Bryant DJ, Kasuboski L, Pattany PM, De Coene B, Lewis PD, et al. Use of fluid attenuated inversion recovery (FLAIR) pulse sequences in MRI of the brain. J Comput Assist Tomogr. 1992;16(6):841–4.

25. Stack JP, Antoun NM, Jenkins JP, Metcalfe R, Isherwood I. Gadolinium-DTPA as a contrast agent in magnetic resonance imaging of the brain. Neuroradiology. 1988;30(2):145–54.

26. Kelly PJ, Daumas-Duport C, Kispert DB, Kall Ba, Scheithauer BW, Illig JJ. Imaging-based stereotaxic serial biopsies in untreated intracranial glial neoplasms. J Neurosurg. 1987;66(6):865–74.

27. Gross MW, Weber WA, Feldmann HJ, Bartenstein P, Schwaiger M, Molls M. The value of F-18-fluorodeoxyglucose PET for the 3-D radiation treatment planning of malignant gliomas. Int J Radiat Oncol Biol Phys. 1998;41(5):989–95.

28. Podgorsak EB, Podgorsak MB. Special procedures and techniques in radiotherapy. In: Podgorsak EB, editor. Radiation oncology physics: A handbook for teachers and students. Vienna: International Atomic Energy Agency; 2005. p. 505–48.

29. Heiss WD, Wienhard K, Wagner R, Lanfermann H, Thiel A, Herholz K, et al. F-Dopa as an amino acid tracer to detect brain tumors. J Nucl Med. 1996;37(7):1180–2.

30. Stadlbauer A, Prante O, Nimsky C, Salomonowitz E, Buchfelder M, Kuwert T, et al. Metabolic imaging of cerebral gliomas: spatial correlation

of changes in O-(2-18F-fluoroethyl)-L-tyrosine PET and proton magnetic resonance spectroscopic imaging. J Nucl Med. 2008;49(5):721–9.

31. Miyagawa T, Oku T, Uehara H, Desai R, Beattie B, Tjuvajev J, et al. "Facilitated" amino acid transport is upregulated in brain tumors. J Cereb Blood Flow Metab. 1998;18(5):500–9.

32. Pirotte B, Goldman S, Massager N, David P, Wikler D, Vandesteene A, et al. Comparison of 18F-FDG and 11C-methionine for PET-guided stereotactic brain biopsy of gliomas. J Nucl Med. 2004;45(8):1293–8.

33. Weber DC, Zilli T, Buchegger F, Casanova N, Haller G, Rouzaud M, et al. [(18)F]Fluoroethyltyrosine- positron emission tomography-guided radiotherapy for high-grade glioma. Radiat Oncol. 2008;3(18):44.

34. Niyazi M, Geisler J, Siefert A, Schwarz SB, Ganswindt U, Garny S, et al. FET-PET for malignant glioma treatment planning. Radiother Oncol. 2011;99(1):44–8.

35. National Center for Biotechnology Information. PubChem Compound Database [Internet]; 2013 [cited 16 Oct 2013]. CID:56494. Available from: http://pubchem.ncbi.nlm.nih.gov/summary/summary.cgi?cid=56494.

36. Nanni C, Fanti S, Rubello D. 18F-DOPA PET and PET/CT. J Nucl Med. 2007;48(10):1577–9.

37. Garnett ES, Firnau G, Nahmias C. Dopamine visualized in the basal ganglia of living man. Nature. 1983;305(5930):137–8.

38. Becherer A, Karanikas G, Szabó M, Zettinig G, Asenbaum S, Marosi C, et al. Brain tumour imaging with PET: a comparison between [18F]fluorodopa

and [11C]methionine. Eur J Nucl Med Mol Imaging. 2003;30(11):1561–7.

39. Agid Y. Parkinson's disease: pathophysiology. Lancet. 1991;337(8753): 1321–4.

40. Chen W, Silverman DHS, Delaloye S, Czernin J, Kamdar N, Pope W, et al. 18F-FDOPA PET imaging of brain tumors: comparison study with 18F-FDG PET and evaluation of diagnostic accuracy. J Nucl Med. 2006;47(6):904–11.

41. Ledezma CJ, Chen W, Sai V, Freitas B, Cloughesy T, Czernin J, et al. 18F-FDOPA PET/MRI fusion in patients with primary/recurrent gliomas: initial experience. Eur J Radiol. 2009;71(2):242–8.

42. Alexander AL, Lee JE, Lazar M, Field AS. Diffusion tensor imaging of the brain. Neurotherapeutics. 2007;4(3):316–29.

43. Einstein A. [On the movement of small particles suspended in stationary liquids required by the molecular-kinetic theory of heat]. Ann Phys. 1905;322(8):549–60. German.

44. Stejskal EO, Tanner JE. Spin diffusion measurements: spin echoes in the presence of a time-dependent field gradient. J Chem Phys. 1965;42(1):288–92.

45. Basser PJ, Mattiello J, LeBihan D. MR diffusion tensor spectroscopy and imaging. Biophys J. 1994;66(1):259–67.

46. Basser PJ, Pierpaoli C. Microstructural and physiological features of tissues elucidated by quantitative-diffusion-tensor MRI. J Magn Reson B. 1996;111(3):209–19.

47. International Commission on Radiation Units and Measurements. Prescribing, recording and reporting photon beam therapy. Bethesda (MD): International Commission on Radiation Units and Measurements; 1993. Report No.: 50.

48. International Commission on Radiation Units and Measurements. Prescribing, recording and reporting photon beam therapy (supplement to ICRU report 50). Bethesda (MD): International Commission on Radiation Units and Measurements; 1999. Report No.: 62.

49. Shaffer R, Nichol AM, Vollans E, Fong M, Nakano S, Moiseenko V, et al. A comparison of volumetric modulated arc therapy and conventional intensity-modulated radiotherapy for frontal and temporal high-grade gliomas. Int J Radiat Oncol Biol Phys. 2010;76(4):1177–84.

50. Radiation Therapy Oncology Group. RTOG 0825: Phase III double-blind placebo-controlled trial of conventional concurrent chemoradiation and adjuvant temozolomide plus bevacizumab versus conventional concurrent chemoradiation and adjuvant temozolomide in patients with newly diagnosed glioblastoma [Internet]; 2011 [cited 11 Nov 2013]. Available from: http://www.rtog.org/ClinicalTrials/ProtocolTable/StudyDetails.aspx?action=openFile&FileID=4664.

51. Champ CE, Siglin J, Mishra MV, Shen X, Werner-Wasik M, Andrews DW, et al. Evaluating changes in radiation treatment volumes from postoperative to same-day planning MRI in High-grade gliomas. Radiat Oncol. 2012;7(1):220.

52. McDonald MW, Shu HKG, Curran WJ, Crocker IR. Pattern of failure after limited margin radiotherapy and temozolomide for glioblastoma. Int J Radiat Oncol Biol Phys. 2011;79(1):130–6.

53. Chang EL, Akyurek S, Avalos T, Rebueno N, Spicer C, Garcia J, et al. Evaluation of peritumoral edema in the delineation of radiotherapy clinical target volumes for glioblastoma. Int J Radiat Oncol Biol Phys. 2007;68(1):144–50.

54. Narayana A, Yamada J, Berry S, Shah P, Hunt M, Gutin PH, et al. Intensity-modulated radiotherapy in high-grade gliomas: clinical and dosimetric results. Int J Radiat Oncol Biol Phys. 2006;64(3):892–7.

55. Bortfeld T. Optimized planning using physical objectives and constraints. Semin Radiat Oncol. 1999;9(1):20–34.

56. Bortfeld TR, Kahler DL, Waldron TJ, Boyer AL. X-ray field compensation with multileaf collimators. Int J Radiat Oncol Biol Phys. 1994;28(3):723–30.

57. Mackie TR, Holmes T, Swerdloff S, Reckwerdt P, Deasy JO, Yang J, et al. Tomotherapy: a new concept for the delivery of dynamic conformal radiotherapy. Med Phys. 1993;20(6):1709–19.

58. Yu CX. Intensity-modulated arc therapy with dynamic multileaf collimation: an alternative to tomotherapy. Phys Med Biol. 1995;40(9):1435–49.

59. Yu CX, Li XA, Ma L, Chen D, Naqvi S, Shepard D, et al. Clinical implementation of intensity-modulated arc therapy. Int J Radiat Oncol Biol Phys. 2002;53(2):453–63.

60. Otto K. Volumetric modulated arc therapy: IMRT in a single gantry arc. Med Phys. 2008;35(1):310–7.

61. Bergman AM, Bush K, Milette MP, Popescu IA, Otto K, Duzenli C. Direct aperture optimization for IMRT using Monte Carlo generated beamlets. Med Phys. 2006;33(10):3666–79.

62. Chin E. A four dimensional volumetric modulated arc therapy planning system for stereotactic body radiation therapy in lung cancers. University of British Columbia; 2013.

63. Fowler JF. The linear-quadratic formula and progress in fractionated radiotherapy. Br J Radiol. 1989;62(740):679–94.

64. Qi XS, Schultz CJ, Li XA. An estimation of radiobiologic parameters from clinical outcomes for radiation treatment planning of brain tumor. Int J Radiat Oncol Biol Phys. 2006;64(5):1570–80.

65. Lea DE, Catcheside DG. The mechanism of the induction by radiation of chromosome aberrations in Tradescantia. J Genet. 1942;44(2-3):216–45.

66. Puck TT, Marcus PI. Action of x-rays on mammalian cells. J Exp Med. 1956;103(5):653–66.

67. Park C, Papiez L, Zhang S, Story M, Timmerman RD. Universal survival curve and single fraction equivalent dose: useful tools in understanding potency of ablative radiotherapy. Int J Radiat Oncol Biol Phys. 2008;70(3):847–52.

68. Brenner DJ, Hlatky LR, Hahnfeldt PJ, Huang Y, Sachs RK. The linear-quadratic model and most other common radiobiological models result

in similar predictions of time-dose relationships. Radiat Res. 1998; 150(1):83–91.

69. Brenner DJ. The linear-quadratic model is an appropriate methodology for determining isoeffective doses at large doses per fraction. Semin Radiat Oncol. 2008;18(4):234–9.

70. Burman C, Kutcher GJ, Emami B, Goitein M. Fitting of normal tissue tolerance data to an analytic function. Int J Radiat Oncol Biol Phys. 1991;21(1):123–35.

71. Moiseenko V, Deasy JO, Van Dyk J. Radiobiological modeling for treatment planning. In: Van Dyk J, editor. The modern technology of radiation oncology: A compendium for medical physicists and radiation oncologists. vol. 2. Madison (WI): Medical Physics Publishing; 2005. p. 185–220.

72. Niemierko A. Reporting and analyzing dose distributions: A concept of equivalent uniform dose. Med Phys. 1997;24(1):103–10.

73. Wu Q, Mohan R, Niemierko A, Schmidt-Ullrich R. Optimization of intensity-modulated radiotherapy plans based on the equivalent uniform dose. Int J Radiat Oncol Biol Phys. 2002;52(1):224–35.

74. Li XA, Alber M, Deasy JO, Jackson A, Ken Jee KW, Marks LB, et al. The use and QA of biologically related models for treatment planning: short report of the TG-166 of the therapy physics committee of the AAPM. Med Phys. 2012;39(3):1386–409.

75. Ling CC, Humm J, Larson S, Amols H, Fuks Z, Leibel S, et al. Towards multidimensional radiotherapy (MD-CRT): biological imaging and biological conformality. Int J Radiat Oncol Biol Phys. 2000;47(3):551–60.

76. Galvin JM, De Neve W. Intensity modulating and other radiation therapy devices for dose painting. J Clin Oncol. 2007;25(8):924–30.

77. Kim Y, Tomé Wa. Dose-painting IMRT optimization using biological parameters. Acta Oncol. 2010;49(8):1374–84.

78. Kracht LW, Miletic H, Busch S, Jacobs AH, Voges J, Hoevels M, et al. Delineation of brain tumor extent with [11C]L-methionine positron emission tomography: local comparison with stereotactic histopathology. Clin Cancer Res. 2004;10(21):7163–70.

79. Pafundi DH, Laack NN, Youland RS, Parney IF, Lowe VJ, Giannini C, et al. Biopsy validation of 18F-DOPA PET and biodistribution in gliomas for neurosurgical planning and radiotherapy target delineation: results of a prospective pilot study. Neuro Oncol. 2013;15(8):1058–67.

80. Archip N, Jolesz FA, Warfield SK. A validation framework for brain tumor segmentation. Acad Radiol. 2007;14(10):1242–51.

81. Deeley MA, Chen A, Datteri R, Noble JH, Cmelak AJ, Donnelly EF, et al. Comparison of manual and automatic segmentation methods for brain structures in the presence of space-occupying lesions: a multi-expert study. Phys Med Biol. 2011;56(14):4557–77.

82. Warfield SK, Zou KH, Wells WM. Simultaneous truth and performance level estimation (STAPLE): an algorithm for the validation of image segmentation. IEEE Trans Med Imaging. 2004;23(7):903–21.

83. Namavari M, Bishop A, Satyamurthy N, Bida G, Barrio JR. Regioselective radiofluorodestannylation with [18F]F2 and [18F]CH3COOF: a

high yield synthesis of 6-[18F]Fluoro-L-dopa. Int J Rad Appl Instrum A. 1992;43(8):989–96.

84. McGurk RJ, Bowsher J, Lee Ja, Das SK. Combining multiple FDG-PET radiotherapy target segmentation methods to reduce the effect of variable performance of individual segmentation methods. Med Phys. 2013;40(4):042501.

85. Jaccard P. [Comparative study of the distribution of flora in a portion of the Alps and the Jura]. Bull Soc Vaud Sci Nat. 1901;37(142):547–79. French.

86. Jaccard P. The distribution of the flora in the alpine zone. New Phytol. 1912;11(2):37–50.

87. Lee SW, Fraass Ba, Marsh LH, Herbort K, Gebarski SS, Martel MK, et al. Patterns of failure following high-dose 3-D conformal radiotherapy for high-grade astrocytomas: a quantitative dosimetric study. Int J Radiat Oncol Biol Phys. 1999;43(1):79–88.

88. Cattaneo GM, Reni M, Rizzo G, Castellone P, Ceresoli GL, Cozzarini C, et al. Target delineation in post-operative radiotherapy of brain gliomas: interobserver variability and impact of image registration of MR(pre-operative) images on treatment planning CT scans. Radiother Oncol. 2005;75(2):217–23.

89. Jena R, Price SJ, Baker C, Jefferies SJ, Pickard JD, Gillard JH, et al. Diffusion tensor imaging: possible implications for radiotherapy treatment planning of patients with high-grade glioma. Clin Oncol (R Coll Radiol). 2005;17(8):581–90.

90. Bondiau PY, Konukoglu E, Clatz O, Delingette H, Frenay M, Paquis P. Biocomputing: numerical simulation of glioblastoma growth and comparison with conventional irradiation margins. Phys Med. 2011;27(2):103–8.

91. Chen W. Clinical applications of PET in brain tumors. J Nucl Med. 2007;48(9):1468–81.

92. Lee IH, Piert M, Gomez-Hassan D, Junck L, Rogers L, Hayman J, et al. Association of 11C-methionine PET uptake with site of failure after concurrent temozolomide and radiation for primary glioblastoma multiforme. Int J Radiat Oncol Biol Phys. 2009;73(2):479–85.

93. Weber DC, Casanova N, Zilli T, Buchegger F, Rouzaud M, Nouet P, et al. Recurrence pattern after [(18)F]fluoroethyltyrosine-positron emission tomography-guided radiotherapy for high-grade glioma: a prospective study. Radiother Oncol. 2009;93(3):586–92.

94. Fueger BJ, Czernin J, Cloughesy T, Silverman DH, Geist CL, Walter Ma, et al. Correlation of 6-18F-fluoro-L-dopa PET uptake with proliferation and tumor grade in newly diagnosed and recurrent gliomas. J Nucl Med. 2010;51(10):1532–8.

95. Piroth MD, Pinkawa M, Holy R, Klotz J, Schaar S, Stoffels G, et al. Integrated boost IMRT with FET-PET-adapted local dose escalation in glioblastomas. Results of a prospective phase II study. Strahlenther Onkol. 2012;188(4):334–9.

96. Rickhey M, Morávek Z, Eilles C, Koelbl O, Bogner L. 18F-FET-PET-based dose painting by numbers with protons. Strahlenther Onkol. 2010;186(6):320–6.

97. Walter F, Cloughesy T, Walter Ma, Lai A, Nghiemphu P, Wagle N, et al. Impact of 3,4-dihydroxy-6-18F-fluoro-L-phenylalanine PET/CT on managing patients with brain tumors: the referring physician's perspective. J Nucl Med. 2012;53(3):393–8.

98. Painter KJ, Hillen T. Mathematical modelling of glioma growth: the use of Diffusion Tensor Imaging (DTI) data to predict the anisotropic pathways of cancer invasion. J Theor Biol. 2013;323:25–39.

99. Giese A, Kluwe L, Laube B, Meissner H, Berens ME, Westphal M. Migration of human glioma cells on myelin. Neurosurgery. 1996;38(4):755–64.

100. Clatz O, Sermesant M, Bondiau PY, Delingette H, Warfield SK, Malandain G, et al. Realistic simulation of the 3-D growth of brain tumors in MR images coupling diffusion with biomechanical deformation. IEEE Trans Med Imaging. 2005;24(10):1334–46.

101. Bondiau PY, Clatz O, Sermesant M, Marcy PY, Delingette H, Frenay M, et al. Biocomputing: numerical simulation of glioblastoma growth using diffusion tensor imaging. Phys Med Biol. 2008;53(4):879–93.

102. Konukoglu E, Clatz O, Bondiau PY, Delingette H, Ayache N. Extrapolating glioma invasion margin in brain magnetic resonance images: suggesting new irradiation margins. Med Image Anal. 2010;14(2):111–25.

103. Jbabdi S, Mandonnet E, Duffau H, Capelle L, Swanson KR, Pélégrini-Issac M, et al. Simulation of anisotropic growth of low-grade gliomas using diffusion tensor imaging. Magn Reson Med. 2005;54(3):616–24.

104. Kallenberg K, Goldmann T, Menke J, Strik H, Bock HC, Stockhammer F, et al. Glioma infiltration of the corpus callosum: early signs detected by DTI. J Neurooncol. 2013;112(2):217–22.

105. Deng Z, Yan Y, Zhong D, Yang G, Tang W, Lü F, et al. Quantitative analysis of glioma cell invasion by diffusion tensor imaging. J Clin Neurosci. 2010;17(12):1530–6.

106. Beppu T, Inoue T, Shibata Y, Yamada N, Kurose A, Ogasawara K, et al. Fractional anisotropy value by diffusion tensor magnetic resonance imaging as a predictor of cell density and proliferation activity of glioblastomas. Surg Neurol. 2005;63(1):56–61.

107. Kinoshita M, Hashimoto N, Goto T, Kagawa N, Kishima H, Izumoto S, et al. Fractional anisotropy and tumor cell density of the tumor core show positive correlation in diffusion tensor magnetic resonance imaging of malignant brain tumors. Neuroimage. 2008;43(1):29–35.

108. Stadlbauer A, Ganslandt O, Buslei R, Hammen T, Gruber S, Moser E, et al. Gliomas: histopathologic evaluation of changes in directionality and magnitude of water diffusion at diffusion-tensor MR imaging. Radiology. 2006;240(3):803–10.

109. Lee EJ, Lee SK, Agid R, Bae JM, Keller A, Terbrugge K. Preoperative grading of presumptive low-grade astrocytomas on MR imaging: diagnostic value of minimum apparent diffusion coefficient. AJNR Am J Neuroradiol. 2008;29(10):1872–7.

110. Aubert-Broche B, Grova C, Jannin P, Buvat I, Benali H, Gibaud B. Detection of inter-hemispheric asymmetries of brain perfusion in SPECT. Phys Med Biol. 2003;48(11):1505–17.

111. Jenkinson M, Beckmann CF, Behrens TEJ, Woolrich MW, Smith SM. FSL. Neuroimage. 2012;62(2):782–90.

112. Woolrich MW, Jbabdi S, Patenaude B, Chappell M, Makni S, Behrens T, et al. Bayesian analysis of neuroimaging data in FSL. Neuroimage. 2009;45(1 Suppl):S173–S186.

113. Smith SM, Jenkinson M, Woolrich MW, Beckmann CF, Behrens TEJ, Johansen-Berg H, et al. Advances in functional and structural MR image analysis and implementation as FSL. Neuroimage. 2004;23 Suppl 1:S208–S219.

114. Smith SM. Fast robust automated brain extraction. Hum Brain Mapp. 2002;17(3):143–55.

115. Behrens TEJ, Woolrich MW, Jenkinson M, Johansen-Berg H, Nunes RG, Clare S, et al. Characterization and propagation of uncertainty in diffusion-weighted MR imaging. Magn Reson Med. 2003;50(5):1077–88.

116. Behrens TEJ, Johansen-Berg H, Woolrich MW, Smith SM, Wheeler-Kingshott CAM, Boulby PA, et al. Non-invasive mapping of connections between human thalamus and cortex using diffusion imaging. Nat Neurosci. 2003;6(7):750–7.

117. Behrens TEJ, Berg HJ, Jbabdi S, Rushworth MFS, Woolrich MW. Probabilistic diffusion tractography with multiple fibre orientations: What can we gain? Neuroimage. 2007;34(1):144–55.

118. Johansen-Berg H, Behrens TEJ, Robson MD, Drobnjak I, Rushworth MFS, Brady JM, et al. Changes in connectivity profiles define functionally distinct regions in human medial frontal cortex. Proc Natl Acad Sci U S A. 2004;101(36):13335–40.

119. Jbabdi S, Sotiropoulos SN, Savio AM, Graña M, Behrens TEJ. Model-based analysis of multishell diffusion MR data for tractography: how to get over fitting problems. Magn Reson Med. 2012;68(6):1846–55.

120. Jenkinson M, Smith S. A global optimisation method for robust affine registration of brain images. Med Image Anal. 2001;5(2):143–56.

121. Jenkinson M, Bannister P, Brady M, Smith S. Improved optimization for the robust and accurate linear registration and motion correction of brain images. Neuroimage. 2002;17(2):825–41.

122. Grabner G, Janke AL, Budge MM, Smith D, Pruessner J, Collins DL. Symmetric atlasing and model based segmentation: an application to the hippocampus in older adults. Med Image Comput Comput Assist Interv. 2006;9(Pt 2):58–66.

123. Andersson JLR, Jenkinson M, Smith S. Non-linear registration aka spatial normalisation. Oxford (UK): Oxford Centre for Functional MRI of the Brain; 2007. Report No.: TR07JA2.

124. Andersson JLR, Jenkinson M, Smith S. Non-linear optimisation. Oxford (UK): Oxford Centre for Functional MRI of the Brain; 2007. Report No.: TR07JA1.

125. Rueckert D, Sonoda LI, Hayes C, Hill DL, Leach MO, Hawkes DJ. Non-rigid registration using free-form deformations: application to breast MR images. IEEE Trans Med Imaging. 1999;18(8):712–21.

126. Oxford Centre for Functional MRI of the Brain. FMRIB58_FA [Internet]; 2012 [cited 22 Nov 2013]. Available from: http://fsl.fmrib.ox.ac.uk/fsl/fslwiki/FMRIB58_FA.

127. Stadlbauer A, Hammen T, Buchfelder M, Bachmair J, Dörfler A, Nimsky C, et al. Differences in metabolism of fiber tract alterations in gliomas: a combined fiber density mapping and magnetic resonance spectroscopic imaging study. Neurosurgery. 2012;71(2):454–63.

128. Rose S, Fay M, Thomas P, Bourgeat P, Dowson N, Salvado O, et al. Correlation of MRI-derived apparent diffusion coefficients in newly diagnosed gliomas with [18F]-fluoro-L-dopa PET: what are we really measuring with minimum ADC? AJNR Am J Neuroradiol. 2013;34(4):758–64.

129. Stadlbauer A, Buchfelder M, Salomonowitz E, Ganslandt O. Fiber density mapping of gliomas: histopathologic evaluation of a diffusion-tensor imaging data processing method. Radiology. 2010;257(3):846–53.

130. Chan MF, Schupak K, Burman C, Chui CS, Ling CC. Comparison of intensity-modulated radiotherapy with three-dimensional conformal radiation therapy planning for glioblastoma multiforme. Med Dosim. 2003;28(4):261–5.

131. Hermanto U, Frija EK, Lii MJ, Chang EL, Mahajan A, Woo SY. Intensity-modulated radiotherapy (IMRT) and conventional three-dimensional conformal radiotherapy for high-grade gliomas: does IMRT increase the in-

tegral dose to normal brain? Int J Radiat Oncol Biol Phys. 2007;67(4): 1135–44.

132. Thilmann C, Zabel A, Grosser KH, Hoess A, Wannenmacher M, Debus J. Intensity-modulated radiotherapy with an integrated boost to the macroscopic tumor volume in the treatment of high-grade gliomas. Int J Cancer. 2001;96(6):341–9.

133. Floyd NS, Woo SY, Teh BS, Prado C, Mai WY, Trask T, et al. Hypofractionated intensity-modulated radiotherapy for primary glioblastoma multiforme. Int J Radiat Oncol Biol Phys. 2004;58(3):721–6.

134. Sultanem K, Patrocinio H, Lambert C, Corns R, Leblanc R, Parker W, et al. The use of hypofractionated intensity-modulated irradiation in the treatment of glioblastoma multiforme: preliminary results of a prospective trial. Int J Radiat Oncol Biol Phys. 2004;58(1):247–52.

135. Iuchi T, Hatano K, Narita Y, Kodama T, Yamaki T, Osato K. Hypofractionated high-dose irradiation for the treatment of malignant astrocytomas using simultaneous integrated boost technique by IMRT. Int J Radiat Oncol Biol Phys. 2006;64(5):1317–24.

136. Panet-Raymond V, Souhami L, Roberge D, Kavan P, Shakibnia L, Muanza T, et al. Accelerated hypofractionated intensity-modulated radiotherapy with concurrent and adjuvant temozolomide for patients with glioblastoma multiforme: a safety and efficacy analysis. Int J Radiat Oncol Biol Phys. 2009;73(2):473–8.

137. Nakamatsu K, Suzuki M, Nishimura Y, Kanamori S, Koike R, Shibata T, et al. Treatment outcomes and dose-volume histogram analysis of simul-

taneous integrated boost method for malignant gliomas using intensity-modulated radiotherapy. Int J Clin Oncol. 2008;13(1):48–53.

138. Miwa K, Matsuo M, Shinoda J, Oka N, Kato T, Okumura A, et al. Simultaneous integrated boost technique by helical tomotherapy for the treatment of glioblastoma multiforme with 11C-methionine PET: report of three cases. J Neurooncol. 2008;87(3):333–9.

139. Chan JL, Lee SW, Fraass BA, Normolle DP, Greenberg HS, Junck LR, et al. Survival and failure patterns of high-grade gliomas after three-dimensional conformal radiotherapy. J Clin Oncol. 2002;20(6):1635–42.

140. Petrecca K, Guiot MC, Panet-Raymond V, Souhami L. Failure pattern following complete resection plus radiotherapy and temozolomide is at the resection margin in patients with glioblastoma. J Neurooncol. 2013;111(1):19–23.

141. Kosztyla R, Chan EK, Hsu F, Wilson D, Ma R, Cheung A, et al. High-grade glioma radiation therapy target volumes and patterns of failure obtained from magnetic resonance imaging and (18)F-FDOPA positron emission tomography delineations from multiple observers. Int J Radiat Oncol Biol Phys. 2013;87(5):1100–6.

142. Oppitz U, Maessen D, Zunterer H, Richter S, Flentje M. 3D-recurrence-patterns of glioblastomas after CT-planned postoperative irradiation. Radiother Oncol. 1999;53(1):53–7.

143. Tsien C, Moughan J, Michalski JM, Gilbert MR, Purdy J, Simpson J, et al. Phase I three-dimensional conformal radiation dose escalation study in

newly diagnosed glioblastoma: Radiation Therapy Oncology Group Trial 98-03. Int J Radiat Oncol Biol Phys. 2009;73(3):699–708.

144. Stewart RD, Li XA. BGRT: Biologically guided radiation therapy—The future is fast approaching! Med Phys. 2007;34(10):3739–51.

145. Walter F, la Fougère C, Belka C, Niyazi M. Technical Issues of [(18)F]FET-PET Imaging for Radiation Therapy Planning in Malignant Glioma Patients - A Review. Front Oncol. 2012;2:130.

146. Bentzen S. Theragnostic imaging for radiation oncology: dose-painting by numbers. Lancet Oncol. 2005;6(2):112–7.

147. Bentzen S, Gregoire V. Molecular imaging-based dose painting: a novel paradigm for radiation therapy prescription. Semin Radiat Oncol. 2011;21(2):101–10.

148. Thorwarth D, Eschmann SM, Paulsen F, Alber M. Hypoxia dose painting by numbers: a planning study. Int J Radiat Oncol Biol Phys. 2007;68(1):291–300.

149. Niyazi M, Bartenstein P, Belka C, Ganswindt U. Choline PET based dose-painting in prostate cancer–modelling of dose effects. Radiat Oncol. 2010;5:23.

150. Würschmidt F, Petersen C, Wahl A, Dahle J, Kretschmer M. [18F] fluoroethylcholine-PET/CT imaging for radiation treatment planning of recurrent and primary prostate cancer with dose escalation to PET/CT-positive lymph nodes. Radiat Oncol. 2011;6:44.

151. Chang JH, Lim Joon D, Lee ST, Gong SJ, Anderson NJ, Scott AM, et al. Intensity modulated radiation therapy dose painting for localized prostate

cancer using ^{11}C-choline positron emission tomography scans. Int J Radiat Oncol Biol Phys. 2012;83(5):e691–e696.

152. Meijer G, Steenhuijsen J, Bal M, De Jaeger K, Schuring D, Theuws J. Dose painting by contours versus dose painting by numbers for stage II/III lung cancer: practical implications of using a broad or sharp brush. Radiother Oncol. 2011;100(3):396–401.

153. Piroth MD, Pinkawa M, Holy R, Stoffels G, Demirel C, Attieh C, et al. Integrated-boost IMRT or 3-D-CRT using FET-PET based auto-contoured target volume delineation for glioblastoma multiforme–a dosimetric comparison. Radiat Oncol. 2009;4:57.

154. Ken S, Vieillevigne L, Franceries X, Simon L, Supper C, Lotterie JA, et al. Integration method of 3D MR spectroscopy into treatment planning system for glioblastoma IMRT dose painting with integrated simultaneous boost. Radiat Oncol. 2013;8:1.

155. Duprez F, De Neve W, De Gersem W, Coghe M, Madani I. Adaptive dose painting by numbers for head-and-neck cancer. Int J Radiat Oncol Biol Phys. 2011;80(4):1045–55.

156. Madani I, Duprez F, Boterberg T, Van de Wiele C, Bonte K, Deron P, et al. Maximum tolerated dose in a phase I trial on adaptive dose painting by numbers for head and neck cancer. Radiother Oncol. 2011;101(3):351–5.

157. Rickhey M, Koelbl O, Eilles C, Bogner L. A biologically adapted dose-escalation approach, demonstrated for 18F-FET-PET in brain tumors. Strahlenther Onkol. 2008;184(10):536–42.

158. Jones B, Sanghera P. Estimation of radiobiologic parameters and equivalent radiation dose of cytotoxic chemotherapy in malignant glioma. Int J Radiat Oncol Biol Phys. 2007;68(2):441–8.

159. Mayo C, Yorke E, Merchant TE. Radiation associated brainstem injury. Int J Radiat Oncol Biol Phys. 2010;76(3 Suppl):S36–S41.

160. Mayo C, Martel MK, Marks LB, Flickinger J, Nam J, Kirkpatrick J. Radiation dose-volume effects of optic nerves and chiasm. Int J Radiat Oncol Biol Phys. 2010;76(3 Suppl):S28–S35.

161. Lawrence YR, Li XA, el Naqa I, Hahn CA, Marks LB, Merchant TE, et al. Radiation dose-volume effects in the brain. Int J Radiat Oncol Biol Phys. 2010;76(3 Suppl):S20–S27.

162. Wigg D. Applied radiobiology and bioeffect planning. Madison (WI): Medical Physics Publishing; 2001.

163. Panet-Raymond V, Ansbacher W, Zavgorodni S, Bendorffe B, Nichol A, Truong PT, et al. Coplanar versus noncoplanar intensity-modulated radiation therapy (IMRT) and volumetric-modulated arc therapy (VMAT) treatment planning for fronto-temporal high-grade glioma. J Appl Clin Med Phys. 2012;13(4):3826.

164. Pauleit D, Floeth F, Hamacher K, Riemenschneider MJ, Reifenberger G, Müller HW, et al. O-(2-[18F]fluoroethyl)-L-tyrosine PET combined with MRI improves the diagnostic assessment of cerebral gliomas. Brain. 2005;128(Pt 3):678–87.

165. Rachinger W, Goetz C, Pöpperl G, Gildehaus FJ, Kreth FW, Holtmannspötter M, et al. Positron emission tomography with O-(2-[18F]fluoroethyl)-l-

tyrosine versus magnetic resonance imaging in the diagnosis of recurrent gliomas. Neurosurgery. 2005;57(3):505–11.

166. Pöpperl G, Götz C, Rachinger W, Gildehaus FJ, Tonn JC, Tatsch K. Value of O-(2-[18F]fluoroethyl)- L-tyrosine PET for the diagnosis of recurrent glioma. Eur J Nucl Med Mol Imaging. 2004;31(11):1464–70.

167. Thorwarth D, Soukup M, Alber M. Dose painting with IMPT, helical tomotherapy and IMXT: a dosimetric comparison. Radiother Oncol. 2008;86(1):30–4.

168. Houweling AC, Wolf AL, Vogel WV, Hamming-Vrieze O, van Vliet-Vroegindeweij C, van de Kamer JB, et al. FDG-PET and diffusion-weighted MRI in head-and-neck cancer patients: Implications for dose painting. Radiother Oncol. 2013;106(2):250–4.

169. Sanai N, Berger MS. Glioma extent of resection and its impact on patient outcome. Neurosurgery. 2008;62(4):753–64.

170. Karunanithi S, Sharma P, Kumar A, Khangembam BC, Bandopadhyaya GP, Kumar R, et al. Comparative diagnostic accuracy of contrast-enhanced MRI and (18)F-FDOPA PET-CT in recurrent glioma. Eur Radiol. 2013;23(9):2628–35.

171. Karunanithi S, Sharma P, Kumar A, Gupta DK, Khangembam BC, Ballal S, et al. Can (18)F-FDOPA PET/CT predict survival in patients with suspected recurrent glioma? A prospective study. Eur J Radiol. 2014;83(1):219–25.

172. Harris RJ, Cloughesy TF, Pope WB, Nghiemphu PL, Lai A, Zaw T, et al. 18F-FDOPA and 18F-FLT positron emission tomography parametric response

maps predict response in recurrent malignant gliomas treated with bevacizumab. Neuro Oncol. 2012;14(8):1079–89.

173. Coenen VA, Krings T, Mayfrank L, Polin RS, Reinges MH, Thron A, et al. Three-dimensional visualization of the pyramidal tract in a neuronavigation system during brain tumor surgery: first experiences and technical note. Neurosurgery. 2001;49(1):86–92.

174. Abdullah KG, Lubelski D, Nucifora PGP, Brem S. Use of diffusion tensor imaging in glioma resection. Neurosurg Focus. 2013;34(4):E1.

175. Wu JS, Zhou LF, Tang WJ, Mao Y, Hu J, Song YY, et al. Clinical evaluation and follow-up outcome of diffusion tensor imaging-based functional neuronavigation: a prospective, controlled study in patients with gliomas involving pyramidal tracts. Neurosurgery. 2007;61(5):935–48; discussion 948–9.

176. Trepanier PY, Fortin I, Lambert C, Lacroix F. A Monte Carlo based formalism to identify potential locations at high risk of tumor recurrence with a numerical model for glioblastoma multiforme. Med Phys. 2012;39(11):6682–91.

177. Gooya A, Pohl KM, Bilello M, Cirillo L, Biros G, Melhem ER, et al. GLISTR: glioma image segmentation and registration. IEEE Trans Med Imaging. 2012;31(10):1941–54.

178. Zeng QS, Li CF, Liu H, Zhen JH, Feng DC. Distinction between recurrent glioma and radiation injury using magnetic resonance spectroscopy in combination with diffusion-weighted imaging. Int J Radiat Oncol Biol Phys. 2007;68(1):151–8.

179. Wang S, Kim S, Chawla S, Wolf RL, Zhang WG, O'Rourke DM, et al. Differentiation between glioblastomas and solitary brain metastases using diffusion tensor imaging. Neuroimage. 2009;44(3):653–60.

180. Xu JL, Li YL, Lian JM, Dou SW, Yan FS, Wu H, et al. Distinction between postoperative recurrent glioma and radiation injury using MR diffusion tensor imaging. Neuroradiology. 2010;52(12):1193–9.

181. Giussani C, Poliakov A, Ferri RT, Plawner LL, Browd SR, Shaw DWW, et al. DTI fiber tracking to differentiate demyelinating diseases from diffuse brain stem glioma. Neuroimage. 2010;52(1):217–23.

182. Byrnes TJD, Barrick TR, Bell BA, Clark CA. Diffusion tensor imaging discriminates between glioblastoma and cerebral metastases in vivo. NMR Biomed. 2011;24(1):54–60.

183. Wang S, Kim S, Chawla S, Wolf RL, Knipp DE, Vossough A, et al. Differentiation between glioblastomas, solitary brain metastases, and primary cerebral lymphomas using diffusion tensor and dynamic susceptibility contrast-enhanced MR imaging. AJNR Am J Neuroradiol. 2011;32(3):507–14.

184. Hua C, Merchant TE, Gajjar A, Broniscer A, Zhang Y, Li Y, et al. Brain tumor therapy-induced changes in normal-appearing brainstem measured with longitudinal diffusion tensor imaging. Int J Radiat Oncol Biol Phys. 2012;82(5):2047–54.

185. Chen F, Zhang X, Li M, Wang R, Wang HT, Zhu F, et al. Axial diffusivity and tensor shape as early markers to assess cerebral white matter damage

caused by brain tumors using quantitative diffusion tensor tractography. CNS Neurosci Ther. 2012;18(8):667–73.

186. Provenzale JM, McGraw P, Mhatre P, Guo AC, Delong D. Peritumoral brain regions in gliomas and meningiomas: investigation with isotropic diffusion-weighted MR imaging and diffusion-tensor MR imaging. Radiology. 2004;232(2):451–60.

187. Toh CH, Castillo M, Wong AMC, Wei KC, Wong HF, Ng SH, et al. Primary cerebral lymphoma and glioblastoma multiforme: differences in diffusion characteristics evaluated with diffusion tensor imaging. AJNR Am J Neuroradiol. 2008;29(3):471–5.

188. Kim MJ, Kim HS, Kim JH, Cho KG, Kim SY. Diagnostic accuracy and interobserver variability of pulsed arterial spin labeling for glioma grading. Acta Radiol. 2008;49(4):450–7.

189. Cao Y, Tsien CI, Nagesh V, Junck L, Ten Haken R, Ross BD, et al. Survival prediction in high-grade gliomas by MRI perfusion before and during early stage of RT [corrected]. Int J Radiat Oncol Biol Phys. 2006;64(3):876–85.

190. Bisdas S, Naegele T, Ritz R, Dimostheni A, Pfannenberg C, Reimold M, et al. Distinguishing recurrent high-grade gliomas from radiation injury: a pilot study using dynamic contrast-enhanced MR imaging. Acad Radiol. 2011;18(5):575–83.

191. Dujardin MI, Sourbron SP, Chaskis C, Verellen D, Stadnik T, de Mey J, et al. Quantification of cerebral tumour blood flow and permeability with T1-weighted dynamic contrast enhanced MRI: a feasibility study. J Neuroradiol. 2012;39(4):227–35.

192. Laprie A, Catalaa I, Cassol E, McKnight TR, Berchery D, Marre D, et al. Proton magnetic resonance spectroscopic imaging in newly diagnosed glioblastoma: predictive value for the site of postradiotherapy relapse in a prospective longitudinal study. Int J Radiat Oncol Biol Phys. 2008;70(3):773–81.

193. Pirzkall A, Li X, Oh J, Chang S, Berger MS, Larson Da, et al. 3D MRSI for resected high-grade gliomas before RT: tumor extent according to metabolic activity in relation to MRI. Int J Radiat Oncol Biol Phys. 2004;59(1):126–37.

194. Karunanithi S, Bandopadhyaya GP, Sharma P, Kumar A, Singla S, Malhotra A, et al. Prospective comparison of 99mTc-GH SPECT/CT and 18F-FDOPA PET/CT for detection of recurrent glioma: A pilot study. Clin Nucl Med. 2014;39(2):e121–e128.

195. Nielles-Vallespin S, Weber MA, Bock M, Bongers A, Speier P, Combs SE, et al. 3D radial projection technique with ultrashort echo times for sodium MRI: clinical applications in human brain and skeletal muscle. Magn Reson Med. 2007;57(1):74–81.

196. Weber MA, Henze M, Tüttenberg J, Stieltjes B, Meissner M, Zimmer F, et al. Biopsy targeting gliomas: do functional imaging techniques identify similar target areas? Invest Radiol. 2010;45(12):755–68.

197. Tanderup K, Olsen DR, Grau C. Dose painting: art or science? Radiother Oncol. 2006;79(3):245–8.

198. Daisne JF, Sibomana M, Bol A, Doumont T, Lonneux M, Grégoire V. Tridimensional automatic segmentation of PET volumes based on measured

source-to-background ratios: influence of reconstruction algorithms. Radiother Oncol. 2003;69(3):247–50.